



Universidad de Concepción
Dirección de Postgrado
Facultad de Ciencias Químicas
Departamento Ciencias de la Tierra

**Estructura friccional de la mega-falla inversa del margen de
subducción Chileno**

(Frictional structure of the Chilean megathrust)

Tesis para optar al grado de Doctor en Ciencias Geológicas

Diego Alexis Molina Ormazabal
Concepción, Chile
2022

Profesor Guía : Andrés Tassara Oddo
Depto Ciencias de la Tierra, Facultad de Ciencias Químicas
Universidad de Concepción

Agradecimientos

Esta tesis de cierta forma plasma un sin número de experiencias tanto académicas como personales que me han hecho crecer y desarrollarme como una persona más íntegra. Aquí están reflejados 5 años de vivencias, altos, bajos pero por sobre todo esfuerzo y perseverancia. Por lo mismo, el primer agradecimiento va a mi mismo, por haber tomado este desafío y seguir adelante pese a todas las dificultades que se dieron en el camino.

El rodearse de un ambiente amoroso, acogedor y contenedor es uno de los factores que permitieron el culminar este manuscrito, muchas veces proporcionando inspiración, motivación y amor. Mi familia, mi mamá Rosa, José, mis hermanos, mis abuelos que ya no están, mi padre, abuela Carmen y muchos otros de mi núcleo familiar cercano, a ellos, infinitas gracias. Quizás no lo saben, pero valoro enormemente su apoyo y contención. Con ustedes comparto este sentimiento de felicidad y éxito. Gracias, sobre todo por entender muchas veces mi distanciamiento para terminar este proceso. Los amo.

Quiero expresar también mi reconocimiento a Klaus Bataille. Fue él quien me insertó primeramente en el mundo de los terremotos y el hacer ciencia. Pero además brindándome el espacio idóneo para poder terminar este proceso. Además de convertirse en un colega y amigo. Por supuesto que también resalto, valoro y agradezco el enorme e incondicional apoyo otorgado por mi profesor guía y amigo, Andrés Tassara, a quien admiro tanto por su riqueza académica como personal. Andrés sin duda es pilar fundamental del éxito de esta tesis pero además de permitirme desarrollarme como científico y ser una persona más íntegra. No puedo dejar de lado a Jean-Paul Ampuero, quien tuvo la disposición de recibirme en Francia en el marco de este doctorado. Pablo Ampuero me recibió y además abrió las puertas de su familia, dando contención y compañía tan necesarias en época de pandemia y aislamiento. Me hizo mirar la dinámica de terremotos desde una perspectiva más física, además de tener la paciencia y motivación para apoyarme en mi investigación, a pesar de no tener obligación. Así mismo agradezco al Dr. Rodrigo Abarca y Dr. Andrea Madella por recibirme y pacientemente enseñarme nuevas metodologías asociadas al estudio de los grandes terremotos y brindarme su conocimiento en el desarrollo de este manuscrito.

Agradezco a todas mis amistades que muchas veces sin saberlo, me estaban empujando a seguir a través de la motivación, compañía y amor. Entre ellos María Esperanza y Joaquín Cortés, quienes a pesar de ser funcionarios del departamento de Ciencias de la Tierra, tuvieron la gentileza de considerarme como amigo. También agradezco a Valeria, Paula, Luchin, Belén, Emilio, Hector, Estela, entre cuantos otros, por estar ahí siempre que necesité.

Quiero extender mis agradecimiento a las múltiples fuentes de financiamiento que se requirió durante mi pasantía, congresos y finalización de este doctorado. Entre ellos el proyecto Núcleo Milenio Cyclo, dirigido por Daniel Melnick a quien también doy gracias por su apoyo en el desarrollo de mi investigación y las ocasiones de discusión científica. Finalmente a la Universidad de Concepción y a becas ANID.

Diego Molina

1 de abril de 2020.

Resumen

Las zonas de subducción tipo chilena se dan en márgenes convergentes entre una placa oceánica y continental. El contacto entre placas da lugar a la mega-falla inversa o *megathrust* en inglés. Aquí es donde se localiza la zona sismogénica y donde los terremotos más destructivos ocurren. Estos son repentinas dislocaciones que ocurren una vez la resistencia de la falla se ve superada debido a los esfuerzos tectónicos generados por la colisión entre la placa superior e inferior. Se ha reportado que los terremotos responden a periodos de carga y descarga de esfuerzos elásticos, proceso conocido como el ciclo sísmico, que finalmente culmina con el deslizamiento relativo entre ambas placas. El deslizamiento máximo tiende a desarrollarse en zonas de alta fricción conocidas como asperezas sísmicas, mientras que regiones con menor deslizamiento (baja fricción), muchas veces inhibiendo la propagación de terremotos, corresponden a barreras sísmicas. Esto se debe a que las zonas de alta fricción permanecen acopladas durante el proceso de carga (intersísmico), generando déficit de deslizamiento que debe ser eventualmente liberado. Generalmente las barreras se asocian a un bajo acoplamiento intersísmico. Esta distribución heterogénea de propiedades friccionales puede ser definida como la estructura friccional del megathrust.

Gracias a observaciones geológicas e instrumentales se ha podido inferir que segmentos de distinta extensión parecieran ser caracterizados por ciclos sísmicos de distinta duración, dando lugar a la segmentación sísmica. La segmentación de terremotos a lo largo de zonas de subducción es importante ya que da ideas de la máxima extensión de un terremoto, lo cual impacta directamente el riesgo sísmico. Es probable que la presencia de distintos segmentos sismogénicos respondan a una heterogénea estructura friccional del megathrust. No obstante, los mecanismos controlando tal estructura y por lo tanto la segmentación sismogénica y su persistencia, aún no son totalmente comprendidos. Algunas pistas acerca de los factores modulando la estructura friccional viene de la correlación espacial entre estructuras geológicas de la placa oceánica-continental (estructura geológica del ante arco) y la extensión de terremotos.

Esta tesis propone como hipótesis que la estructura geológica del ante-arco controla la estructura friccional del megathrust. Para validar esta hipótesis, se propone

utilizar el margen chileno dado su amplio registro sísmico y la variedad de ambientes geológicos, convirtiendo a la zona de subducción chilena como un verdadero laboratorio natural.

Mediante el empleo de Análisis por Componentes Principales, se logra estimar la correlación espacial entre distintos campos geofísicos y geológicos utilizados para iluminar la estructura friccional. A partir de esto se muestra que el primer componente de los campos muestra una clara relación con la distribución de sismicidad, sugiriendo que el primer componente representa el primer orden de la estructura friccional del margen Chileno. Esto es utilizado para construir el primer modelo formal de segmentación para Chile, el cual puede ser aplicado para la mejor evaluación de riesgo sísmico en el país y/o en otra zona de subducción. Por otro lado, los resultados indican que la zona norte del país (18° - 33° S) es caracterizada por un megathrust mucho más inestable, propiciado por un ante-arco denso y pesado. El sur (33° - 44° S), sin embargo, es gobernado por un régimen condicionalmente estable, lo cual es causado por un antearco más liviano y menos denso. Esto explicaría porqué el norte de Chile pareciera experimentar terremotos de mediana magnitud pero alta recurrencia temporal, al contrario del sur donde gigantes terremotos sacuden el margen, pero con una recurrencia menor. Interesantemente, de los segmentos unitarios obtenidos se infieren potenciales asperezas sísmicas que se correlacionan con la presencia de estructuras oceánicas y corticales de la placa de Nazca y Sudamérica, respectivamente.

Adicionalmente, del modelo de segmentación, se logran distinguir posibles barreras sísmicas. A través de simulaciones numéricas del ciclo sísmico, se demuestra que la naturaleza física de barreras sísmicas puede ser generado por la presencia de material *Velocity Weakening* que promueve un comportamiento condicionalmente estable. Los múltiples patrones de deslizamientos albergados por estas barreras son similares a los observados en fallas reales, apoyando la idea de que nuestra conjetura de barreras condicionalmente estables es plausible. Por otro lado, las simulaciones muestran que estas barreras pueden estar acopladas, desafiando la visión de que solo asperezas sísmicas pueden desarrollar este comportamiento. Además explicando la observación de porque algunos sectores reconocidos como

barreras presentan un alto acople. Usando la teoría de mecánica de la fractura, se logra construir un parámetro adimensional para medir la eficiencia de las barreras y el cual se puede aplicar para anticipar el comportamiento de barreras naturales. Esto tiene un fuerte impacto en los avances sobre modelos físicos de riesgo sísmico.

Esta tesis proporciona una base teórica que explica la relación entre la estructura geológica del ante arco y la estructura friccional del megathrust, sugiriendo además que esta última es persistente a escala geológica. Básicamente, la presencia de montes marinos, ridges asísmicos y/o zonas de fractura generarían una distribución heterogénea de la resistencia de la falla a esfuerzos. Similar sería el efecto de la estructura de la densidad del ante-arco mediante su efecto en el estrés normal, explicando entonces los mecanismos detrás de la segmentación sismogénica en el país y otras zonas de subducción. Finalmente se valida nuestra hipótesis a través de una amplia discusión al final de este manuscrito y se discuten los alcances de este trabajo en el riesgo sísmico del país y la física de terremotos como también la segmentación en fallas reales.

Abstract

Chilean-type subduction zones occur in convergent margins between an oceanic and continental plate. On the plate interface is found the megathrust, where the seismogenic zone takes place. Here, more devastating earthquakes happen, the so-called subduction zone earthquakes. They are explained by sudden dislocations once the fault strength is overcome due to the tectonic forces driven by the collision between both plates. It has been reported that earthquakes respond to elastic strain loading and unloading, a process known as the seismic cycle, which ultimately promotes relative slip between the upper and lower plate. The maximum slip tends to occur in high friction zones known as “seismic asperities” whereas zones of low friction and therefore reduced slip are “seismic barriers”. The high friction on the asperities provokes both plates to get stuck, a feature known as coupling, prone to the zone to accumulate slip deficit that eventually must be released. In general, seismic barriers are related to zones of low coupling. This heterogeneous frictional property distribution can be understood as the megathrust frictional structure.

Given the recent instrumental records and geological observations, it has been possible to observe that segments of different extensions seem to be characterized by seismic cycles of distinct duration. This characteristic has been attributed to the “seismic segmentation”. Because the seismic risk is controlled by the maximum size of a rupture, earthquake segmentation along subduction zones is significantly important. Likely the seismic segmentation is a reflection of an heterogeneous frictional structure of the megathrust. However, the underlying mechanisms controlling the megathrust frictional structure and thus seismic segmentation are not fully understood. Insights regarding the multiple factors modulating the frictional structure come from the correlation between geological features of both plates (fore-arc geological structure) and the distribution of earthquakes.

In this thesis it is hypothesized that “the geological structure of the fore-arc exerts control on the megathrust frictional structure”. To validate this statement, it is proposed to use the Chilean margin due to its extended register of earthquakes, spanning at least 500 years of records. Further, because of its varied geological

environments, Chile is a perfect natural laboratory to investigate earthquake phenomena.

Through the Principal Component Analysis (PCA) the spatial correlation between different geophysical/geological proxies, usually used to illuminate the frictional structure, is estimated. It is shown that the first component (PCA) exhibits a clear relation with the seismicity distribution, suggesting that the first principal component represents the first-order frictional structure of the Chilean megathrust. From this, the first formal segmentation model for the Chilean margin is constructed, which can be applied to improve earthquake hazard assessments. Our results indicate that the north of Chile (18° - 33° S) is characterized by a very unstable megathrust caused by a heavy and very dense fore-arc. On the other hand, the south of Chile (33° - 44° S) would be governed by a conditionally stable regime. This explains why the northern part of the country hosts several intermediate magnitude earthquakes with a high recurrence whilst the south is the net of huge ruptures. Notably, the unitary segments derived from the segmentation models are inferred to display the presence of seismic asperities. Remarkably, their distribution is strongly associated with the localization of geological features of the Nazca and South American plates, respectively.

Additionally, from the segmentation model, several seismic barriers are interpreted. By running numerical simulations of the seismic-cycle, it is demonstrated that the physical nature of seismic barriers can be explained by the presence of Velocity Weakening material promoting a conditionally stable regime. Indeed, the ample slip pattern displayed by conditionally stable barriers is similar to that reported on natural barriers. Further, the seismic barriers in the simulations can be coupled, challenging the idea that only seismic barriers can present this feature. Likewise, some natural barriers are reported to lie on zones of high coupling. Considering fracture mechanics, a non-dimensional parameter is constructed to estimate the barrier efficiency (ability to stop earthquakes). This parameter can be applied to natural barriers to anticipate their slip behavior, impacting on physics-based hazards assessments.

Regarding the interplay between geological and frictional structure, this thesis provides a theoretical basis to explain possible feedback processes involved. Basically, the presence of seamount chain, aseismic ridges, and fracture zones would cause the fault to experience an heterogeneous strength. Similarly, the fore-arc density structure by modulating the normal stress above the plate interface may be impacting the fault strength, explaining the possible mechanisms behind earthquake segmentation in Chile and other subduction zones. Accordingly, because the geological structure is a long term feature of the margin, it is shown that the frictional structure is a persistent feature and thus the seismic segmentation prevails over time.

1. Introduction	17
1.1 Subduction zones and megathrust earthquakes	17
1.2 Illuminating the frictional structure	19
1.3 Persistence of seismic segmentation and hazard assessments	22
1.4 Chile as a study case	23
1.6 Contents and Structure of the thesis	26
1.6.1. Methods Chapter 2 (Review)	27
1.6.1.1 Proxies construction	27
1.6.1.2 Principal Component Analysis	29
1.6.2 Methods Chapter 3 (Review)	29
1.6.2.1 Numerical simulations	29
1.6.2.2 Fracture mechanics	30
2. Frictional Segmentation of the Chilean Megathrust From a Multivariate Analysis of Geophysical, Geological, and Geodetic Data	32
2.1 Introduction	34
2.2 Seismotectonic Setting of the Chile Margin	37
2.3 Methods	39
2.3.1. Principal Component Analysis	40
2.3.2 Computation of Proxies for Megathrust Frictional Structure	41
2.3.2.1. Residual Gravity Anomaly Δg	41
2.3.2.2. Effective Basal Friction Coefficient b	42
2.3.2.3. Degree of Interseismic Geodetic Locking Λ	45
2.4. Results	45
2.5. Discussion	50
2.5.1. Relating Trench-Perpendicular PCA Tendencies With Megathrust Seismogenic Zone	50
2.5.2. Along-Trench PCA Tendencies and Segmentation of the Chilean Megathrust	56
2.5.2.1. Large-Scale (103 km) Segmentation and the Role of Contrasting Frictional Stability Regimes	57
2.5.2.2. Small-Scale (<102 km) Variability and Seismic Segmentation Model for the Chilean Margin	60
2.5.3. Structural Controls on Seismic Segmentation	67
2.6 Conclusions	71
3. Slip behavior of velocity-weakening barriers	75
3.1 Introduction	76
3.2 Simulating the earthquake cycle around VW barriers	79
3.3 Results	80
3.3.1 Diverse slip patterns on the central VW patch	80
3.3.2 From aseismic to seismic slip on VW barriers	82
3.3.3 Fracture mechanics on VW barriers	83
3.4 Discussion	86
3.4.1 Interseismic coupling pattern on VW barriers	86
3.4.2 Implications for structural control on earthquake behavior	87
3.5 Methods	89

3.5.1	Earthquake cycle model setup	89
3.5.2.	Energy balance for earthquakes	91
3.5.3.	Barrier efficiency	93
3.5.4.	Constructing	94
3.5.5.	Calibration of effective rupture width in the 2.5D model	95
3.5.6.	Slip rates thresholds defining slip behaviors	96
3.5.7.	Interseismic coupling (ISC)	96
4.	Discussion	98
4.1	Frictional structure of the Chilean megathrust and earthquake segmentation	98
4.1.1	Physical nature of asperities	98
4.1.2	Physical nature of barriers	100
4.1.3	Fracture mechanics, implication on earthquake segmentation	101
4.1.4	Seismogenic width effect on long ruptures	103
4.2	Relation between the frictional structure and geological features, implications on spatial and temporal persistence of seismic segmentation	104
4.3	Long and short term earthquake behavior at first order segmentation scale	108
4.4	Implication (Application) on seismic potential	110
5.	Conclusions	117
6.1 (A1)	Supplementary Material Chapter 1	119
	Table S1.	122
	Figure S1 and Figure S2.	123
6.2 (A2)	Supplementary Material Chapter 2	127
	Predicting barrier efficiency	133
	Estimating the efficiency of natural barriers	137
6.3 (A3)	Seismogenic width effect on seismic barriers	139
7.	Thesis References	143

Figure index

Chapter 1

Figure 1.1	Illustration subduction zone	18
Figure 1.2	Chilean tectonic setting	24
Figure 1.3	Schematic representation of a Chilean type subduction zone	25

Chapter 2

Figure 2.1	Seismotectonic setting of the Chilean subduction zone	38
Figure 2.2	Derivation of Residual Gravity Anomaly by the Principal Component Analysis (PCA) method	43
Figure 2.3	Spatial distribution of the three proxies of the frictional structure along the Chilean megathrust inside the area considered for this study (i.e., as covered by the 150 km long trench-perpendicular profiles used for the principal component analysis)	46
Figure 2.4	Results of the combined multiproxy Principal Component Analysis analysis	47
Figure 2.5	Reconstructed maps of the three frictional proxies	49
Figure 2.6	Relationship between trench-perpendicular tendencies of frictional proxies, seismic behavior and schematic subduction zone structure	54
Figure 2.7	Relationship between along-trench tendencies of frictional proxies and seismic behavior	58
Figure 2.8	Seismic segmentation model	62
Figure 2.9	Comparison between residual gravity, density and geologic structure	69

Chapter 3

Figure 3.1	Conceptual model and numerical simulation setup	78
Figure 3.2	Results of seismic cycle simulations	81
Figure 3.3	The diversity of slip behaviors in VW barriers	83
Figure 3.4	Rupture arrest conditions and barrier efficiency based on fracture mechanics	85

Chapter 4

Figure 4.1	Seismotectonic illustration of Central and Southern Andes	106
Figure 4.2	Time dependent seismic hazard assessment (Valdivia segment)	113
Figure 4.3	Time dependent seismic hazard assessment (Iquique, Antofagasta and Copiapo segments)	114
Figure 4.4	Time dependent seismic hazard assessment (Maule and Valparaíso segments)	116

Chapter 6

Figure S1	Empirical Orthogonal Functions	124
Figure S2	Reconstructed spatial distributions of different locking grids	125
Figure Extended data 1	The diversity of slip behavior in VW barrier types	128
Figure Extended data 2	Seismic cycle simulations of frequent barriers	129
Figure Extended data 3	Long-term interseismic coupling in the CVWP	130
Figure Extended data 4	Reference seismic cycle simulation	131
Figure S1	Stress drop dependency with D_c , σ_n or barrier length L_B observed from the earthquake simulation	134
Figure S2	G_o and G_c mean values from simulations (originally used to estimate λ , Methods 3.5.3) compared with G_{cp} and G_{1opp} proxies mean values calculated considering stress drop dependency with D_c , σ_n and barrier length L_B [Figure S1]	135
Figure S3	Measured and predicted λ compared with the probability P (Percentage of events breaking the barrier)	136
Figure S4	Slip deficit for the Maule earthquake area	138

Table index

Chapter 6

Table S1	Vertices of unitary seismic segments	123
----------	--------------------------------------	-----

1. Introduction

1.1 Subduction zones and megathrust earthquakes

Subduction zones take place where two tectonic plates collide, being one of them subducted below the other (Fig. 1.1). The subducted and overriding plates often correspond to an oceanic and continental plate respectively, such as the Chilean and Cascadian margin, for instance. The upper region of the contact between both plates is known as the megathrust and it hosts the so-called seismogenic zone (Fig. 1.1). Because of the huge tectonic forces interacting between both plates and frictional processes, they may get coupled, leading to the megathrust and elastic medium to accumulate huge deformation, elastic strain and slip deficit (Lamb, 2006; Meade and Conrad, 2008). However, this accumulation of elastic energy can not be stored in the medium indefinitely and it must be released through some mechanisms once the strength of the seismogenic zone is overcome. Notice that the strength depends mainly on normal stress and friction properties distribution, here-after call the frictional structure (Davis et al., 1983). The main process occurring are the megathrust earthquakes and they can be understood as sudden dislocation on the seismogenic zone releasing both, part of the slip deficit and elastic deformation.

They are explained by the elastic rebound theory (Mitiyasu, 1976) and are characterized by irradiate seismic waves to the medium, causing often huge damage on human population, that's why subduction earthquakes are cataloged as one of the most devastating hazards over the world. As observations and earthquake records have been increasing, it has been proposed that earthquake occurrence is a process of load unloading of stresses on the megathrust, a process known as the seismic cycle (Wesson et al., 2015). Interesting, different parts of a subduction margin along strike, seem to be characterized by distinct seismic cycle time duration, which implies that probably stresses on the megathrust are not equally distributed and thus provoking earthquakes of different magnitude and recurrence along strike. This distribution of earthquakes of different size filling distinct portions of the margin was studied in the early 70s and the concept to refer to it was introduced as seismic segmentation (Schwartz and Coppersmith, 1984). It was proposed that such segments were characterized by hosting the largest earthquake known as a

characteristic earthquake, which was expected to be persistent in space time (Sykes and Nishenko, 1984).

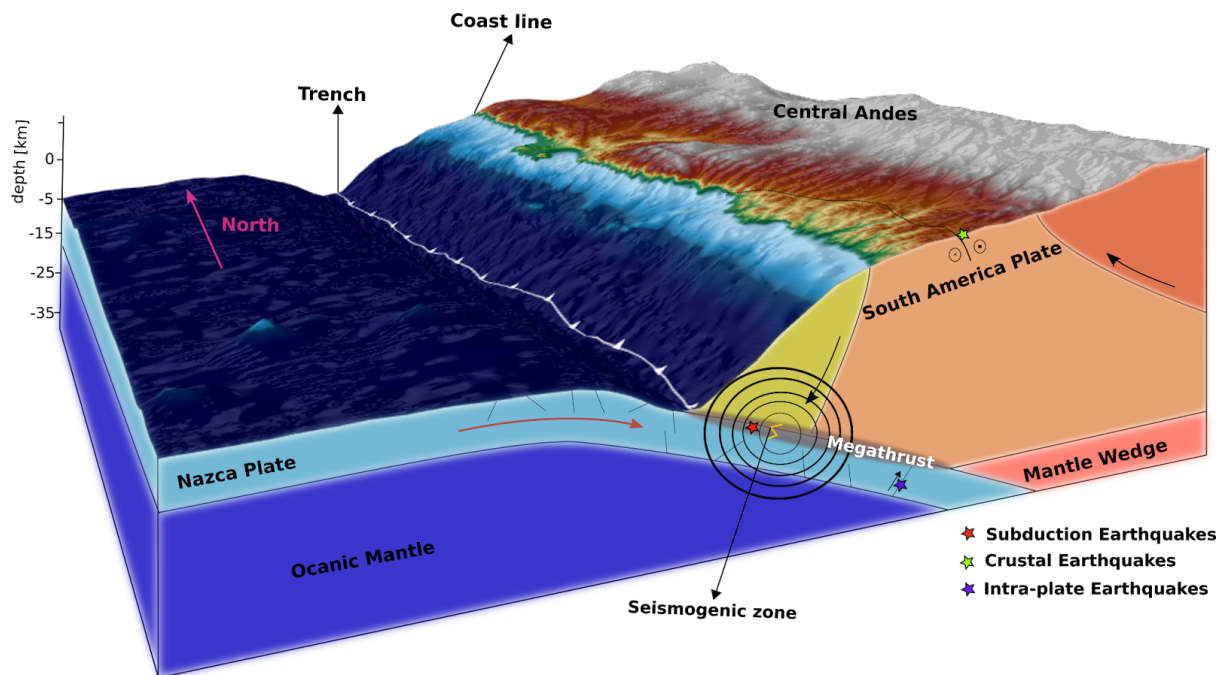


Figure 1.1 Illustration subduction zone: The convergence between Nazca and South America plates. On top of a shaded-relief map of topography and bathymetry (GEBCO_2019 grid). Pink arrow depicts the convergence rate between Nazca and South America plates (Kendric et al., 2003). In soft and dark blue the oceanic plate and oceanic mantle respectively. Brown and red colors depict the continental plate and mantle wedge. Orange represents the continental basement and yellow the outer fore-arc. Gray ellipse the contact plate or plate interface where the megathrust and seismogenic zone are. Black contour lines showing the irradiated seismic waves from a subduction earthquake hypocenter.

However, as time passed, it was observed that such segments were able to host earthquakes of smaller size before the characteristic earthquakes occurred, implying that the frictional structure of the megathrust was heterogeneous. An initial model to explain these observations was proposed in the early 80s by Lay and Kanamori (1981), the so-called “asperity model”. Basically, regions of the megathrust related to high friction remain coupled during prolonged time -interseismic phase- and they are defined as seismic asperities, which accumulates large slip deficit. The slip deficit is released in a sudden dislocation through an earthquake lasting several seconds even minutes, a stage of the cycle known as coseismic phase. Afterwards, the areas surrounding the asperities, often characterized by presenting lower friction,

accommodate slip deficit slowly by stable slip mechanism during several years. This is defined as the postseismic stage and it is the end of a seismic cycle. Finally, the seismogenic zone gets coupled, initiating the interseismic phase, and therefore the seismic cycle again.

The asperity model was useful to understand why sometimes seismic segments were broken by smaller earthquakes. The basic idea is that during small earthquakes isolated asperities fail whereas bigger events likely involve the interaction of more asperities. The cause of preventing earthquakes propagating from one asperity to another was explained by the presence of seismic barriers, recognized as areas of low friction promoting rupture arrest (Aki, 1983). Therefore, it was suggested that probably large seismic segments were characterized by the presence of barriers separating asperities, which during some stage of the seismic cycle all were synchronized and slipped, provoking a huge earthquake, the characteristic earthquake. Moreover, the term characteristic earthquake was losing validity because it was observed that seismic segments started to be the net of seismic events bigger than the characteristic earthquake and usually similar earthquakes breaking seismic segments seemed not to share the same properties between them, such as the amount of slip or irradiated energy (Rong et al., 2003). Nevertheless, worldwide earthquake records on different subduction zones would seem to exhibit a spatial seismic segmentation of first order (Philibosian, B. & Meltzner, 2020), implying a segmented frictional structure across megathrusts which probably respond to a heterogeneous distribution of fault strength. Changes on the mechanical properties of the elastic medium, tectonic setting variations, difference on plate velocity convergence, plate ages, fault roughness, seismogenic width, among others, have been proposed to explain such heterogeneous megathrust frictional regime (Wirth et al., 2022), yet the dominant factors are still debated.

1.2 Illuminating the frictional structure

The frictional regime on faults can be addressed by considering the rate and state friction law. This offers a theoretical framework able to describe the multiple frictional regime that a fault can host. This law was introduced from laboratory rock

experiments showing a direct relation between friction and slip velocity (Dieterich, 1979; Tullis, 1988). The mathematical expression of this law can be written as;

$$\frac{\tau}{\sigma_n} = \mu^* + a \ln\left(\frac{V}{V^*}\right) + b \ln\left(\frac{V^* \theta}{D_c}\right) \quad (1.1)$$

$$\frac{d\theta}{dt} = 1 - \frac{V\theta}{D_c} \quad (1.2)$$

Here τ and σ_n are the shear strength parallel to the fault and the normal stress perpendicular to the fault, respectively, V the sliding velocity and θ a state variable, μ^* and V^* are reference values for friction and velocity, respectively, D_c is a critical slip distance for state evolution, and a and b are positive coefficients controlling the velocity and state effects, respectively. The full spectrum of slip behaviors can be associated to two main different frictional regimes, that is, how friction behaves depending on the fault slip velocity. If $a-b > 0$, Velocity Weakening behavior (VW) arises: after a sudden increase in velocity, the friction goes down, inducing slip acceleration, that is unstable slip, often related to earthquake nucleation and propagation. On the other hand, if $a-b < 0$, Velocity Strengthening (VS) behavior emanates: with increasing slip velocity, friction goes up, producing a slow down associated with earthquake arrest and stable slip. Importantly, there is a bifurcation in the VW domain controlling the frictional stability of the fault, modulated by a critical stress given by the following equation (Scholz, 1998):

$$\sigma_c = \frac{k D_c}{-(a-b)} \quad (1.3)$$

Here k is the stiffness of the media surrounding the fault. The fault moves under unstable sliding if $\sigma_c < \sigma_n$. When $\sigma_c > \sigma_n$, the fault can experience conditionally stable behavior, that is aseismic slip but shifting to unstable sliding under important normal stress perturbations triggered by fault slip conditions. Further, VW material has been proposed to govern the behavior of asperities whereas VS behavior would cause the barriers to stop earthquake rupture propagation. Despite the increased

knowledge on possible frictional regimes governing natural faults, the frictional structure controlling earthquake behavior remains poorly understood. How VW and VS material may interact and provoke the current spatial segmentation along subduction zones is controversial. Mapping this spatial organization and heterogeneous frictional structure and thus knowing what it is the frictional structure of megathrust is an issue since we can not measure it at the fault itself.

Different geophysical or geological proxies have been used to try to map how the frictional structure is organized on megathrust, for instance gravity anomalies, coastal geomorphology, seismicity distribution, among others (Song and Simons, 2003, Saillard et al., 2017, Legrand et al., 2012). The former evidenced that regions of negative gravity anomalies were correlated with areas experiencing large coseismic slip. From this, it was suggested that negative gravity anomalies were pointing out to zones of high friction, inducing the upper plate to be dragged towards major depths, provoking a negative gravity signature (Song and Simons, 2003). Consequently, high stress loading was built up and therefore earthquakes happened. However, later it was shown that both positive and negative gravity anomalies correlate with coseismic slip patches (Tassara, 2010; Bassett and Watts 2015a, 2015b). Hence, it was proposed that gravity anomalies were influencing vertical stress on the megathrust driven by density changes, which ultimately exert control on seismic behavior and seismic segmentation (Tassara, 2010). Similarly, geodetic observations have been used to describe kinematically the plate interaction through measuring the degree of locking on the megathrust (Moreno et al., 2010, Metois et al., 2016). That is how much of the convergence rate is accommodated by aseismic slip. High locking implies two very locked plates, related to seismic slip whereas low locking exhibits high creeping rates, that is stable slip. Since differences on slip behavior also have been shown to respond to frictional conditions on the fault (Rubin and Ampuero, 2005), locking has been used to map different frictional behavior on megathrusts too, for instance high creeping rates often are associated with VS material (Wang and Bilek, 2014). Further, locking patterns along the trench also report a segmented margin, usually showing a spatial correspondence between high locked patches and large coseismic slip (Loveless and Meade, 2011; Protty et al., 2014). Surprisingly, both gravity and locking proxies also seem to be linked to the geological structures of both plates (Wang and Bilek, 2014; Bassett and Watts,

2015a-2015b), supporting them that both geological and frictional structure might be connected through some process.

1.3 Persistence of seismic segmentation and hazard assessments

Likewise, how persistent the seismic segmentation can be is another open question. If we accept that gravity is a proxy to the frictional structure, and that gravity responds to long term mass variation of the forearc, then we could hypothesize that seismic segmentation could be persistent over geological time. Assessing this could be done by looking at the seismic record to see if the segmentation prevails over time. However, since the earthquake records of entire seismic cycles are lacking, the scientific community can not ensure with confidence that the current spatial segmentation is representative of the long-term behavior. However, some insights regarding whether the seismic segmentation is permanent is its correlation with tectonic features of both upper and lower plates (Loveless et al., 2010). Observations evidencing such correlation was that rupture areas of earthquakes were located close to incoming features of the oceanic plate, for instance seamount chains or aseismic ridges (Wang and Lin, 2022, Contreras-Reyes and Carrizo, 2011). Likewise, other rupture areas extension were delimited by crustal discontinuities and anomalous geomorphology such as crustal faults and peninsulas respectively (Collot et al., 2004; Melnick et al., 2009). Nevertheless, how these tectonic features, part of the geological structure, are impacting on the fault strength, which in turn depends on frictional and mechanical properties, remain poorly understood. Therefore, attempts on illuminating the frictional structure of the megathrust is essential to better comprehend the current seismicity pattern.

Importantly, although the characteristic earthquake concept has been invalidated throughout time, seismic segmentation has not. Seismic segments are important because they can provide the possible largest rupture extension that the segment can experience (Sykes and Nishenko, 1984). This could help to estimate the maximum earthquake size in a segment, which is a significant parameter controlling seismic hazard. Similarly, the recurrence time of earthquakes works as essential inputs on probabilistic models assessing potential rupture escenarios (Marinieri et al., 2021). Nonetheless, current knowledge of the return period of big earthquakes is

poorly constrained, being paleo and historical records the most used data to infer earthquake recurrence time (Cisterna et al, 2005). Therefore, unveiling whether current seismic patterns are permanent over broad time scales, can significantly help to improve mitigation measurements to avoid human casualties and destruction of

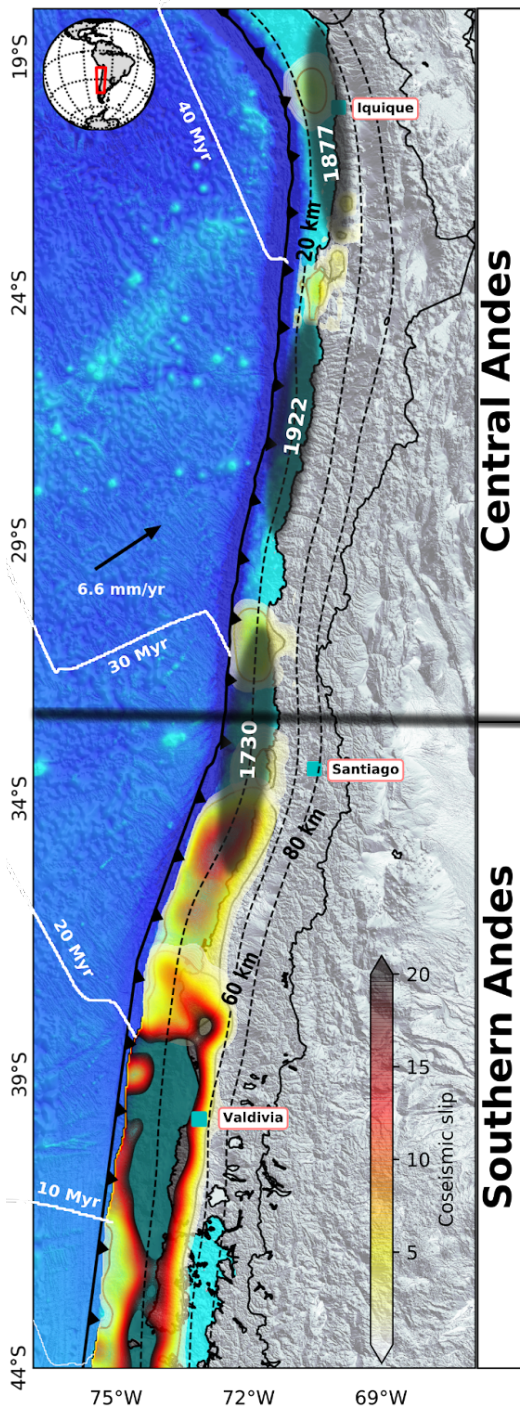
critical infrastructure. Likewise, counting with an estimation of possible segments size in a particular subduction zone together with their possible time dependent rupture potential is vital to advance on seismic hazard assessments. The former idea has been addressed recently by creating segmentation maps of several subduction zones, but considering only information of past earthquake records (Philibosian, B. & Meltzner, 2020). A possible issue coming from this is the bias originated by the short register time of seismic cycles. A practical solution would be to reproduce those segmentation models but using independent geophysical proxies, such as gravity and locking fields.

1.4 Chile as a study case

As it was previously mentioned, several are the subduction margins showing a first order seismic segmentation along strike, yet what are the mechanisms behind it are not fully understood. Evidence of this is clearly exposed on the Chilean margin. Previous works have shown that the Chilean megathrust is seismically segmented (Ruiz and Madariaga, 2018). For instance, historical and instrumental earthquake records seem to point out a clear difference between the north (18° - 33° S) and south (33° - 46° S) of Chile, implying a first order segmentation (Tassara, 2010).

In the former area, usually earthquakes are of moderate size (<8.5) and their recurrence time is ~ 100 years while in the latter, earthquakes tend to be larger considering both, magnitude and return period (Beck et al., 1998; Vargas et al., 2005; Leon et al., 2019; Kempf et al., 2020; Moernaut et al., 2018). It is possible that the previous observations are being caused by a heterogeneous distribution on properties of the megathrust, especially inducing important changes on asperities fault strength from north to south. Interestingly, northern and southern Chile also exhibit a sharp geological segmentation, being highly reflected by the presence of the Central and Southern Andes orogenic segments (Tassara et al., 2006; Tassara & Yáñez, 2003) (Fig. 1.2). An abrupt variation on cordillera altitude is the main feature

provoking the Andean Segmentation. This morpho structural correlation of the Andes with a first order seismic segmentation motivates us to investigate whether this observation is merely a coincidence or it responds to a physical interaction between the geological structure and frictional structure of the Chilean megathrust.



At the same time, another question arises; is it possible that there is a second or third order segmentation present along the Chilean megathrust? And if it does, how can we identify it and how much we can investigate its frictional regime. To investigate this, the Chilean margin offers an unique and ideal opportunity given ~500 years of seismicity historical records and well registered instrumental recent events (Fig. 1.2). Also, due to its varied and rich geological environments, we can explore how many differences in the geological structure might be influencing the earthquake patterns. Further, we could extrapolate our results to those subduction zones with similar geological characteristics.

Figure 1.2 Chilean tectonic setting: On top of a shaded-relief map of topography and bathymetry (GEBCO_2019 grid). Warm colors display the coseismic slip for most recent instrumental earthquakes (1960 Valdivia M9.5, 2010 Maule M8.8, Illapel 2015 M8.3, Atacama 1995 M8, Tocopilla 2007 M7.8 and Iquique 2014 M8.1. (Moreno et al., 2009, 2012, Bravo et al., 2019, Tilmann et al., 2016, Hayes et al., 2017, Motagh et al., 2009, Schur et al., 2014). Shade ellipses represent main seismic gaps (Beck et al., 1998; Carvajal et al., 2017; Comte & Pardo, 1991). White lines show the age

distribution for the Nazca plate (Muller et al., 2008). Black arrow depicts the convergence rate between Nazca and South America plates (Kendric et al., 2003). The right-hand side of the figure shows the extent and names of first-order segments recognized for the Andean margin (Tassara et al., 2006; Tassara & Yáñez, 2003).

1.5 Scientific Question, Hypothesis and Objectives

In this thesis we focus on solving two main aspects of the topics previously mentioned. What is the frictional structure of the Chilean megathrust? That is, how, VW and VS material, for instance, are organized in space to create the current earthquake pattern (Fig. 1.3). On the other hand, we propose to explore what is the link between long-term geological structure and frictional structure and how this link can give us insights on the natural persistence of the seismic segmentation in Chile and elsewhere (Fig. 1.3). Further, we could use the obtained information to discuss implications on seismic hazard.

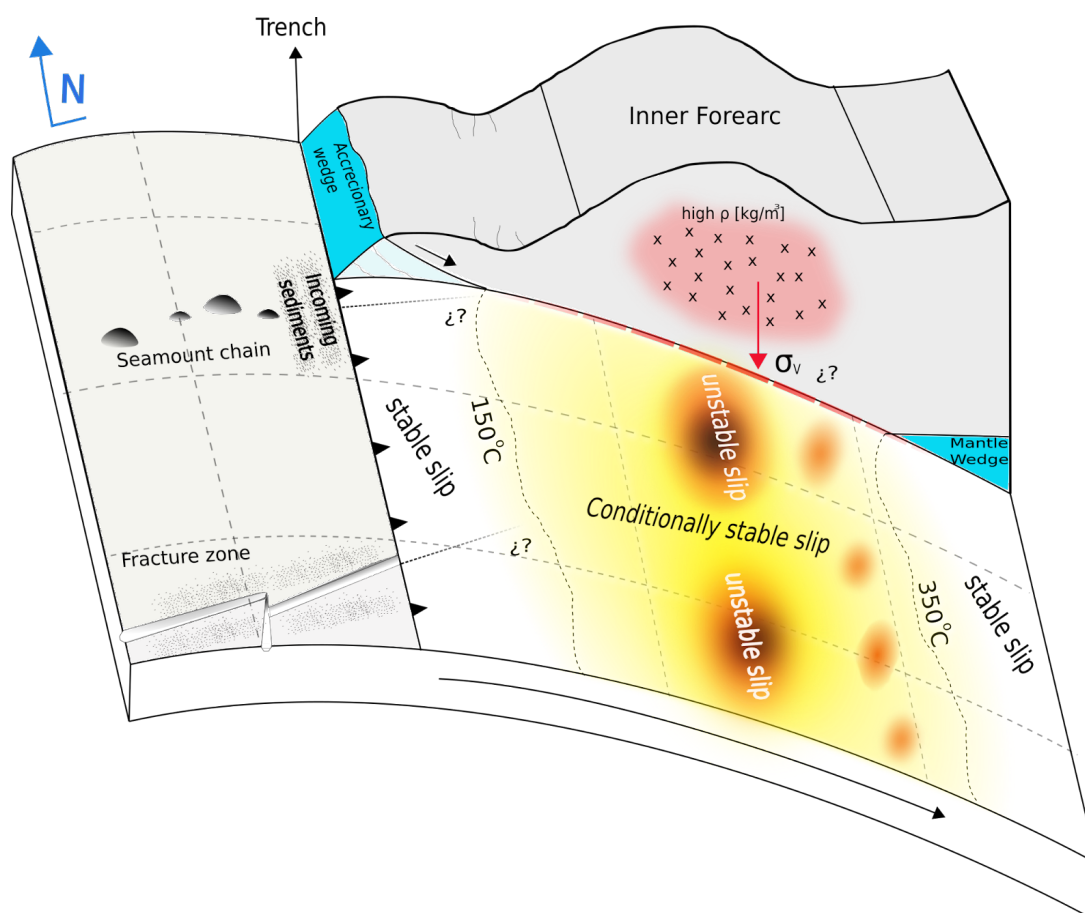


Figure 1.3 Schematic representation of a Chilean type subduction zone. Warm colors display the frictional structure with its different slip behavior. Dashed black lines represent the isotherms for 150°C and 350°C. Gray dotted regions show the presence of sediments favored by oceanic features. Red zone exhibiting a density anomaly within the inner forearc provoking an increase in vertical stress. Black arrow representing the motion direction of the oceanic slab. Note that interrogation symbols point out how different tectonic features might be controlling the frictional structure.

To guide this research, we propose the next hypothesis:

The geological structure of both converging plates exerts control on the frictional structure of the Chilean megathrust.

Testing this statement will be carried out by the following general and specific objectives.

General objective:

Understand through what physical mechanisms the different geological factors are influencing and/or controlling the megathrusts frictional structure (Fig. 1.3).

Specific objective:

1. Create a large database compiling all geophysical and geological available data for the Chile margin.
2. Characterize the frictional structure of the megathrust.
3. Identify the most important geological feature of the Chilean forearc
4. Estimate the correlation degree between both the geological and frictional structures along the Chilean margin.
5. Comprehend the multiple roles of geology on the frictional structure.

1.6 Contents and Structure of the thesis

The thesis is organized in 5 main sections. Chapter 1 is this introduction, which provides a basic theory and concepts to derive scientific questions and to identify the knowledge gap in the area reflected in our hypothesis. Additionally, in this Chapter we make a brief review of the methodologies carried out on this research that is expressed in one published paper presented as Chapter 2 and one submitted paper corresponding to Chapter 3. Then, the articles of Chapter 2 and 3 are presented in their original form. Chapter 4 is a discussion that attempts to put the main scientific findings in a larger perspective regarding seismotectonics in subduction zones with

implications for seismic hazard assessment. This follows in Chapter 5 by the main conclusions of the thesis.

The detailed methodology utilized in this thesis is fully described in the articles corresponding to Chapters 2 and 3. However, here it is a summarized review of methods to introduce the key concepts which will be helpful to both give an adequate context throughout the thesis reading and to see how they allow to fulfill the specific objectives.

1.6.1. Methods Chapter 2 (Review)

1.6.1.1 Proxies construction

The basic tool used in Chapter 2, correspond to the Principal Component Analysis (PCA), which uses an orthogonal transformation over observations of possible correlated variables in order to obtain a new set of coordinates of linearly uncorrelated variables that concentrate along their axes most of the covariance of the data. In our case, the possible correlated variables are gravity anomalies, basal friction and interseismic locking, all of them covering the entire Chilean margin. These geophysical and geological fields can be understood as proxies for the frictional structure of the megathrust and are constructed as follows.

The former was obtained by employing a novel method, particularly involving the Principal Component Analysis. In general, gravity anomalies are calculated by removing from the gravity field an averaged regional field in order to unmask anomalous zones (Song and Simon., 2003; Bassett and Watts, 2015a). However this method induces a bias since the average regional field may not be spatially representative of the entire region. Considering the PCA method, we proceed to obtain the first mode of the gravity field, which can be understood as a regional mean but contemplating important first order along strike variations; for instance the presence of the Andes cordillera and its changes in altitude parallel to the trench. Other features can be the trench itself and its configuration. These structures ultimately may mask some local anomalous zones related to short wave-length scale features, thus it is important to remove them in order to have less biased gravity anomaly field. Then, the first mode is extracted and the gravity anomaly is obtained.

Regarding basal friction, this procedure is carried out by considering the classical Non-Cohesive Coulomb Wedge (NCCW) theory (Dahlen, 1984; Davis et al., 1983). The NCCW was built through a force balance between the frictional strength of the megathrust and gravitational body forces inside the wedge, which can be related to the taper angle of the fore-arc wedge. The taper angle is simply the sum between topographic slope angle and dip slab angle. Changes on the taper angles can come from variations on either wedge physical properties or effective basal friction. Importantly, since we expected that wedge geometry would be permanent over time, within our context, changes on taper angle are inferred to respond to deformation at geological time scale. Assuming that taper angle variations along strike reflect an heterogeneous basal friction distribution, we proceed to estimate a basal friction map. To do so, slope angles are calculated using a bathymetric-topographic grid along-strike provided by GEBCO data and dip angles are extracted from Slab 2.0 model (https://www.gebco.net/data_and_products/gridded_bathymetry_data/; Hayes et al., 2018). Once the values of taper angle are listed in a grid, we compute the basal friction by using equations 9, 17 and 19 of Dahlen (1984). Please note that gravity anomalies and basal friction are long-term proxies since they are constrained by geological properties such as density variations or wedge geometry respectively. Finally, the third proxy used in Chapter two is the Interseismic coupling (ISC) or locking. Locking is a kinematic description of the interaction between two plates, in our case the Nazca and Southamerica plates. It has been shown that locking maps describe the slip behavior that a fault can experience, ranging from aseismic to seismic pattern. Here we use a map of locking created by a concatenation at the scale of the whole Chilean margin of maps for specific regions presented by Moreno et al. (2010, 2012), Tilmann et al. (2016), and Li et al. (2015). All these maps were based on the same methodology, that is, the inversion of interseismic GPS velocity vectors to backslip (Savage, 1983) at the megathrust via Green's functions that are computed on the base of a unique 3D finite element elastic model. Therefore, these individual maps are fully compatible and can be integrated into a coherent image of interseismic locking along the entire margin. Here we emphasize that ISC is a short term proxy because the used GPS data, span for solely two decades.

1.6.1.2 Principal Component Analysis

Once we have built the three proxies of long and short term, we are ready to subject them into the PCA framework. We consider trench-perpendicular profiles of a common length that are distributed along the trench axis and we use them to interpolate the proxies and thereby to have them equally distributed in space. By concatenating all the fields into a singular matrix, we compute the covariance matrix, which allows us to calculate the singular values and eigen vectors. These are the Principal components (PCs) and Empirical Orthogonal functions (EOFs) respectively. Principal Components, each of them associated with a particular mode k , provide information on the trench-perpendicular variability of the along-trench pattern informed by a given EOF. Further, the k modes explain a particular percentage of the covariance between the three proxies. In addition, it is possible to map the first-order common spatial distribution of each proxy as informed by the first k modes considered in the analysis. Finally, EOFs, PCs and the first three modes are used in Chapter 2 to investigate whether along-strike and perpendicular trench variations of the fields are correlated with seismic patterns over the Chilean subduction zone.

1.6.2 Methods Chapter 3 (Review)

1.6.2.1 Numerical simulations

Numerical simulation of earthquake cycles are carried out in order to explore under what condition, VW patches can behave as seismic barriers. To do so, we used the QDYN software (Luo et al., 2017a) which allows us to perform quasi-dynamic earthquake-cycle simulations. Our model setting consists in a planar fault mimicking a typical subduction geometry, which is loaded by uniform steady slip at depth beyond its width. We capture the essence of the 3D fault problem while keeping the computations affordable by doing 2.5D simulations: we model a 1D fault in a 2D elastic medium. The fault is governed by the RSF law with the aging law and it is characterized by the presence of a conditionally stable patch surrounded by two very seismic asperities. Our model considers pure dip-slip and frictional properties and normal stress are variable along strike, specifically within the conditionally stable zone or Central Velocity Weakening Patch (hereafter CVWP). We run dozens of simulations by varying the critical distance D_c and normal stress in the CVWP to explore whether these changes promote earthquake arrest. In particular, we

performed one set of simulations varying D_c between 0.1 and 0.4 m and another set varying σ_n between 95 and 400 MPa. The simulations span a large number of earthquake cycles over a period of ~ 9 kyr and ~ 10 kyr, depending if D_c or σ_n are varied respectively. Our numerical results are summarized mainly in slip distributions in both space and time as locking considering slip rate in each point of the fault. Likewise, we quantify the ratio between aseismic and seismic slip at each fault location in order to describe the slip behavior of the CVWP.

1.6.2.2 Fracture mechanics

To gain more insights on earthquake physics, we found useful to recur to Linear Elastic Fracture Mechanics (LEFM), which provides a theoretical framework to study rupture propagation and arrest. Whether an earthquake can break through a barrier depends on the balance between the mechanical energy available in the incoming rupture (its static energy release rate G_o) and the energy dissipated by slip in the barrier (the fracture energy G_c). Earthquakes propagate if $G_o \geq G_c$; otherwise they stop (Fossum and Freund, 1975). In order to verify this arrest condition, the energy quantities are calculated for all earthquakes interacting with the CVWP, either by arresting within it or crossing it totally. Other important quantity is the asperity energy release rate denoted as G_{oi} , which arise from a theoretical analysis and it depends directly on squared stress drop, length asperity and it is inversely proportional to shear modulus.

LEFM is used to quantify the barrier efficiency, that is the ability of the CVWP to prevent earthquake propagation. We approximate G_o by assuming uniform stress drop in the asperity, $\Delta\tau_a$, and in the barrier, $\Delta\tau_b$, which leads to an energy ratio defined as $\Gamma(\frac{l}{l_o}, \frac{\Delta\tau_b}{\Delta\tau_a}, \frac{G_c}{G_{oi}})$, where l and l_o are the rupture and asperity lengths respectively. The equilibrium condition $\Gamma = 1$ gives a non-dimensional equation of the form

$$f\left(\frac{l}{l_o}, \frac{\Delta\tau_b}{\Delta\tau_a}, \frac{G_c}{G_{oi}}\right) = 0, \quad (1.4)$$

Thus the normalized rupture arrest length $\frac{l}{l_o}$ is controlled by the energy ratio $\frac{G_c}{G_{oi}}$ and

the stress drop ratio $T = \frac{\Delta\tau_b}{\Delta\tau_a}$:

$$\frac{l}{l_o} = g\left(\frac{G_c}{G_{oi}}, T\right) \quad (1.5)$$

This particular example suggests that the resistance of a barrier to rupture penetration in general depends on the two non-dimensional parameters $\frac{G_c}{G_{oi}}$ and T .

2. Frictional Segmentation of the Chilean Megathrust From a Multivariate Analysis of Geophysical, Geological, and Geodetic Data

Chapter 2 corresponds to the first manuscript within the tesis's context. The article was submitted to the *Journal of Geophysical Research* on July 23th, 2020 and accepted on April 28th, 2021. (Published on May 10th, 2021)

Cite: Molina, D., Tassara, A., Abarca, R., Melnick, D., & Madella, A. (2021). Frictional segmentation of the Chilean megathrust from a multivariate analysis of geophysical, geological, and geodetic data. *Journal of Geophysical Research: Solid Earth*, 126, e2020JB020647. <https://doi.org/10.1029/2020JB020647>

Frictional Segmentation of the Chilean Megathrust From a Multivariate Analysis of Geophysical, Geological, and Geodetic Data

Diego Molina ^{1,2}, Andrés Tassara ^{1,2}, Rodrigo Abarca ³, Daniel Melnick ^{2,4}, and Andrea Madella ⁵

1 Departamento Ciencias de la Tierra, Facultad de Ciencias Químicas, Universidad de Concepción, Concepción, Chile,

2 Millennium Nucleus The Seismic Cycle Along Subduction Zones CYCLO, Valdivia, Chile,

3 Departamento de Geofísica, Facultad de Ciencias Físicas y Matemáticas, Universidad de Concepción, Concepción, Chile,

4 Instituto de Ciencias de la Tierra, TAQUACh, Universidad Austral de Chile, Valdivia, Chile,

5 Institut für Geowissenschaften, Universität Tübingen, Tübingen, Germany

Abstract

We present a formal seismic segmentation model of the Chile Margin derived from a multivariate analysis of gravity anomalies, basal friction and interplate locking from GPS velocities. These independent proxies of the frictional structure along the megathrust integrate over timescales of 10^1 – 10^7 years. We analyze their covariance using Principal Component Analysis (PCA) and extracting the Empirical Orthogonal Functions (EOFs) and Principal Components (PCs). We find that (a) the first and first + second PCA modes for the triple combination of the proxies explain (respectively) 41.4% and 69.4% of the total variance and (b) the first-order spatial

pattern of each isolated proxy is largely reproduced when it is combined with the other two proxies. This suggests that the three proxies share a first order along-trench tendency that must be connected through a common physical process. Comparing our results with rupture areas of earthquakes and using the rate-and-state friction theory, we infer that trench-perpendicular PCs reflect the limits of the velocity-weakening (VW) seismogenic zone. Polarity changes in along-trench EOFs (mostly for gravity) mark changes between unstable and conditionally stable frictional regimes inside the VW zone and we used them to define the boundaries of 17 unitary segments. These segments correlate with first-order tectonic features of the Andes at $>10^3$ -km scales as well as with zones of multi-segment ruptures at 10^2 -km scale. We analyze the combined influence of subducting and upper-plate geologic features on the nature of persistent seismic barriers. Our results have implications for understanding seismotectonic processes along the Andean margin and elsewhere.

2.1 Introduction

Seismic asperities, as defined by the classic conceptual model of Lay and Kanamori (1981), are high-friction regions of a fault plane that are locked over the interseismic period and can suddenly slip during an earthquake, releasing the elastic strain accumulated around the fault. Asperities can be spatially limited by barriers, defined by Aki (1979) as geometric discontinuities and/or low friction areas segmenting the fault. After decades of research, there is now ample recognition that fault planes are formed by a heterogeneous distribution of asperities and barriers (e.g., Avouac, 2015; Bilek & Lay, 2002; Bürgmann, 2018; Kanamori, 2014; Lay et al., 2012; Seno & Yamasaki, 2003), although the factors and mechanisms controlling this frictional heterogeneity remain poorly understood. Moreover, a better comprehension of the relationship between this heterogeneous frictional structure, the along-strike segmentation of seismogenic faults and temporal recurrence of large earthquakes is fundamental to improve the assessment of seismic hazards (Gerstenberger et al., 2020; Kagan & Jackson, 1991; McCann et al., 1979; Sykes & Nishenko, 1984).

In the case of megathrust faults at subduction zones, geophysical, geomorphological and geodetic data have been used as proxies for mapping changes in the frictional structure along the interplate boundary. Some of these proxies can be associated with the long-term ($10^6 - 10^7$ yr) geological structure of both converging plates, as expressed by gravimetric and bathymetric anomalies (e.g., Bassett & Watts, 2015a, 2015b; Sobiesiak et al., 2007; Song & Simons, 2003; Tassara, 2010; Wells et al., 2003), seismic velocities (e.g., Hicks et al., 2014; Hua et al., 2020; Liu & Zhao, 2018; Yamamoto et al., 2014) and friction computed from the Coulomb wedge theory (e.g., Dahlen, 1984; Cubas et al., 2013; Fagereng, 2011). At an intermediate time-scale ($10^3 - 10^5$ yr), forearc morphology and spatially varying uplift rates of Quaternary marine terraces have been

used to infer trench-parallel variations in megathrust friction that can be related to earthquake segmentation (e.g., Jara-Muñoz et al., 2015; Marshall & Anderson, 1995; Melnick et al., 2009; Saillard et al., 2017). Other proxies are derived from geodetic data (e.g., Burgmann et al., 2005; Chlieh et al., 2008; Loveless & Meade, 2011; Moreno et al., 2010) or the spatio-temporal distribution of seismicity (b-value; e.g.,

Legrand et al., 2012; Rodríguez-Pérez & Zuñiga, 2018; Schurr et al., 2014; Tormann et al., 2015; Wiemer & Wyss, 1997) and therefore may be related to the frictional structure at short time-scales ($10^0 - 10^2$ yr). If the first-order frictional structure of the fault plane is time-independent, then all these different proxies should be spatially correlated, implying that the emerging distribution of asperities and barriers is persistent over many seismic cycles. Since each individual proxy is linked with the frictional structure of the fault through a particular mechanism, the recognition of a common spatial variability can be used not only to probe the persistency of the frictional structure over time but also to illuminate the physical nature of asperities and barriers. In this contribution, we aim to test these hypotheses using the Chile Margin as case study, by performing a multivariate spatial analysis of three independent proxies: (a) gravity anomalies; (b) interseismic geodetic locking; and (c) basal friction computed from wedge taper theory. In order to establish an adequate framework for this article, we offer here a brief review on the basic concepts behind these three proxies.

1. Gravity anomalies: It has been suggested that gravity anomalies along subduction zones highlight the location of asperities and barriers (Bassett & Watts, 2015a, 2015b; Li & Liu, 2017; Song & Simons, 2003; Wells et al., 2003). Song and Simons (2003) proposed a global correlation between large coseismic slip and negative trench-perpendicular gravity anomalies and argued that these regions correspond to asperities where high megathrust friction can drag down the upper-plate crust inducing low gravity (a view also shared by Wells et al., 2003 and Llenos & McGuire, 2007, among others). In contrast, Sobiesiak et al. (2007) found a local relationship between positive gravity and large slip for the 1995 Mw8 Antofagasta (North Chile) earthquake, and Tassara (2010) suggested a dichotomy with large coseismic slip associated with gravity highs and lows in the northern and southern parts of the Chile Margin, respectively. The latter is interpreted as mainly related to variations in the upper-plate density distribution associated with the geological structure. A similar conclusion was reached by Bassett and Watts (2015a, 2015b) and Bassett et al. (2016) by comparing gravity anomalies and seismogenic parameters at several subduction zones.

2. Geodetic locking: Another observational proxy that has been largely used to infer a spatial variability of megathrust frictional properties at short time-scales is the degree of geodetic fault locking (or interplate coupling) that can be inverted from satellite-based observations (mostly GPS and InSAR) of upper plate surface deformation during the interseismic period (e.g., Burgmann et al., 2005; Chlieh et al., 2008; Loveless & Meade, 2011; McCaffrey et al., 2002; Metois et al., 2012, 2016; Moreno et al., 2010, 2012; Wallace et al., 2004). This proxy is based on a kinematic description of plate subduction, where landward surface velocities are inverted into the backslip (downward) velocity along the megathrust assuming this as a dislocation inside an elastic media (Okada, 1985; Savage, 1983). Patches of high interseismic locking (i.e., those having a backslip velocity close to convergence velocity) can be inferred to represent high friction asperities that could be prone to slip in a future earthquake, an interpretation that has been actually confirmed in the case of recent large earthquakes (e.g., Loveless & Meade, 2011; Li et al., 2015; Moreno et al., 2010; Tilmann et al., 2016).

3. Megathrust friction could be estimated from the trench-perpendicular geometry of the forearc wedge, that is, from its topographic slope and slab dip angle, when this geometry is considered into the framework of the theory of critically tapered Coulomb wedges (Davis et al., 1983; Dahlen, 1984; Wang & Hu, 2006). Under the assumptions that the wedge is on the verge of failure (i.e., it is in a critical state where basal shearing is in equilibrium with the internal deformation of the wedge) and that material properties inside the wedge are known, it is possible to infer a value of basal friction. This method has been applied to the Chile Margin (i.e., Cubas et al., 2013; Maksymowicz, 2015) and other subduction zones (Cubas et al., 2013; Fagereng, 2011; Koge et al., 2014), contributing with relevant information about the long-term relation between megathrust friction and the structure of the forearc.

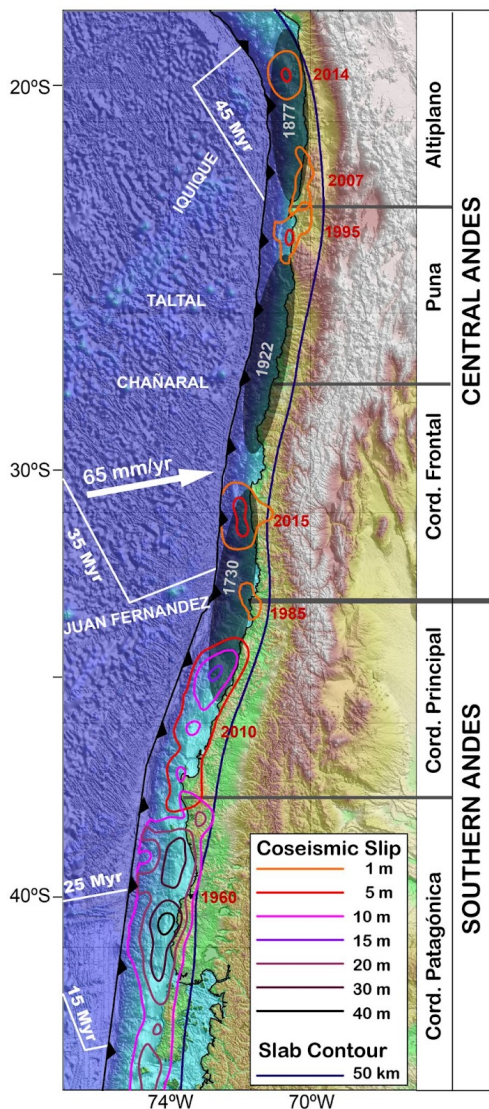
In this contribution, we develop a novel statistical approach based on the Principal Component Analysis (PCA) method in order to quantitatively determine the degree of correlation between these three proxies by evaluating their common spatial variability along the Chilean subduction zone. After a brief description of the seismotectonic setting, we explain the basis of the PCA approach as well as the methods used for the computation of each proxy. We then describe the resulting maps of gravity anomaly, locking degree, and basal

friction, focusing on the presentation of the reconstructed fields as derived from the first common mode of each proxy determined by the PCA analysis. The results are discussed in the context of the ~500-year-long seismic history of the Chile Margin, which is one of the largest records at subduction zones (e.g., Philibosian & Meltzner, 2020). Given the occurrence of several great to giant instrumentally recorded events (e.g., Mw9.5 Valdivia 1960, Mw8.8 Maule 2010, Mw8.4 Illapel 2015, Mw8.1 Iquique 2014), a relatively simple geometry, and a well-understood plate tectonic context along 4,000 km, the Chile Margin is an ideal place to study the possible connections between the megathrust frictional structure and its seismogenic behavior. Based on this analysis, we propose a formal seismotectonic segmentation model for this subduction zone and discuss the implications for the nature of the frictional structure along the Chile Margin as well as for seismic hazard assessments along subduction zones elsewhere.

2.2 Seismotectonic Setting of the Chile Margin

The western margin of South America is dominated by the Andean cordillera, which can be considered the final product of a process of subduction orogeny that started during the Paleozoic along the active margin of Gondwana (e.g., Charrier et al., 2007). A Jurassic-Cretaceous magmatic arc along the Coastal Cordillera in the northern part of the margin is intruded into remnants of a Late Paleozoic paired intrusive-metamorphic subduction complex that is better preserved in the central and southern sectors of the Chilean forearc. The current morphostructural configuration and internal anatomy of the Andean margin has allowed to propose an along-strike segmentation (Folguera et al., 2018; Tassara et al., 2006; Tassara & Yáñez, 2003). The Chilean part of the margin studied here is characterized by two first-order segments called Central (5°–33°S) and Southern (33°–47°S) Andes that are further subdivided into several second-order segments (Figure 2.1).

The age of the Present-day convergence between Nazca and South American plates estimated by GPS measurements has an azimuth of 80°E (that is slightly oblique to the margin) and a rate of ~65 mm/yr (Kendrick et al., 2003). Nazca plate along the trench (Müller et al., 2016) decreases from a maximum of ~50 Myr around 20°S to 0 Myr at 46.5°S, where the Chile Rise subducts below the continent. Jumps in the



age of the ocean floor are associated with fracture zones (Figure 2.1) with a general azimuth of $\sim 70^\circ\text{E}$. Positive bathymetric anomalies correspond to seamounts chains including the Iquique, Taltal, Chañaral and Juan Fernández ridges (Figure 2.1). Some of these subducting features have been related to regions of anomalous coastal geomorphology (peninsulas and embayments), which could be associated to zones of decreased interseismic coupling at the megathrust and can act as barriers to seismic propagation (e.g., Melnick et al., 2009; Saillard et al., 2017). From a seismological perspective and considering the 500-year-long history of documented seismic events along the Chile Margin, this region is characterized by a high frequency of great to giant (moment magnitude M_w 8–9.5) megathrust earthquakes (e.g., Kelleher, 1972; Ruiz & Madariaga, 2018). Figure 2.1 shows the coseismic slip distribution of the greatest events instrumentally recorded during the XX and XXI centuries.

Figure 2.1: Seismotectonic setting of the Chilean subduction zone. On top of a shaded-relief map of topography and bathymetry (GEBCO_2019 grid: https://www.gebco.net/data_and_products/gridded_bathymetry_data/ gebco_2019/gebco_2019_info.html), we plot contours for the age of the oceanic Nazca plate (white lines with numbers; Muller et al., 2016), names of seamount chains (white names in capital letters), plate convergence vector (Kendrick et al., 2003), the trench axis (black thick line with triangles), the contour of 50 km depth of the subducted slab (purple thick lines; Hayes et al., 2018), estimated rupture length of historical great earthquakes associated with current seismic gaps (semi-transparent dark gray areas with year of the earthquake in light gray: Beck et al., 1998; Carvajal et al., 2017; Comte & Pardo, 1991), contours of coseismic slip of earthquakes occurred in years 1960 (Moreno et al., 2009), 1985 (Bravo et al., 2019), 1995 (Hayes, 2017), 2007 (Motagh et al., 2010), 2010 (Moreno et al., 2012), 2014 (Schurr et al., 2014), and 2015 (Tilmann et al., 2016). The right-hand side of the figure shows the extent and names of first- and second-order segments recognized for the Andean margin (Tassara et al., 2006; Tassara & Yáñez, 2003)

This includes the following earthquakes: Mw9.5 Valdivia 1960 (the largest event ever recorded), Mw8.8 Maule 2010, Mw8.4 Illapel 2015, Mw8.1 Iquique 2014, Mw8 Antofagasta 1995, Mw8 Valparaiso 1985, and Mw7.8 Tocopilla 2007 (see references for their slip models in caption of Figure 2.1).

Moderate-to-large slip associated to non-tsunamigenic events (1985, 1995, and 2007) ruptured mostly the deepest (inland) part of the seismogenic zone, defined as zone C of the megathrust by Lay et al. (2012). By the contrary, great-to-giant tsunamigenic events (1960, 2010, 2014, 2015) concentrate most of the slip below the offshore tip of the forearc, rupturing mostly zone B (and A) of Lay et al. (2012). Figure 2.1 also shows that most of the Southern Andean megathrust was ruptured by the 1960 and 2010 events, whereas large seismic gaps remain unbroken in the Central Andean segment, most notably associated with the great Iquique 1877, Copiapo 1922, and Valparaiso 1730 earthquakes. It is important to note that the estimated rupture lengths of the largest pre-instrumental earthquakes shown in Figure 2.1 (as proposed by Beck et al., 1998; Carvajal et al., 2017; Comte & Pardo, 1991) need to be carefully interpreted as uncertainties are difficult to assess for historical events (Philibosian & Meltzner, 2020).

2.3 Methods

We used three independent proxies of the frictional structure of the megathrust that are theoretically associated with this structure through different physical mechanisms: (a) residual gravity anomaly, (b) megathrust friction computed from Coulomb wedge theory, and (c) degree of geodetic plate locking. The first two are related to the long-term structure of both plates, which integrates millions of years of tectonic evolution, whereas the third proxy is computed by the inversion of satellite geodetic data (GPS surface velocities) that images crustal deformation at decadal time scale. We are particularly interested in analyzing the degree of spatial correlation between these three proxies and its relationship with recent earthquakes to propose a seismotectonic segmentation model of the Chile Margin. We first explain the method for the multivariate spatial correlation analysis of the three proxies and then we provide details about the computation of these proxies.

2.3.1. Principal Component Analysis

Principal Component Analysis (PCA) is a standard statistical method derived from linear algebra that is widely used to recognize patterns in data of high dimension and to highlight similarities and differences between these dimensions (e.g., Smith, 2002; Venegas, 2001). This method has been commonly used to study the spatial and temporal variability of geophysical data, for example to invert continuous GPS time-series into spatial patterns of slip after large earthquakes (He et al., 2015; Ji & Herring, 2013; Kositsky & Avouac, 2010; Perfettini et al., 2010). We use PCA to quantify common spatial patterns of the geophysical/geodetic proxies along the study region. Details about the development, implementation and application of our method are presented in the Supplementary Material (See Appendix A1), but we describe here some basic concepts that are necessary in order to frame the presentation and discussion of results.

PCA works over matrices that in our case are constructed by assembling M trench-perpendicular profiles as rows of a matrix P . The profiles are separated 20 km along the trench axis between 18° and 44°S , and each of them is formed by N points. When we applied the method to compute the residual gravity anomaly (see Section 2.3.2.1), then we choose $N = 400$ points that were spaced by 2.5 km and covered 500 km to both sides of the trench axis. By performing the PCA method to analyze the spatial correlation between the different frictional proxies, we choose $N = 166$ points separated by 0.9 km that cover a length of approx. 150 km from the trench axis to the main Andean cordillera.

Matrix P is used to interpolate grids with values of the frictional proxies (the computation of which is explained in Section 2.3.2) in order to build one data matrix D_p for each proxy p . Values on D_p are centered and normalized with respect to the mean and standard deviation of each proxy in order to ensure spatial comparability between them (e.g., Smith, 2002; Venegas, 2001). Our implementation of PCA can be applied to one individual matrix D_p (in which case we define a parameter $C = 1$) or combinations of them ($C = 2$ or 3). In this later case, we concatenate the D_p matrices in a combined data matrix D . From the covariance matrix of D , it is straightforward to obtain its eigenvalues λ_k and eigenvectors E^k . The eigenvectors, also called Empirical Orthogonal Functions (EOFs), represent in our case the

along-trench variability of a particular trench-perpendicular characteristic spatial pattern. We refer to the K indexes as modes, which are ordered following the rank of their eigenvalues λ_K from the highest ($K = 1$) to the lowest ($K = CN$). Only the first K modes are further considered as their EOFs concentrate most of the common variability of the original data (measured as the sum of the first K eigenvalues divided by the sum of all the eigenvalues). For each proxy, we stack the first K EOFs in a matrix E_p . We then compute the principal component matrix for each proxy as $A_p = E_p^T * D_p$ (T indicating the transpose of E_p), which has dimensions $K \times N$ and therefore is independent of the number of trench-perpendicular profiles M . Each row of the A_p matrix is known as the Principal Component (PC) associated with a particular mode K and provides valuable information on the trench-perpendicular variability of the along-trench pattern informed by its respective EOF. Multiplying E_p (containing the K EOF columns of length M) with A_p (containing the K PC rows of length N) and remapping the (m,n) matrix locations back to the original geographic coordinates, it is possible to map the first-order common spatial distribution of each proxy as informed by the first K modes considered in the analysis. Details of the full procedure are described in the Supporting Information.

2.3.2 Computation of Proxies for Megathrust Frictional Structure

2.3.2.1. Residual Gravity Anomaly Δg

Residual gravity anomalies at subduction zones have been commonly computed from Free-Air and/or Bouguer anomaly grids by subtracting trench-perpendicular average values to the data. This procedure allows removing the long wavelength part of the gravity signal associated with the underlying dense oceanic plate and the geometry of the forearc wedge. The remaining residual signal highlights short-wavelength features most likely related to lateral variations of the density structure of the forearc and frictional heterogeneities of the megathrust. The computation of the trench-perpendicular average gravity field has been done both in the spatial (Song & Simons, 2003) and frequency (Bassett & Watts, 2015a, 2015b) domains. However, if only a single trench-perpendicular averaged regional profile is considered for a very long subduction zone such as the Chile Margin (ca. 4,500 km

length), residual anomalies may be systematically over- or under-estimated as long-wavelength along-trench tendencies will be masked. To overcome this potential bias, we developed a new procedure that is based on the PCA method. Instead of removing a single 1D trench-perpendicular average profile to the original gravity data as done by previous authors, we computed the residual gravity anomaly by removing the 2D gravity field reconstructed from the first mode identified by the PCA analysis over the original gravity data, which contain the first-order trench-perpendicular and along-trench features of the gravity field.

We applied the method described in Section 2.3.1 to the Free-Air gravity anomaly grid of Sandwell et al. (2014), as shown in Figure 2.2a. In order to apply the procedure, we created the matrix \mathbf{P} considering in this case $M = 341$ trench-perpendicular profiles, each containing $N = 400$ points separated by 2.5 km and covering 1000 km from a point in the Nazca plate in the west to another point located at the eastern part of the cordilleran axis (see Figure 2.2). The trench in all the profiles is located at the center of the profile (i.e., $n = 200$). After interpolating the original value of Free-Air anomaly for each (m, n) element of matrix \mathbf{P} , we obtained the covariance matrix and then the eigenvalues (measuring the amount of variance), eigenvectors (EOFs for the along-trench spatial tendency) and principal components (representing the trench-perpendicular spatial tendency) for each mode K . We then reconstructed the full spatial tendency expressed in the first mode by multiplying the EOF and principal component associated only with $K = 1$. The obtained first-order tendency of the Free-Air anomaly is shown in Figure 2.2b, where we can appreciate the large signal associated with main tectonic features of the subduction zone and their long-wavelength along-trench variation. After linearly gridding and subtracting the result from the original data, we obtain the residual gravity anomaly Δg (Figure 2.2c).

2.3.2.2. Effective Basal Friction Coefficient Φ_b

The classical Non-Cohesive Coulomb Wedge (NCCW) theory (Dahlen, 1984; Davis et al., 1983) applied to a subduction zone relates the taper angle of the forearc wedge (i.e., the sum of topographic slope angle α and slab dip angle β) with the force balance between the frictional strength of the megathrust and gravitational

body forces inside the wedge itself. According to the NCCW theory, the spatial variations of the taper angle $\alpha + \beta$ should reflect changes either of the wedge's physical properties (i.e., internal friction coefficient μ_{int} , pore fluid pressure ratio λ and density ρ) or the effective basal friction coefficient Φ_b (to clarify, by Φ_b we are not referring to the basal friction angle, but it refers to μ_b^{eff} of Cubas et al., 2013 or μ_b'' of Wang & Hu, 2006). The taper angle should be considered in this framework as the resulting manifestation of the deformation suffered by the wedge at geological timescale in order to balance the internal body forces of the wedge and frictional shear traction at its base.

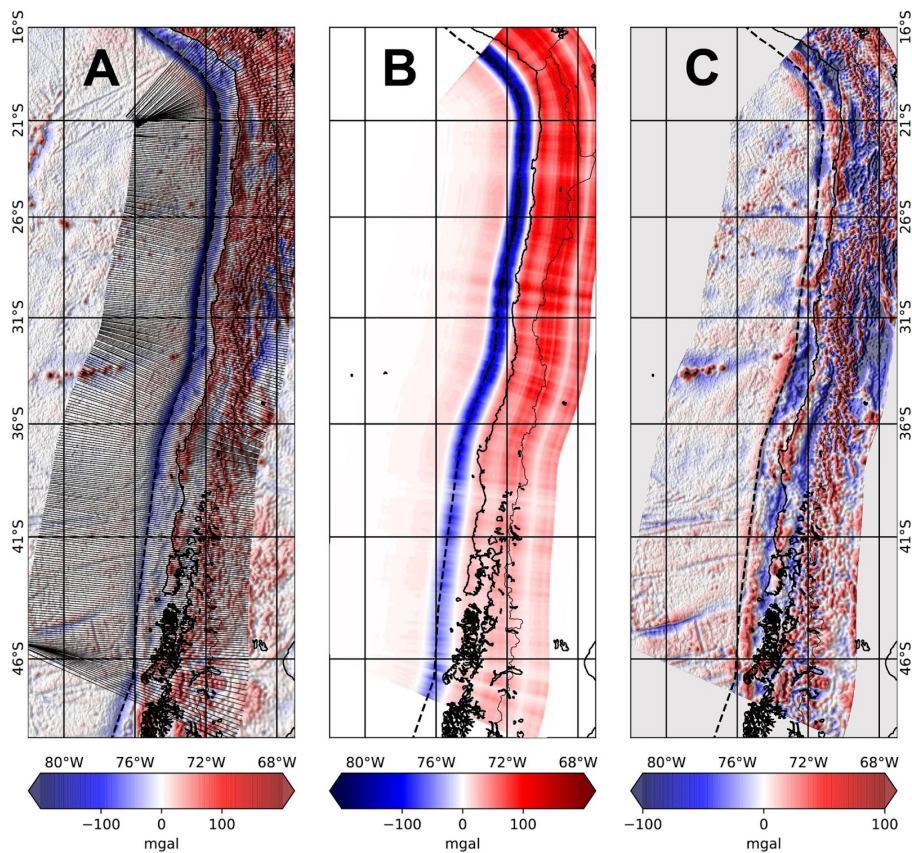


Figure 2.2: Derivation of Residual Gravity Anomaly by the Principal Component Analysis (PCA) method. (a) Original Free-Air anomaly of Sandwell et al. (2014) after centering and normalizing the grid values. Black lines show the $M = 341$ trench-perpendicular profiles that form matrix P in this case. (b) Full spatial tendency of the gravity field as defined by the first mode identified by the PCA analysis. (c) Final residual gravity anomaly Δg obtained after subtracting the spatial tendency related to the first mode (b) from the original data (a).

As mentioned by several authors (Cubas et al., 2013; Dahlen, 1984; Maksymowicz, 2015; Wang & Hu, 2006) the NCCW is unable to describe the continuous time variation of the stress–strain field or to make predictions about a specific fault. However, it describes the deformation style of the continental wedge that results from the maintenance and support of the first-order wedge geometry at the time scale of million years.

We calculate taper angles estimating β directly from the Slab2.0 model (Hayes et al., 2018) between the trench and the 50 km depth contour of the subducted slab, which should encompass the entire seismogenic zone (Lay et al., 2012). The value of α is derived from the GEBCO_2020 bathymetry-topography grid (https://www.gebco.net/data_and_products/gridded_bathymetry_data/). The raw grid was smoothed in order to capture the first-order wedge geometry, avoiding potential bias due to small scale topographic features such as submarine canyons. To do so, each grid cell was assigned the average slope within a 25-km-radius smoothing window centered in the cell itself. As shown by Cubas et al. (2013), the size and shape of the smoothing window do not substantially impact inferences of α . Once α and β are determined, we define a local wedge taper angle at each grid node and compute the corresponding estimate of Φ_b from Equations 9, 17, and 19 of Dahlen (1984). For this, we assume constant values of physical properties inside the wedge, that is, $\mu_{int} = 0.6$, $\lambda = 0.85$ and $\rho = 2,700 \text{ gr/m}^3$. Although these numbers are similar to those used by previous authors (Cubas et al., 2013; Dahlen, 1984; Maksymowicz, 2015; Wang & Hu, 2006), their actual values are irrelevant for the purpose of this study, because our aim is to detect relative variation of effective basal friction along strike, rather than its absolute value. Accordingly, estimates of Φ_b are divided by the average of the entire margin, such that values greater/lesser than 1 indicate basal friction above/below this average. We also note that Φ_b is almost insensitive to lateral variations of density within the range of possible values for crustal materials, as demonstrated for instance by the detailed sensitivity analysis of Maksymowicz (2015). This is important because it ensures that this proxy for the frictional structure of the megathrust is independent of residual gravity anomalies Δg , which are mostly dominated by the density distribution of both plates.

2.3.2.3. Degree of Interseismic Geodetic Locking Λ

The degree of interseismic locking Λ that can be derived from space geodetic data is one of the most popular methods to illuminate the apparent distribution of coupled asperities along the megathrust. The values of Λ ranges between 0 for no fault locking (i.e., fully creeping behavior likely related to low-friction barriers where no elastic strain is being cumulated) to 1 for a fully locked/coupled fault (i.e., likely related to high-friction seismic asperities). Here we use a map of Λ created by a concatenation at the scale of the whole Chilean margin of maps for specific regions presented by Moreno et al. (2010, 2012), Tilmann et al. (2016), and Li et al. (2015). All these maps were based on the same methodology, that is, the inversion of interseismic GPS velocity vectors to backslip (Savage, 1983) at the megathrust via Green's functions that are computed on the base of a unique 3D finite element elastic model. Therefore, these individual maps are fully compatible and can be integrated into a coherent image of interseismic locking along the entire margin. Further details on the methodology may be found in Moreno et al. (2012) and tests for the spatial resolution of each map are provided in the original publications. The first order along-trench pattern of interseismic locking identified by the PCA method using our concatenated grid is rather similar to the tendency recognized from grids published by Metois et al. (2016) and Saillard et al. (2017), as can be seen in Figures S1 and S2 (See Appendix A1).

2.4. Results

The results of the methods described in Section 2.3.2 are shown in Figure 2.3, including maps of the degree of interseismic geodetic locking (Λ), forearc residual gravity anomaly (Δg), and long-term effective basal friction coefficient (Φ_b). We will focus here on the analysis of common spatial features of the three proxies to obtain an integrated view of the frictional structure of the megathrust. Independently, these three proxies exhibit a first-order positive visual correlation between regions with high values of Λ , Δg , and Φ_b , such as along the Central Andean forearc (i.e., north of 33°S). However, farther south the relation is less obvious along specific forearc segments of the Southern Andes.

Figure 2.4 shows the trench-perpendicular Principal Components (PCs, Figure 2.4a) and along-trench Empirical Orthogonal Functions (EOFs, Figure 4b) for each proxy resulting from the multivariate PCA analysis combining the three of them ($C = 3$). As can be observed in Figure 2.4a, the PC of the first mode is very similar for the three proxies. This common first-order trench-perpendicular tendency shows a downward concave shape with positive values between 20 and 140 km from the trench and negative values beyond this range. The similarity of the first PC between the three proxies is expressed in the percentage of total variance explained by the first mode, which in this case is 41.4%.

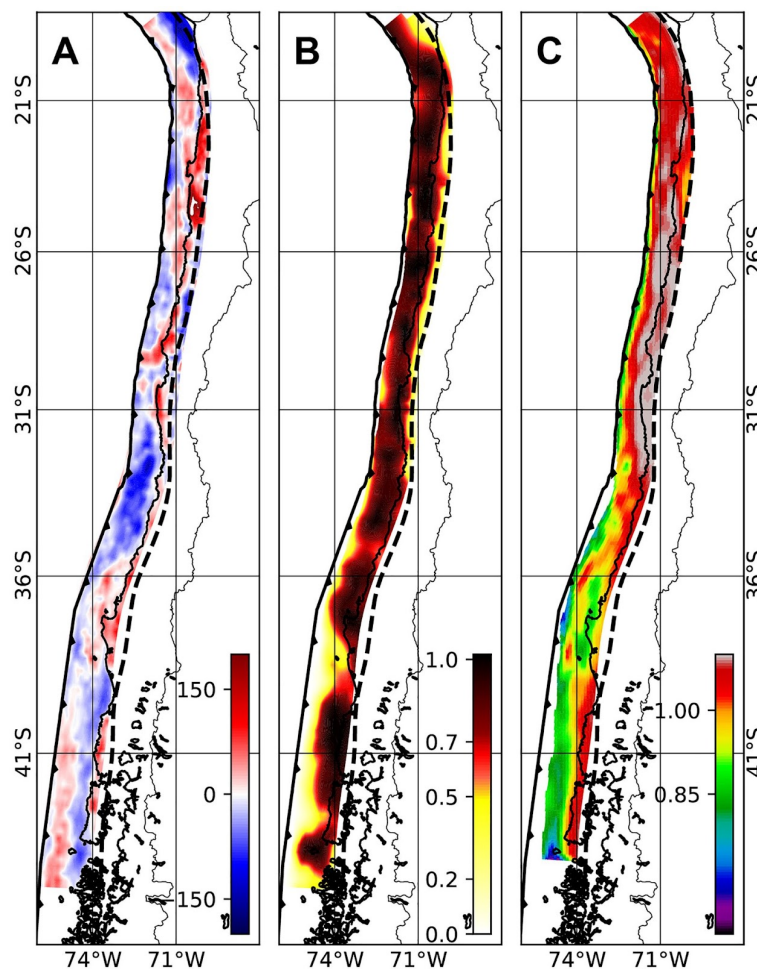


Figure 2.3: Spatial distribution of the three proxies of the frictional structure along the Chilean megathrust inside the area considered for this study (i.e., as covered by the 150 km long trench-perpendicular profiles used for the principal component analysis). (a) Residual Gravity Anomaly Δg [mGal], (b) Interseismic Geodetic Locking Λ , (c) Long-term Basal Friction Φ_b . Dashed-black line shows the 50 km contour of the subducted slab (Hayes et al., 2018).

No formal rule has been proposed for evaluating the explained variance in terms of a possible correlation between different variables, but this number can be considered significant when compared to other analyses of geophysical fields (e.g., Davydenko & Grayver, 2014; Rangelova et al., 2007; Wilks, 2016). Figure 2.4a also shows the trench-perpendicular tendency associated with PCs obtained by considering the first two modes ($k = 1 + 2$), which account for 69.4% of the total variance. The differences between these tendencies and those related to the first mode alone illuminate the trench-perpendicular trend of the second principal component (for $K = 1$), which account for 28% of the total variance. As can be inferred from Figure 2.4a, trends associated with the second mode are also similar between the three proxies and differ with respect to PCs of the first mode by showing a shift from

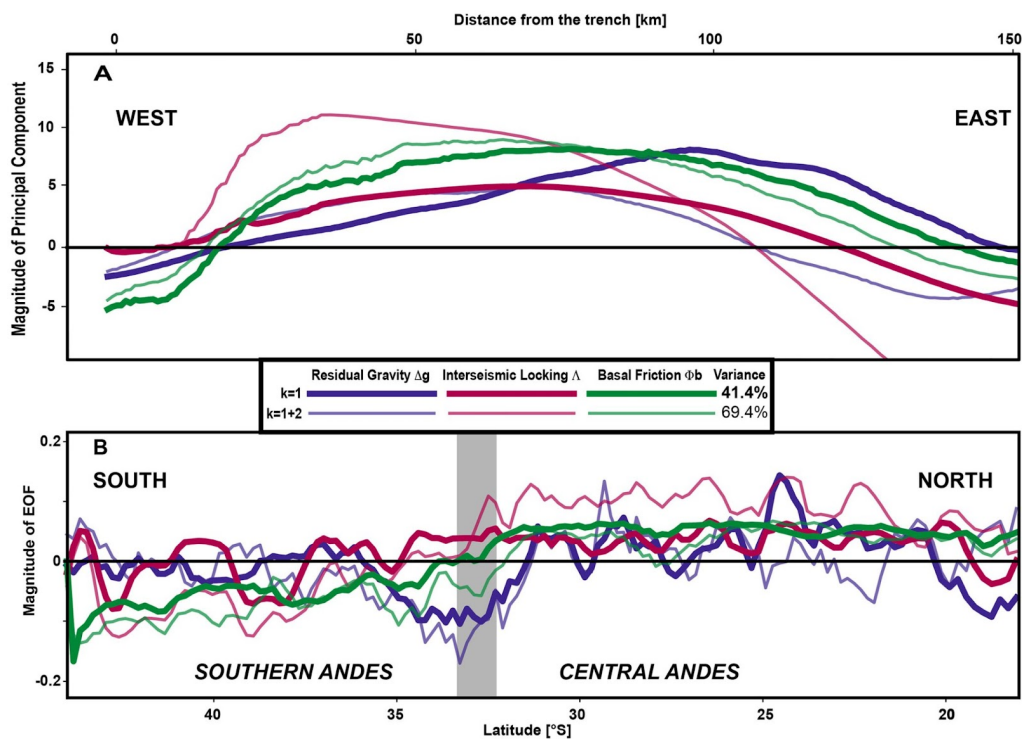


Figure 2.4: Results of the combined multiproxy Principal Component Analysis analysis. (a) Magnitude of the Principal Components (PCs) for each computed proxy depicting the trench-perpendicular tendency of the data against the distance from the trench ($x = 0$ km). (b) Magnitude of the Empirical Orthogonal Functions (EOFs, i.e., the eigenvectors of the covariance matrix, see Section 3.1) for each proxy at latitudes projected along the trench axis. For both panels, the color of each line represents different proxies (blue for gravity anomaly Δg , red for interseismic locking Δ , green for basal friction coefficient Φ_b) and their thickness differentiates results for the first mode only ($K = 1$, thick line) and for a combination of the first two modes ($K = 1 + 2$, thin line).

positive values in the trench-ward half of the profile toward negative values landward. The small difference between PCs obtained for $K = 1$ and $K = 1 + 2$ in the case of long-term basal friction Φ_b indicates that the magnitude of the second PC is rather low compared with the first PC. This is also the case for the trench-ward part of residual gravity Δg . Larger amplitudes for $K = 2$ are most notable in the case of interseismic locking Λ , for which the entire second PC profile has amplitudes similar to the first PC, implying that the combined $K = 1 + 2$ tendency differs significantly with respect to the PC of the first mode. The along-trench variability of the PCs can be appreciated in the form of the Empirical Orthogonal Functions (EOFs) depicted in Figure 2.4b. The EOFs associated with the first mode ($k = 1$) define the first order along-trench tendency of the three proxies, which is dominated by positive values along the Central Andean forearc and neutral-to-negative values along the Southern Andes. Within this first-order tendency, the larger along-trench variability is shown by Δg that is marked by successive highs and lows, intersecting the origin of the y-axis (i.e., magnitude of EOF = 0) at several latitudes. This is different to the tendency shown by basal friction along the Central Andes where it presents a roughly constant value of EOF magnitude with rather smooth and small-amplitude fluctuations, whereas locking shows an intermediate behavior between the other two proxies. Transitioning toward the Southern Andean forearc, the EOFs of friction and locking start to differ with Φ_b moving toward negative values and showing a gradual southward decrease, whereas Λ also shows a general southward decrease but maintaining the EOF in average values around zero and a tendency that is more similar to the one shown by gravity. Along-trench tendencies shown for the first two modes together ($K = 1 + 2$) are similar to those described for the first mode alone, mostly for friction and gravity with locking showing increased amplitudes and larger latitudinal gradients.

A complementary view of the results obtained by our PCA method is presented in Figure 2.5, where we show 12 maps for each proxy (36 maps in total) that are reconstructed after performing the matrix multiplication between column EOF vectors (i.e., along-trench tendencies) with row PC vectors (i.e., trench-perpendicular tendencies) for specific combinations of proxies and modes. Particularly, maps along the right-hand panels of Figure 2.5 were reconstructed multiplying the PCs and

EOFs of Figure 2.4, that is, considering the triple combination of the proxies ($C = 3$) and for the three possible combinations of modes ($K = 1, K = 2, K = 1 + 2$). For comparison and completeness, this figure also shows results for the three proxies in isolation ($C = 1$) and the three possible double combinations ($C = 2$). We first note that the intensity of each map (i.e., the range of mapped values around zero) increases with the percentages of explained variance.

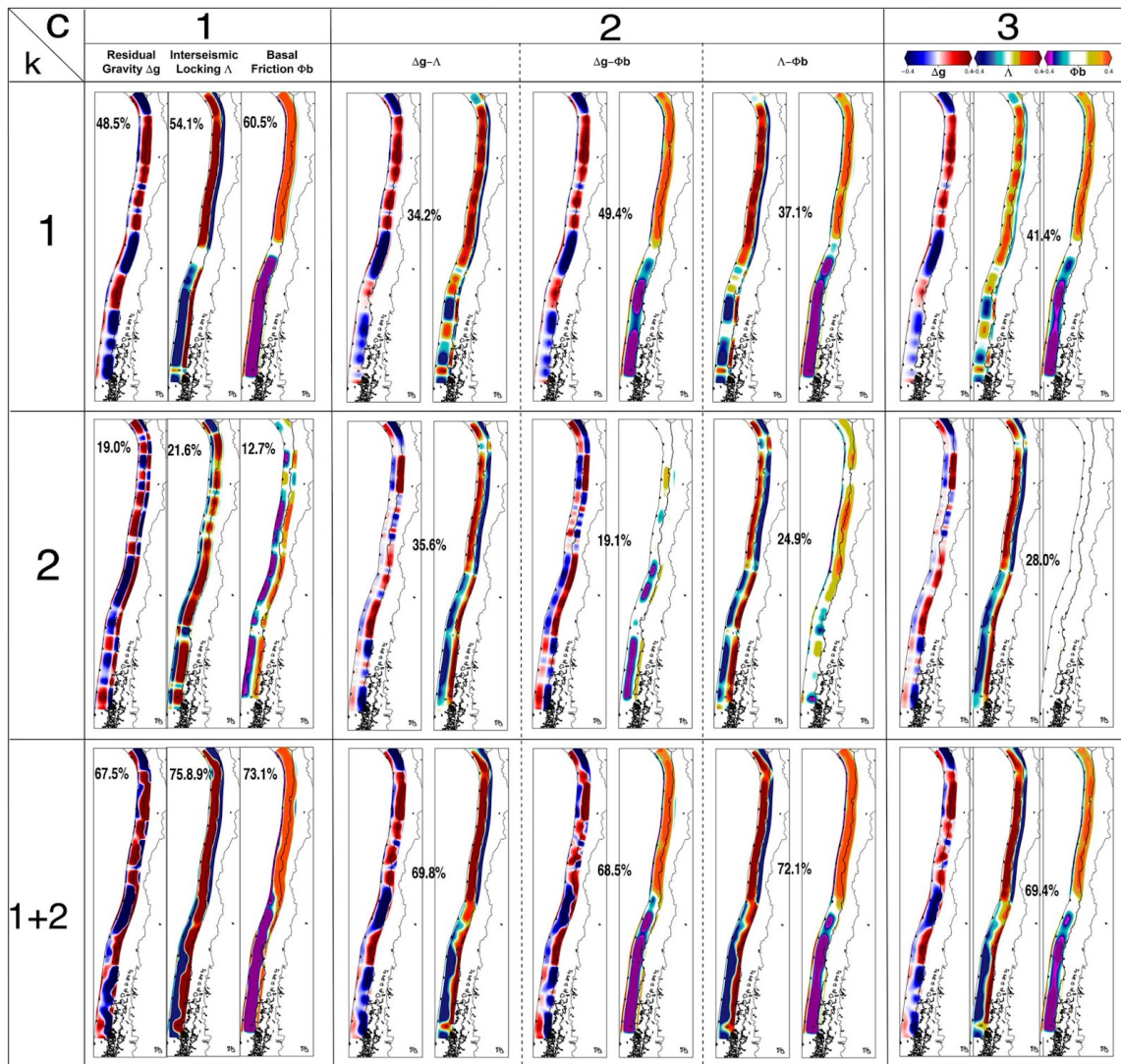


Figure 2.5: Reconstructed maps of the three frictional proxies (Residual Gravity Anomaly Δg , Degree of Interseismic Locking Λ , and Long-Term Basal Friction Φ_b) obtained for different combinations of them in the Principal Component Analysis analysis (x-axis: $C = 1$ isolated analysis, $C = 2$ dual combinations, $C = 3$ triple combination) and different modes (y-axis: $K = 1$ first mode, $K = 2$ second mode, $K = 1 + 2$ both modes combined). Percentages indicate the amount of variance explained in each case.

We also note that the pattern of reconstructed spatial features is more complex and closer to the original proxies (compared with Figure 2.3) when we consider both modes together than when only the first mode is considered. The percentage of variance explained with $C = 1$ (isolated proxy) is only $\sim 10\%$ higher than the value for $C = 3$ (triple combination) and the spatial tendencies observed in maps for $C = 1$ and $C = 3$ are also very similar. This is an indication that these proxies are spatially correlated and share a first order along-trench tendency that must be connected through a common physical process. In the case of Φ_b , it can be clearly appreciated that the second mode contains a small fraction of information, with values near zero for $K = 2$ in double ($C = 2$) combinations and most notably for the triple combination ($C = 3$). This is also visible in the variance explained by the first and second modes of the isolated analysis ($C = 1$) that for Φ_b are respectively the largest (60.5%) and lowest (12.7%) of the three proxies. Spatial tendencies observed for the second mode of Δg and Λ are rather stable independent of the number of combined proxies. In the case of gravity, it shows a dual trench-perpendicular trend that has an along-trench variation complementary to the tendency of the first mode, whereas mode two of locking (mostly for dual and triple combinations) reinforce the near trench tendency of $k = 1$ to show positive values along the Central Andes and negative values for the Southern Andes.

2.5. Discussion

2.5.1. Relating Trench-Perpendicular PCA Tendencies With Megathrust Seismogenic Zone

One of our main results is that the principal components (PCs) characterizing the first order trench-perpendicular tendency of each frictional proxy are very similar one to the other (Figure 2.4a). This common tendency should be associated to a primary physical mechanism connecting the proxies between them and with the seismogenic behavior of the megathrust.

In order to investigate this possible mechanism, Figure 2.6 presents a comparison between the PCs obtained with $k = 1$ and $C = 3$ for the three frictional proxies (as in Figure 2.4a) and histograms showing the trench-perpendicular distribution of

seismicity and coseismic slip. To compute the seismicity histogram, we calculated the trench-perpendicular distance to the trench axis of all the epicenters reported between 1950 and 2020 by the USGS-NEIC catalog (<https://earthquake.usgs.gov/earthquakes/search/>). A similar procedure was applied to obtain trench-perpendicular histograms of maximum coseismic slip from published models (as cited in the caption of Figure 2.6). We considered here the normalized distribution of maximum slip for each event in order to better compare their trench-perpendicular tendencies.

Figure 2.6 shows a zone characterized by positive magnitudes of PCs coinciding with the region where most of the epicenters are located and the largest proportion of coseismic slip is released. The absolute magnitude of the PCs inside this zone tends to correlate with the number of earthquakes and amount of slip, showing a common parabolic form and maximum values for all of them roughly at the center of the zone of positive PCs. Based on this spatial correlation, we identify the two regions where the magnitude of at least one of the three PCs is zero as the updip and downdip limits of the seismogenic zone. These regions are located in Figure 2.6 at respective distances from the trench axis of 20 ± 5 and 135 ± 10 km.

Given the somehow ambiguous meaning of the “seismogenic zone” concept (e.g., Wang & Tréhu, 2016) and taking into account that we aim to establish a mechanical link between the frictional proxies and megathrust seismic behavior, we consider here a definition of the seismogenic zone based on the rate-and-state friction (RSF) law (Dieterich, 1981; Marone, 1998; Ruina, 1983; Scholz, 1998), which in the steady-state can be written as:

$$\tau = \left[\mu_0 + (a - b) \ln\left(\frac{V}{V_0}\right) \right] (\sigma_n - p) \quad (1)$$

In this expression τ is shear stress, σ_n is normal stress, p is pore fluid pressure, and the rate-dependent friction is defined by the term into square brackets; μ_0 is a reference friction attained when the slip velocity V equals the long-term convergence velocity V_0 , and the parameters a and b are experimentally determined. Most fault

materials show negative values of $(a - b)$ for a temperature range between 100°C and 450°C (e.g., Blanpied et al., 1991; Scholz, 1998; den Hartog et al., 2012). Under this condition, Equation 1 predicts a decrease of friction after a sudden increase in slip velocity, that is, a velocity-weakening (VW) behavior where earthquakes can nucleate as frictional instabilities and coseismic slip spread. Owing to the gradual downdip increase of megathrust temperature (e.g., Hyndman & Wang, 1993; Oleskevich et al., 1999), the VW behavior is restricted to a particular depth range that is properly defined into this conceptual framework as the seismogenic zone (Wang & Tréhu, 2016). Inside the VW seismogenic zone, the actual frictional stability regime depends on the relationship between the effective normal stress on the fault ($\sigma_n - p$ in Equation 1) and a critical stress σ_c defined by Scholz (1998) as:

$$\sigma_c = \frac{kL}{-(a-b)} \quad (2)$$

Here k is the stiffness of the elastic media surrounding the fault and L is a critical slip distance. When $\sigma_n > \sigma_c + p$ the fault can only move by unstable sliding during earthquakes, while for $\sigma_n < \sigma_c + p$ the fault is in a conditionally stable regime. Dynamic numerical models of fault behavior based on the RSF law (e.g., Barbot et al., 2012; Noda & Lapusta, 2013) have demonstrated the very rich nature of conditionally stable regions, which show a range of frictional behaviors varying between slow creeping to fault locking during the interseismic phase, unstable coseismic sliding or rupture arrest. In this context, conditionally stable fault patches inside the seismogenic zone can act either as asperities or as barriers depending on their preseismic state of stress and previous patterns of dynamic rupture propagation (Avouac, 2015; Barbot et al., 2012; Bürgmann, 2018; Noda & Lapusta, 2013).

The seismogenic zone mainly corresponds with domain B of Lay et al. (2012), that is, the central down-dip segment of the interplate contact that is characterized by the strongest unstable-sliding VW frictional behavior (Figure 2.6). Owing to this condition, fault domain B slips mainly during great earthquakes (Lay et al., 2012). In the Chilean case (Figure 2.6), this behavior is partially exemplified by the 1995 Antofagasta earthquake (Carlo et al., 1999; Delouis et al., 1998) and mostly by the

2014 Iquique earthquake that ruptured almost exclusively within zone B (e.g., Ruiz et al., 2014; Schurr et al., 2014). The seismogenic zone of Figure 2.6 also includes most of the deeper domain C, characterized by moderate coseismic slip and large radiation of high-frequency energy as observed during the 1985 Valparaiso and 2007 Tocopilla earthquakes (Bravo et al., 2019; Motagh et al., 2010; Peyrat et al., 2010). This behavior can be attributed to the very heterogeneous frictional structure of the fault zone around the downdip limit of the seismogenic zone owing to temperatures between 450°C to 650°C that control transitions of frictional stability regimes and rheology, to the great amount of fluids released from the slab at that depth range, and to the intersection of the megathrust with the continental Moho (Bilek & Lay, 2018; Bürgmann, 2018; Lay et al., 2012; Oleskevich et al., 1999; Wang & Tréhu, 2016). A transitional nature of the downdip limit along domain C can be related in Figure 2.6 with the broader region where the magnitudes of PCs are near zero in comparison with the narrower region associated to the updip limit in the outer forearc region.

Regions located updip and downdip of the seismogenic zone have respectively lower and higher temperatures and therefore are characterized by $(a-b) > 0$. As predicted by Equation 1, this implies a velocity-strengthening (VS) frictional behavior, that is, an increase of friction after an increase in slip velocity. The updip region covered by domain A mostly slips by slow stable sliding associated with aseismic creep during the inter- or post-seismic phases of the seismic cycle, potentially acting as updip barriers to coseismic rupture propagation (Bilek et al., 2004; Bürgmann, 2018; Oleskevich et al., 1999; Scholz, 1998; Wang & Tréhu, 2016). However, the megathrust can be affected by rapid dynamic rupture coming from domain B that can trigger shallow slip eventually up to the trench, causing large tsunamis. This has been the case in Chile for some asperities ruptured by the 1960 Valdivia and 2010 Maule earthquakes and for the 2015 Illapel asperity, all of them generating large tsunamis related to significant slip up to the trench (e.g., Moreno et al., 2009; Tilmann et al., 2016; Yue et al., 2014). The two greatest earthquakes (1960 and 2010) ruptured the full megathrust, slipping along domains A, B, and C. Most of the coseismic slip and epicenters do occur inside the region identified with the seismogenic zone in Figure 2.6, but a significant number of earthquakes and amount of slip is located outside this zone. This is consistent with the general

characterization of the seismogenic zone done by Wang and Tréhu (2016) that show how the downward extend of the VW zone is commonly narrower than the extend of seismicity and earthquake rupture area, mostly at the downdip limit. In this framework, we interpret the observed correlation (Figure 2.6) between magnitude of PCs for the frictional proxies, number of earthquakes and amount of coseismic slip as indicating that all of them could be directly related to the intensity of the VW frictional effect.

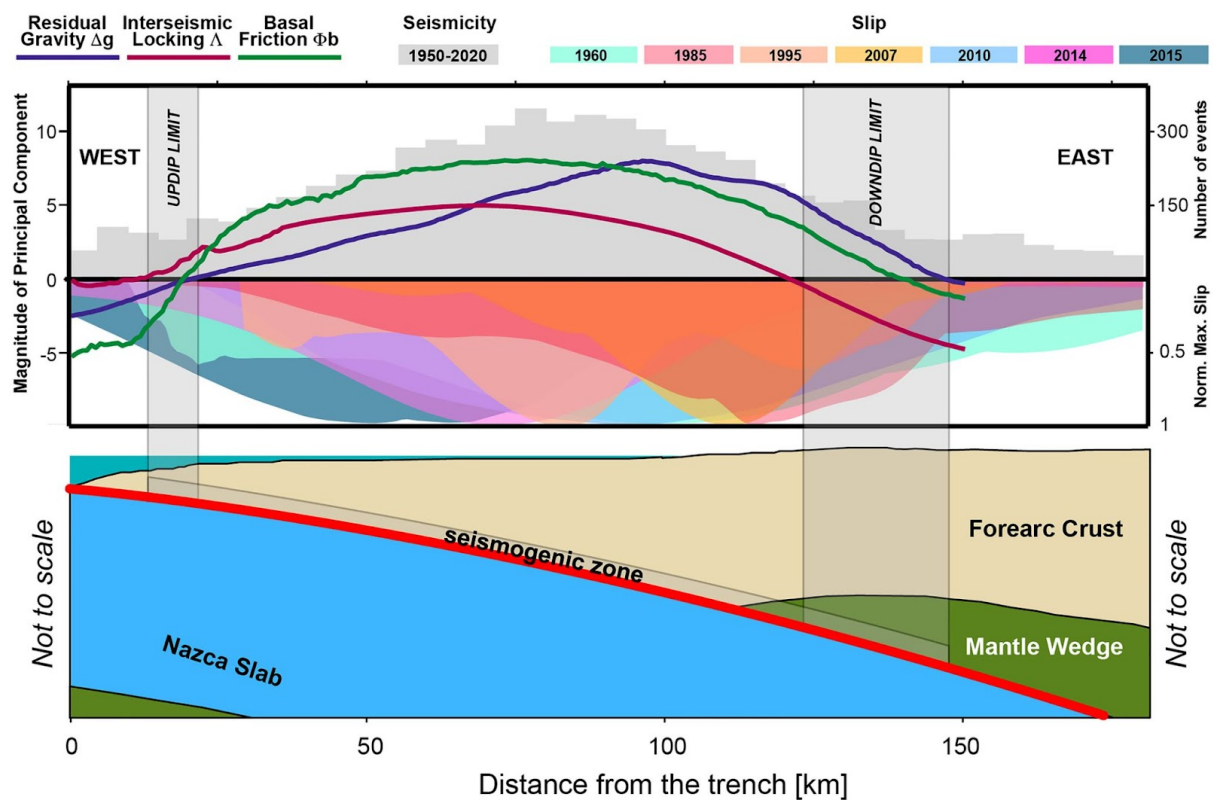


Figure 2.6: Relationship between trench-perpendicular tendencies of frictional proxies, seismic behavior and schematic subduction zone structure. Upper panel shows Principal Components (PCs) of each proxy for the first mode ($K = 1$, as in Figure 2.4) along with number of seismic events reported between 1950 and 2020 in the catalog of the National Earthquake Information Center (NEIC, USGS USA) and normalized maximum slip of large megathrust earthquakes (Iquique 2014 from Schurr et al., 2014; Antofagasta 1995 from Hayes, 2017; Tocopilla 2007 from Motagh et al., 2010; Illapel 2015 from Tilmann et al., 2016; Valparaiso 1985 from Bravo et al., 2019; Maule 2010 from Moreno et al., 2012; Valdivia 1960 from Moreno et al., 2009). Lower panel is a schematic representation (not to scale) of the structure of the subduction zone marking the seismogenic zone along the megathrust (red line). The updip and downdip limits of the seismogenic zone are identified as regions where the magnitude of PC = 0, which coincides with a respective updip and downdip decrease in the number of earthquakes and coseismic slip.

Remember that the actual value of each particular proxy at a given position along the study area will result from the multiplication between the magnitude of its PC and the value of its respective EOF. In this sense, the magnitude of PCs can be considered as defining the amplitude of a given reconstructed proxy whereas the EOF magnitude will define its particular sign (either positive or negative). Thus, we recall that peak values for the magnitude of PCs at the center of the seismogenic zone just indicate that the amplitude of each proxy will be maximized here, which therefore can be interpreted as to that the intensity of the VW effect will be also maximized.

In this context, long-term basal friction Φ_b could be associated to the intensity of the VW behavior via a direct relation to μ_0 of Equation 1, with our results indicating that this parameter has a first-order trench-perpendicular tendency marked by a maximum amplitude at the center of the seismogenic zone and tapering toward its updip and downdip limits. In the case of the residual gravity anomaly Δg this connection could be also established throughout a link with friction, if we follow the interpretation of Song and Simons (2003) and others (e.g., Fuller et al., 2006; Llenos & McGuire, 2007; Wells et al., 2003). However, this interpretation suggests that high megathrust friction must be related to low gravity, contradicting our main observation. We support the alternative view (Bassett & Watts, 2015a, 2015b; Li & Liu, 2017; Tassara, 2010) under which forearc gravity is mainly controlled by the density structure of the subduction zone. Particularly, we believe that the main trench-perpendicular tendency of the gravity anomaly in Figures 2.4a and 2.6 could be caused by a combination of a large-scale signal associated with the density structure mostly of the upper plate (as discussed in Section 2.5.3) over which a smaller-scale signal related to the Trench Parallel Forearc Ridge (TPFR) of Bassett and Watts (2015b) is superimposed. The TPFR has been recognized globally and along the Chile Margin as a positive anomaly along the coastal region presumably related to the underplating of tectonically eroded material near the downdip limit of the seismogenic zone. The superimposed signal of the TPFR could also explain the apparent eastward shift of the peak in gravity compared with those of friction and locking in Figure 2.6.

The density structure and associated buoyancy forces affect Equation 1 mostly through the normal stress σ_n . For the VW effect being positive and maximized inside the seismogenic zone, Equation 2 indicates that σ_n must be high enough to overcome the sum of pore pressure and critical stress threshold. This condition can be accomplished only if density is high, which translates in a high value of Δg . Complementary to the long-term view contributed by Φ_b and Δg , the short-term degree of interseismic locking Λ has been directly related to the magnitude of shear stress at the megathrust (e.g., Wang & Dixon, 2004). If we relate τ with Λ in Equation 1, this latter could be interpreted as a consequence of the interaction between friction (expressed by Φ_b) and effective normal stress (approximated by Δg). With both showing maximum amplitudes at the center of the seismogenic zone, it is expected that Λ will also show a similar first order trench-perpendicular tendency.

We conclude that the sign and magnitude of principal components associated with the first mode of the combined PCA are strongly related to the trench-perpendicular limits of the seismogenic zone and the intensity (or amplitude) of the VW effect within it.

2.5.2. Along-Trench PCA Tendencies and Segmentation of the Chilean Megathrust

We analyze here how the along-trench tendencies of the frictional proxies are spatially correlated with the latitudinal distribution of epicenters and coseismic slip. Remember that the principal component of each proxy is one of the two orthogonal (independent) vectors that describe its actual spatial distribution. The second vector is the Empirical Orthogonal Function (EOF), which should be interpreted as describing the along-trench variability of the trench-perpendicular PC. As we believe that the first mode PCs are directly related to the amplitude of the VW effect within the seismogenic zone, the information provided by the EOFs should be fundamental in order to identify patterns of seismic segmentation along the margin and to link them with the physical mechanisms controlling the megathrust frictional structure. In order to explore this possibility, Figure 2.7 compares the magnitude of EOFs obtained for $K = 1$ and $C = 3$ (as in Figure 2.4b) with the along-trench distribution of seismicity and coseismic slip (as in Figure 2.6).

2.5.2.1. Large-Scale (10^3 km) Segmentation and the Role of Contrasting Frictional Stability Regimes

We note that the Central Andean forearc is characterized by a relatively constant magnitude of the three EOFs around 0.05, with the residual gravity anomaly showing the strongest latitudinal variability. A common southward decrease of the three EOFs can be appreciated along the Southern Andean segment: the EOF magnitude for basal friction (hereafter denoted as EOF Φ_b) becomes increasingly negative southward of 33°S, EOF Δg shows negative-to-neutral values maintaining the strong latitudinal variability observed along the Central Andes and EOF Λ largely follows the main tendency shown by gravity south of 35°S. This large scale (10^3 km) segmentation is spatially correlated with a concentration of pre-2010 epicenters northward from 34°S and much larger coseismic slip released by great earthquakes to the south. Of course, these first-order seismic tendencies could be transient, since great earthquakes ($M_w > 8.5$) have not been yet instrumentally recorded in the Central Andes but have certainly occurred in the past.

If we focus in the central part of the seismogenic zone where the magnitudes of PCs are the highest (Figure 2.6) and follow the conceptual framework established in the previous section, we may infer that the Central Andean seismogenic zone is dominated by high friction Figure 2.8. (associated to positive EOF Φ_b) and high normal stress (owing to mostly positive and locally large EOF Δg), both contributing to maintain the megathrust shear stress at high levels that are translated into the observed high EOF Λ . Moreover, the combination of large normal stresses implied by positive gravity anomalies and the low pore pressure expected inside the narrow Central Andean subduction channel due to the lack of subducted trench sediments (e.g., Dielfolder et al., 2020; Lamb & Davis, 2003; Seno, 2009), should maximize the positive VW effect inside the seismogenic zone, forcing the megathrust to largely stay under unstable frictional conditions.

The notable southward change in the sign of EOF Φ_b crossing the boundary between Central and Southern Andes suggests a reduction of megathrust friction, which combined with a reduced normal stress as implied by negative-to-neutral

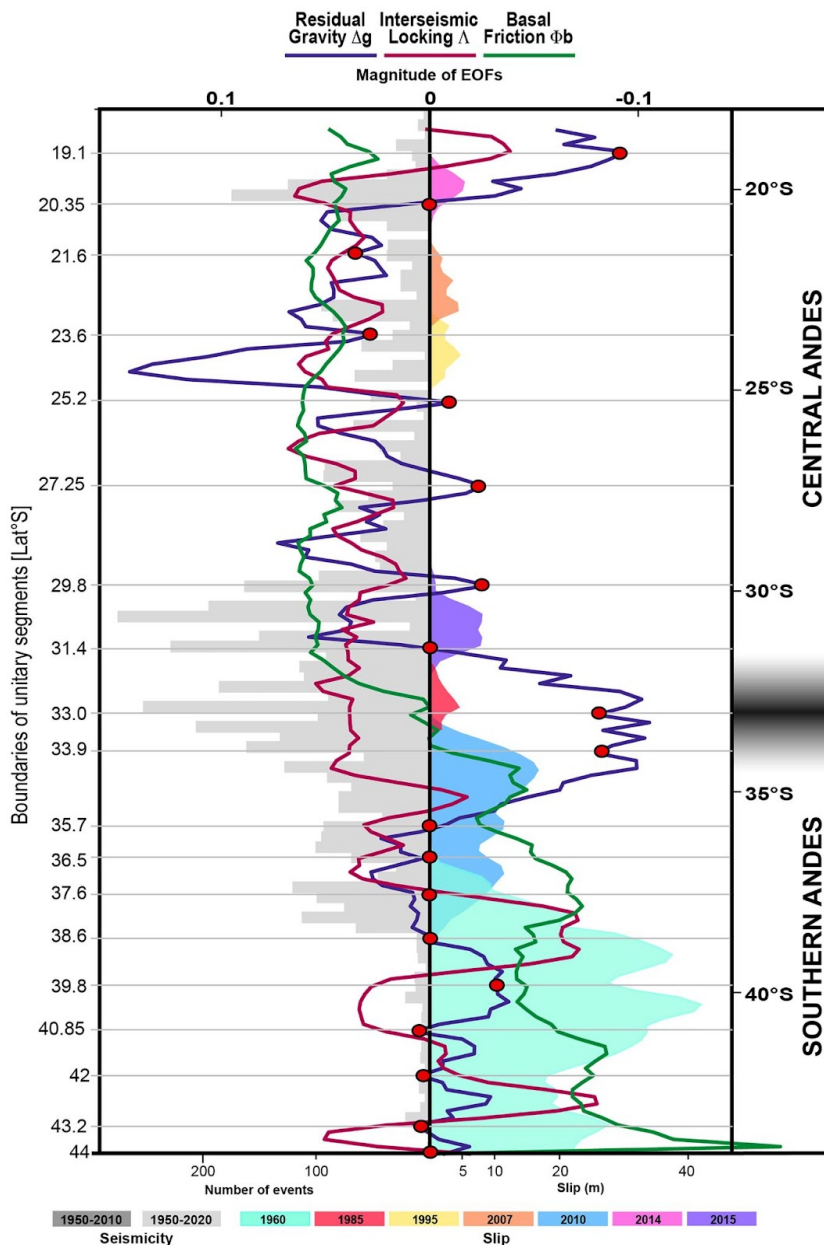


Figure 2.7: Relationship between along-trench tendencies of frictional proxies and seismic behavior. The magnitude of Empirical Orthogonal Functions (EOFs) obtained for $k = 1$ and $C = 3$ (as in Figure 2.4b) for each proxy is projected along the trench and compared with the number of seismic events and maximum slip of large megathrust earthquakes (as in Figure 2.6). We selected points (red circles) where the residual gravity anomaly intersects the origin of the abscise (i.e., EOF $\Delta g = 0$) or shows a strong local maxima/minima and use them to define the boundaries of unitary seismic segments that are shown in Figure 2.8.

values of EOF Δg , can explain the overall southward decrease in shear traction that is marked by the tendency of EOF Λ . In spite of this long wavelength (1000 km) relationship between the three proxies, we note that their short wavelength (100 km) tendencies are less similar along the Southern Andes than what can be appreciated for the Central Andes. This could be due to the larger amount of fluids inside a kilometric-scale subduction channel in the south (e.g., ; Dielforder et al., 2020; Lamb & Davis, 2003; Seno, 2009) that can reduce friction and directly counteracts the influence of σ_n on shear stress by increasing the pore pressure.

In addition, the magnitude of the normal stress itself should be lower than further north as implied by the mostly negative gravity anomaly. As predicted by Equation 2, a VW seismogenic zone loaded by low effective normal stress (low $\sigma_n - p$) should be dominated by a conditionally stable frictional regime. Under these conditions, the nucleation of earthquakes is inhibited (e.g., Scholz, 1998), which can be the underlying cause for the reduced number of epicenters below the Southern Andes compared with the central segment (Figure 2.7). As mentioned before, conditionally stable fault patches can have a wide range of seismic behaviors as predicted by dynamic rupture models (e.g., Avouac, 2015; Barbot et al., 2012; Noda & Lapusta, 2013), including anomalously large coseismic slip. Our results suggest that this could be the most likely situation underneath the Southern Andes.

We suggest that the inferred first-order differences in the frictional structure between the Central and Southern Andean megathrust have a major impact on the whole deformation mechanism of the continental margin and its crustal structure. These inferred differences imply a higher megathrust shear stress in the north compared to the south, which has been largely shown (e.g., Dielforder et al., 2020; Froidevaux & Isacks, 1984; Lamb & Davis, 2003; Sobolev & Babeyko, 2005) as a fundamental requirement to balance in the Central Andes the huge vertical body forces associated to the isostatic support of high orogenic elevations (>4,000 m) and large crustal roots (>70 km; Tassara & Echaurren, 2012). In contrast, moderate elevation (<2,500 m) and normal crustal thickness (<40 km) along most of the Southern Andes suppose a much smaller vertical load that is counterbalanced by a lower megathrust shear stress (Dielforder et al., 2020; Lamb, 2006; Seno, 2009). This agrees with the low friction and mostly conditionally stable frictional regime that we propose for the Southern Andean megathrust. Thus, our results confirm the conclusions of several

previous authors and further suggest that the differences between Central and Southern Andes are not only due to the contrast in megathrust friction alone but also by the dominant frictional stability regime implied by the contrast in residual gravity anomaly. Indeed, the connection between forearc gravity and orogenic structure via the suggested mechanism makes our interpretation of gravity anomalies much more coherent than the hypothesis of Song and Simons (2003). This is because they argue that gravity highs are caused by low friction and vice versa, which is impossible to reconcile with the force balance of the orogenic structure along the Andean margin. Instead, if gravity highs are related to a positive VW effect inside a frictionally unstable seismogenic zone in contrast to gravity lows being related to conditionally stable conditions, the relation between forearc gravity and Andean structure stands.

2.5.2.2. Small-Scale ($<10^2$ km) Variability and Seismic Segmentation Model for the Chilean Margin

We observed in Figure 2.7 a good correlation between the remarkable latitudinal variability of EOF Δg and along-strike patterns of coseismic slip. Therefore, we define a smaller scale ($10^1 - 10^2$ km) segmentation model based exclusively on EOF Δg . For this, we initially choose as unitary segment boundaries all those points in Figure 2.7 that are marked by the condition EOF $\Delta g = 0$ (in our final segmentation model they are the boundaries at 20.35°S, 31.4°S, 35.7°S, 36.5°S, 37.6°S, 38.6°S, 40.85°S, 42°S, 43.2°S, and 44°S). However, we noted that between 25° and 31°S there are three regions where such a selection would be better done (in terms of identifying a clear and marked segment boundary) if we considered the notable local minima of EOF Δg that lays in between two nearest points where EOF $\Delta g = 0$ (unitary segment boundaries at 25.2°S, 27.5°S, and 29.8°S). Keeping this last criterion in mind, we also noted other six regions where the intermediate to long wavelength tendency of EOF Δg was reverted by the occurrence of local minima or maxima, and that these points tend to coincide with the limits of coseismic slip patterns. Based on these observations, we decided to also include these points in the segmentation model (unitary segment boundaries at 19.1°S, 21.6°S, 23.6°S, 33.0°S, 33.9°S, and 39.8°S).

We note that the along-strike slip areas of all the $M_w < 8.5$ earthquakes that ruptured unitary coseismic asperities below the Central Andean forearc are strongly limited by the boundaries of our segments. The Valdivia 1960 and Maule 2010 earthquakes reached their larger size by rupturing multiple asperities across several of our proposed segment boundaries. Yet, these boundaries seem to coincide with lows in the along-strike slip distribution of these earthquakes (Figure 2.7). Most of the segment boundaries are also apparent in the latitudinal tendencies of the other two proxies, although their recognition using only EOF Φ_b and EOF Λ is difficult.

In order to generate georeferenced polygons of the unitary seismic segments, we projected the latitude of each identified boundary at the trench (as in Figure 2.7) inland for 150 km perpendicular to the trench axis (i.e., the total length of the original trench-perpendicular profiles used for PCA). By joining the end points of these trench-perpendicular lines we created the polygons representing our unitary seismic segments (Table S1). These polygons are plotted in Figure 2.8 on top of the maps obtained for each frictional proxy considering the first mode ($K = 1$) and triple PCA combination ($C = 3$). Figure 2.8 allows to better appreciate the relation between segment boundaries and strong latitudinal gradients of the residual gravity anomaly and to see that most of these boundaries are also marked in the Φ_b and Λ maps.

Maps of Figure 2.8 also offer a more explicit view of the first order spatial correlation of frictional proxies between them, with the slip distribution of instrumental earthquakes and rupture zones of historical events. This allows us to provide an extended description of small-scale variations of the proxies and their relation to underlying changes in the frictional structure of the megathrust. Particularly and as noted above, the Central Andean forearc is overall characterized by positive values of the three proxies, pointing to an elevated shear stress (high Λ) as a consequence of large values of basal friction (high Φ_b) and normal stress b (high Δg). Inside this tendency, zones of reduced gravity anomaly (i.e., lower normal stress) that define the boundaries of our unitary seismic segments strongly coincides with zones of reduced locking (low shear stress) and less clearly with areas of low friction (most notably at 27.3°S and particularly at 23.5°S where it coincides with the Mejillones Peninsula). The strong positive correlation between the three proxies is less obvious southward of 31.5°S , that is, transitioning toward the Southern Andean segment. For

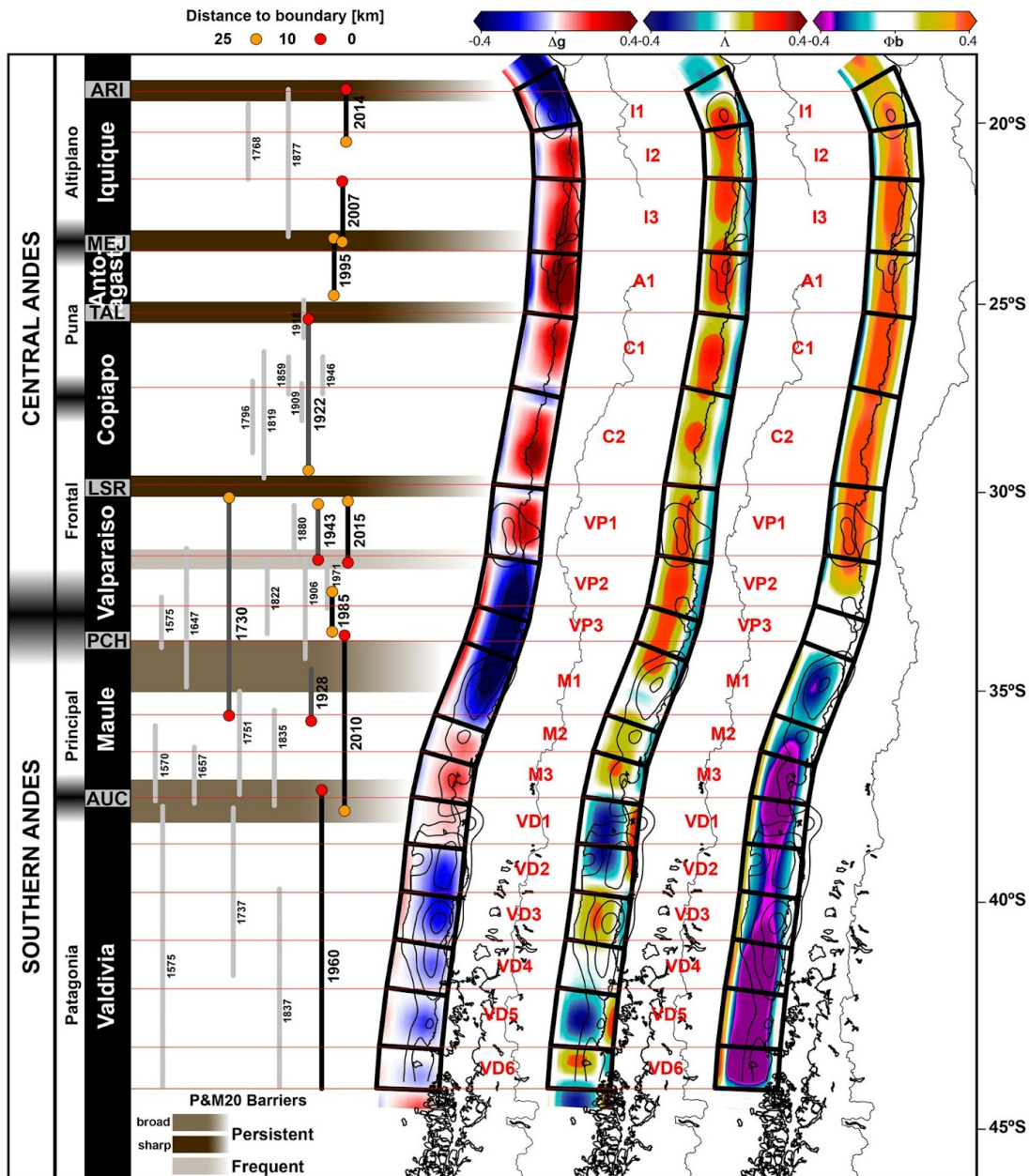


Figure 2.8: Seismic segmentation model. Right half: unitary seismic segments (polygons with black outline) are plotted on top of maps obtained for each frictional proxy (Δg residual gravity anomaly, Λ degree of interseismic locking, Φ_b basal friction) after considering only the first mode for the triple Principal Component Analysis combination (i.e., $k = 1$ and $C = 3$ in Figure 2.5). These maps also show the slip distribution of instrumentally recorded earthquakes (with contouring as in Figure 2.1). Thin red lines mark the intersection of unitary segment boundaries with the trench. Red labels inside each segment indicate its identification code that is formed by the first letter of the respective master segment and a number ordered from north to south. Left half: vertical lines represent length of earthquake ruptures that are well-constrained (black line) by modern slip models of instrumental data, moderately constrained (dark- gray lines) by old instrumental data (Beck et al., 1998) or modeling of historical evidence (Carvajal et al., 2017), and badly constrained (light-gray lines) by historical information (Beck et al., 1998; Cisternas et al., 2018; Comte & Pardo, 1991; Saillard et al., 2017).

Colors at termination points of well- and moderately constrained ruptures give a range of distance to the closest segment boundary. Brown horizontal bands show the location and categorization of seismic barriers proposed by Philibosian and Meltzner (2020; P&M20). The leftmost panel shows segments and names associated to the first and second-order orogenic segmentation (black letters on white background; Tassara & Yáñez, 2003) and our definition of master seismic segments (white letters on black background). Master segments are bounded by barriers named ARI (Arica), MEJ (Mejillones), TAL (Taltal), LSR (La Serena), PCH (Pichilemu), and AUC (Arauco).

instance, the gravity anomaly is markedly negative in the unitary segments VP2, VP3, and M1 suggesting a rather low normal stress. As friction also changes along these segments from positive to negative, it may be expected to observe a negative locking anomaly attesting for a low shear stress. However, this is true only for segment M1 (area of the maximum coseismic slip of the 2010 Maule earthquake), whereas segments VP2 and VP3 show high locking. A similar situation is observed in segments VD3 and VD6 that are also characterized by positive values of Λ and negative Φ_b and Δg . As mentioned above, negative values of the long-term frictional proxies (Φ_b and Δg) inside the VW seismogenic zone can be related to a conditionally stable regime. This allows a range of possible short-term seismic behaviors, including the possibility to become locked and accumulate slip deficit that can be translated in high values of Λ as observed for these particular unitary segments. In this sense, high locking here is not necessarily related to high shear stress associated to unstable-sliding friction as in the Central Andean segments but to the transient coupling of conditionally stable patches.

The only region south of 33°S where the normal stress could be high enough (EOF $\Delta g > 0$) to keep the megathrust in a dominantly unstable condition is the Arauco Peninsula (segments M2, M3, and VD1). This is true even considering the rather low basal friction observed there because frictional stability regimes are not controlled by friction itself but by the combination of normal stress and material properties (see Equation 2). The Arauco Peninsula is the largest morphostructural anomaly of the Andean forearc (Jara-Muñoz et al., 2015; Melnick et al., 2009; Saillard et al., 2017) and is characterized by a relatively high seismicity rate, being also the nest for most of the large earthquakes of the southern segment (i.e., Melnick et al., 2009; Ojeda et al., 2020; Ruiz & Madariaga, 2018; Tassara, 2010). This includes the 1960 and 2010

earthquakes, which occurred respectively at the southern and northern limits of the Arauco Peninsula. The recurrence interval informed by historical and continuous paleoseismic records derived from independent proxies for predecessors of the giant 1960 earthquake (Cisternas et al., 2005, 2018; Kempf et al., 2020; Moernaut et al., 2018) is ~ 300 years. Whether such a short recurrence interval for great-to-giant earthquakes is different to what could be observed along the dominantly unstable-friction Central Andean megathrust (for which paleoseismic records are scarce and inconclusive; Leon et al., 2019; Vargas et al., 2005) or if this is a characteristic feature of a predominantly conditionally stable megathrust, is not warrant at the moment. Comparison with other subduction zone segments characterized by gravity lows and with predictions of dynamic rupture models in the future could be useful to explore this hypothesis.

Complementary to Figure 2.7, we note in Figure 2.8 that the identified unitary seismic segments strongly match the slip patches of instrumental events, both for earthquakes rupturing one asperity as well as for multi-asperity giants. We also note that all of the 13 termination points of the seven instrumentally determined rupture lengths are less than 25 km apart from one of our segment boundaries, with five of them laying within 10 km. If we add the less well-constrained rupture lengths of the 1943, 1928, 1922 (Beck et al., 1998) and 1730 (Carvajal et al., 2017) earthquakes, nine of 20 termination points would fall within 10 km of a segment boundary. Figure 2.8 also shows estimated rupture lengths of historical earthquakes but we prefer to omit their termination points from this analysis because the connection between historical information of these events and their possible slip sources has not been studied with sufficient detail, as done by Carvajal et al. (2017) to estimate the length of the giant 1730 earthquake. Nevertheless, the termination points of these badly constrained historical events also fit with the identified unitary segment boundaries.

We plotted in Figure 2.8 the extent of seismic barriers included in the global catalog of Philiposian and Meltzner (2020, hereafter P&M20) who identified and categorized barriers based on a systematic analysis of earthquakes chronologies and cyclicity patterns. All the P&M20's barriers coincide with one of our unitary segment boundaries, which is not surprising given the already appreciated coincidence with earthquakes rupture lengths. P&M20 divided their barriers in three categories:

persistent (rarely or never traversed), frequent (occasionally traversed) and ephemeral (changing location from cycle to cycle). Persistent barriers can be sharp (50 km width), allowing almost no overlap of contiguous ruptures, or broad zones (150 km width) where earthquakes of both contiguous segments can penetrate but not fully traverse. P&M20 recognized seven barriers along the Chilean margin, from which 6 are persistent and the other is frequent. This is remarkable if compared with the Peru-Ecuador margin or Cascadia where almost no persistent barriers are identified or Japan where half of them are persistent. Barriers segmenting the Central Andean megathrust (ARI, MEJ, TAL, and LSR in Figure 2.8) are all persistent and sharp, whereas two broad persistent barriers are identified along the Southern Andes. One of them (associated with PCH in Figure 2.8) is located around 35°S and its length coincides with the northernmost asperity ruptured by the Maule 2010 earthquake. The other broad barrier is the Arauco Peninsula around 37.5°S (AUC in Figure 2.8). It is noteworthy to mention that there is only one other broad persistent barrier in the P&M20 catalog, corresponding to the Central Mentawai segment along the Sumatra megathrust. Whether this region shares some structural similarities with the southern Andean barriers is unclear, although at least it doesn't seem to be related to any morphological anomaly or correlated with a zone of reduced interseismic locking degree (Philibosian & Meltzner, 2020), as is the case in Chile. In fact, all the Chilean persistent barriers are associated with zones of relatively low locking inside an overall high locking megathrust as has been documented by previous authors (Chlieh et al., 2004; Metois et al., 2016; Moreno et al., 2010, 2012; Philibosian & Meltzner, 2020; Saillard et al., 2017) and can be clearly appreciated in Figure 2.8. As shown by Saillard et al. (2017), these low-locking persistent barriers are correlated with zones of permanent coastal uplift as evidenced by rapidly uplifted Quaternary marine terraces around Peninsulas.

As we acknowledge the coincidence between our segment boundaries and those proposed by P&M20, we find it useful to follow their definition of master seismic segments. A “master segment” represents for them “the maximum-length rupture that can plausibly occur on that section of the fault” and in this sense they can be fundamental inputs for seismic and tsunami hazard assessment (e.g., Gerstenberger et al., 2020). Given this definition, master segments must be bounded by persistent barriers (either sharp or broad) and can be composed by more than one coseismic

asperity. Master segments included in our model (Figure 2.8) are named as those defined by P&M20, with a minor change to reflect only names of the greatest earthquake for each segment. Based on this nomenclature, we assigned an identification code to unitary segments that considers the letters of the master segment and a correlative number from north to south (see Figure 2.8). The spatial extend of our master segments are almost identical to P&M20, which reflects the coincidence in the location of persistent barriers. This is clear for all the sharp Central Andean barriers and the AUC barrier, which is centered in the segment boundary that we located at 37.5°S. However, our PCH barrier is located at the northern limit of the broader Constitución-Pichilemu barrier of P&M20 that coincides with our unitary segment M1.

P&M20 identified one frequent barrier that coincides with the boundary between segments VP1 and VP2.

This barrier was traversed by the giant 1730 earthquake but constitutes the southern limit of the 1943 and 2015 earthquakes and the northern limit of the 1906 and 1822 events. Several of our unitary segment boundaries that were unrecognized by P&M20 could be also categorized as frequent barriers, since they have been traversed by great earthquakes but limited the rupture propagation of smaller intersegment events. Some of our boundaries have never limited well-constrained ruptures. However, the boundary at the center of the Copiapo master segment for instance seems to be the limit of some badly constrained historical events and is associated to frictional heterogeneity as suggested by time-dependent rupture features of the 1922 earthquake (Beck et al., 1998) and the occurrence of seismic swarms (Ruiz & Madariaga, 2018). Similarly, unitary segment boundaries unrecognized by P&M20 along the Valdivia master segment seems to fragment the slip distribution of the 1960 giant into several sub-asperities (Figure 2.8). In this sense, it is worth to note that the Mw7.6 Melinka 2016 earthquake (Moreno et al., 2018) ruptures within segment VD6 and its northern limit coincides with a unitary segment boundary that was apparently traversed by great historical earthquakes in southern Chile (1960, 1837 and 1575).

The intermediate-scale (10 2 km) segmentation level provided by master segments nicely bridges scales between the unitary seismic segments and the first-order

margin segmentation. The coincidence between most of the master seismic segments and second-order orogenic segments, as noted in Figure 2.8, further support the suggested long-term link between the frictional structure of the megathrust and the construction of the Andean cordillera.

2.5.3. Structural Controls on Seismic Segmentation

One important question regarding seismic segmentation patterns is the physical nature of barriers and their possible link to structural features of both converging plates (e.g., Aki, 1979; Bassett & Watts, 2015a, 2015b; Bilek & Lay, 2018; Lay & Kanamori, 1981; Philiposian & Meltzner, 2020; Wang & Bilek, 2014). Although the adjective “persistent” refers to quite different time-scales when applied to earthquake rupture segmentation (10^2 – 10^3 yr) compared to plate structure (10^5 – 10^6 yr), it is expectable that persistent seismic barriers can be related to persistent structural features of the subduction zone, more precisely to geologic structures of one or both plates.

Oceanic ridges, seamount chains and fracture zones has been proposed to act as barriers globally (e.g., Bassett & Watts, 2015a, 2015b; Wang & Bilek, 2014) and along the Chile Margin (e.g., Carena, 2011; Contreras-Reyes & Carrizo, 2011; Sparkes et al., 2010; Saillard et al., 2017). We note in Figure 2.9 that all the subducting bathymetric anomalies are directly related to one of our unitary segment boundaries. Most of them (Iquique Ridge, Mejillones FZ, TalTal Ridge, Challenger FZ, Mocha FZ) are related to persistent barriers but some others (Copiapo and Juan Fernandez Ridges) are not. For the case of the frictionally unstable megathrust underneath the Central Andean forearc and the Arauco Peninsula, the subduction of oceanic features should be related to a reduction of the VW effect, shifting the frictional regime to a conditionally stable situation for which creep is possible (as imaged by reduced locking in Figure 2.8 and noted by Metois et al., 2016 and Saillard et al., 2017). In this context, the coincidence of some peninsulas with persistent barriers, via reduced interplate locking, creeping and enhanced upper plate deformation, can be a consequence of an underlying subducting plate control as suggested by Saillard et al. (2017). The shift from unstable to conditionally stable friction along subducted features could be due to a localized increase in pore pressure, as water contained in sediments deposited at flexural moats (Bassett &

Watts, 2015a, 2015b) and/or inside the over-fractured hydrated lithosphere around seamounts (e.g., Kopp et al., 2004) can be expelled into the megathrust. The enhanced hydration of the subducting oceanic plate and focusing of water influx into the upper plate above subducted anomalies reduces density and can explain the reduced gravity anomaly.

Other three fracture zones are related to segment boundaries along the Valdivia master segment. However, as we infer that the megathrust here is dominated by a conditionally stable frictional regime, a further reduction of the already low effective normal stress is unlikely. In addition, we note that all the subducting features are associated with segment boundaries but not all these boundaries correlate with a subducted anomaly, implying that the subduction of a bathymetric anomaly is a sufficient but not necessary condition to create a seismic barrier, as also observed by others (e.g., Philiposian & Meltzner, 2020; Wang & Bilek, 2014). The upper plate geologic structure must be likely playing a role. Such a role has been suggested at other subduction zones (e.g., Collot et al., 2004; Li & Liu, 2017; Wells et al., 2017) and along the Chilean margin (Bejar-Pizarro et al., 2013; Jara-Muñoz et al., 2015; Melnick et al., 2009; Saillard et al., 2017; Sobiesiak et al., 2007; Tassara, 2010; Victor et al., 2011). Similar to ocean floor anomalies, upper plate structures can influence rupture segmentation creating geometric discontinuities, frictional heterogeneities and/or focused fluid flow (e.g., Philiposian & Meltzner, 2020) and delimiting rock bodies with contrasting lithologies and physical properties. We compare in Figure 2.9 our unitary seismic segments with a simplified geologic map of the Chilean forearc that highlight main lithologic contrasts between igneous-metamorphic basement units. This is compared with the residual gravity anomaly map obtained when considering the triple combination ($C = 3$) and the two higher PCA modes ($K = 1 + 2$ in Figure 2.5). As expected, this map shows more detail than the gravity anomaly map of Figure 2.8 and we preferred it here because it allows us to better appreciate a possible relationship with the smaller-scale geologic structure. Figure 2.9 also includes a map of the average forearc density that was computed from the seismically constrained 3D density model of Tassara and Echaurren (2012).

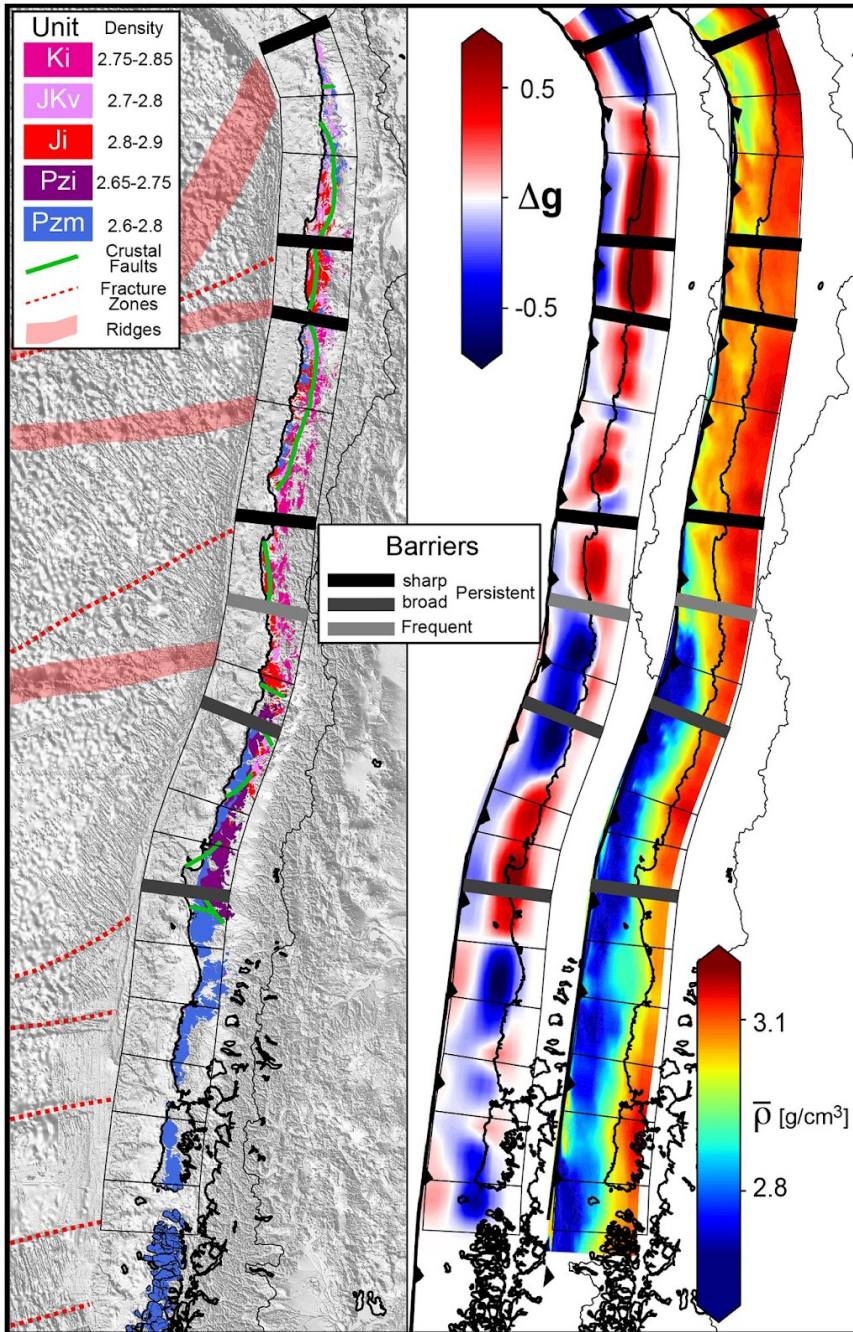


Figure 2.9: Comparison between residual gravity, density and geologic structure. Right panel shows the reconstructed map of Δg for $C = 3$ and $k = 1 + 2$ (as in Figure 2.5) with inferred segments of the seismogenic zone (Figure 2.6) and a map of average forearc density computed from the 3D density model of Tassara and Echaurren (2012). Left panel shows a shaded-relief topography-bathymetry map (GEBCO_2020 grid) on top of which we plot the main geological units of the Chilean forearc (Ki: Cretaceous intermediate intrusives. JKv: Jurassic-Cretaceous intermediate-mafic volcanics. Ji: Jurassic intermediate-mafic intrusives. Pzi: Upper Paleozoic intermediate-felsic intrusives. Pzm: Upper Paleozoic metamorphic complex) extracted from the 1:1.000.000 geological map of Chile (SERNAGEOMIN, 2002) and bathymetric anomalies of the Nazca plate.

We first note a major difference in the geologic configuration of the Central and Southern Andean segments. The Coastal Cordillera north of 33.5°S predominantly consists of Mesozoic mafic-to-intermediate igneous rocks and isolated Paleozoic metasediments. Contrastingly, the Southern Andean forearc is mostly formed by larger sections of the metamorphic complex that are locally intruded by intermediate composition granitoids of the Late Paleozoic. Based on the lithologies of each geologic unit and following the characterization of rock density of Tassara et al. (2006), we assigned ranges of density to these units. We observe that the upper crust is denser along the entire Central Andean forearc and segments M2 and M3 (Arauco Peninsula) compared to the rest of the Southern Andean forearc. This tendency is also reproduced by the average forearc density, although this is much clearly observed in the offshore than along the Coastal Cordillera. The described spatial tendencies of surface and bulk crustal density are fully consistent with the pattern of Δg suggesting a first-order control of the long-term geologic structure of the upper plate on the already discussed large-scale megathrust frictional segmentation.

At a smaller scale, we note a clear correlation between boundaries of master segments and upper crustal faults. All the persistent barriers are associated to notable trench-ward inflections in the strike of margin-parallel fault zones and/or the occurrence of (mostly) NW-oriented structures. The most notable upper crustal faults are imaged by pronounced topographic lineaments in Figure 2.9 and are related to the old geological structure of the margin, for example, the Cretaceous Atacama fault zone in northern Chile (e.g., Charrier et al., 2007) or the Late Paleozoic NW-oriented Lanahue fault at the south of the Arauco Peninsula (e.g., Melnick et al., 2009). In addition, some unitary segment boundaries, unrecognized as P&M20 persistent barriers, are also associated to upper plate faults, as is most notable for the Valparaiso and Maule segments. Indeed, the coseismic slip segmentation of the 2010 Maule earthquake has been already related to a very likely upper plate control (Bishop et al., 2019; Hicks et al., 2014; Jara-Muñoz et al., 2015; Moreno et al., 2012).

Large upper plate faults can control from above the occurrence of geometric, frictional and/or hydraulic heterogeneities on the megathrust (e.g., Philipposian & Meltzner, 2020) and they also delimit blocks with contrasting lithologies and

densities. The occurrence of a large and high-density batholith on top of the asperity ruptured by the Antofagasta 1995 earthquake is remarkable (Sobiesiak et al., 2007), as it is the presence of a high V_p crustal anomaly associated to a Paleozoic batholith that is located 10–20 km eastward to the epicenter of the Maule 2010 earthquake (Hicks et al., 2014). This anomaly is related to a gravity high observed at the boundary between unitary segments M1 and M2 (Figures 2.8 and 2.9). This gravity high prolongs southward into the Arauco Peninsula and coincides with the extension of a large Upper Paleozoic batholith that is also marked by high seismic velocities (Haberland et al., 2009; Moreno et al., 2014) and density (Tassara, 2010). In this sense, the AUC barrier can be described as a large high-density anomaly immersed (intruded actually) into a forearc mostly composed by the low-density Paleozoic metamorphic complex.

Finally, we observe that our unitary segment boundaries are always associated to an anomalous geologic feature of at least one of the plates. Between these boundaries however, persistent barriers seem to be related in Figure 2.9 to the particular situation where subducting plate anomalies and crustal faults meet at then megathrust, mutually reinforcing their potential effects on the frictional regime at the seismogenic zone and creating patches of large frictional heterogeneity that always stops seismic rupture propagation. Similar analysis considering the geologic structure of both plates along other subduction zones could test in the future the generality of this important conclusion.

2.6 Conclusions

We believe that our contribution for the understanding of megathrust seismogenic processes at multiple spatial and temporal scales is varied and we hope that researchers interested in this topic will appreciate both the methods developed here and the mechanical interpretations of our results.

On one side, we show how the classical statistical method of Principal Component Analysis (PCA) can be efficiently applied to (a) generate an adequate description of residual gravity anomalies at the scale of an entire subduction zone, overcoming the problem that other methods (based on one average trench-perpendicular profile)

have when applied to zones that are several thousand km long, (b) analyze the spatial correlation between different proxies of the frictional structure of the megathrust (in this case residual gravity, basal friction from wedge taper theory and interseismic geodetic locking), and (c) provide a first-order representation of common trench-perpendicular and along-trench tendencies that can be used to infer major spatial changes on seismogenic behavior, the underlying mechanical processes and possible controlling factors. Particularly relevant is the use of along-trench changes in the sign (polarity) of the Empirical Orthogonal Function (EOF) derived from residual gravity to map unitary segment boundaries at 10^2 km scale. The strong correlation that we observe between these segments, rupture length of historical events and slip patterns of instrumental earthquakes does demonstrate the very potential of this method. The application to other subduction zones in the future will prove whether this correlation is valid only for the Chilean case or can be expanded globally.

By the other side, the application of the rate-and-state friction (RSF) law to interpret the spatial variations identified by PCA resulted in a particularly useful conceptual framework that delivered a number of significant conclusions. For instance, a quite similar trench-perpendicular tendency of the three frictional proxies (showing a central zone with positive PC magnitudes and negative magnitudes trenchward and downward of this zone) is interpreted in this framework as imaging the extend of the velocity-weakening (VW) seismogenic zone bounded by velocity-strengthening zones outside its updip and downdip limits. Positive PC magnitudes for the three proxies show that high shear traction (directly related by others to the degree of fault locking) at the center of a VW seismogenic zone is the result of high basal friction (directly shown by our results) and high effective normal stress (indirectly shown by our results as high gravity anomaly that should be connected to high density and therefore high vertical stress loading the fault). The trench-perpendicular location of the seismogenic zone could be also inferred just by advocating a common rate-independent friction, as it is also the main latitudinal difference between the Central Andean (high values of shear traction, friction and normal stress) and Southern Andean (low values for all of them) megathrust. However, the use of the RSF law allows for a richer fan of possible interpretations regarding the along-trench

variations. Particularly and in comparison with a gradual north-south decrease of locking (shear traction) and friction along the limit between Central and Southern Andean forearc segments, the strong latitudinal variation of the EOF magnitude for gravity anomaly (EOF Δg) that is associated with the seismic segmentation can be interpreted in the RSF conceptual framework as connected to variations of the frictional stability regime inside the VW seismogenic zone. Positive EOF Δg for most of the Central Andean segment and the Arauco Peninsula (nest of the giant 1960 and 2010 earthquakes) is here connected to an intense VW behavior and unstable-sliding frictional regime. Negative EOF Δg along the rest of Southern Andean forearc (which include master seismic segments related to the 1960, 2010 and the giant 1730 earthquakes) must be related to a conditionally stable frictional regime that opens a range of possible seismogenic behaviors as has been demonstrated by numerical dynamic rupture models. This includes interseismic fault creep or lock, coseismic rupture arrest or large slip activated by a sufficiently rapid rupture front propagation. As suggested by the observation of high interseismic locking patches coinciding with huge coseismic slip in regions of negative EOF Δg , inferred conditionally stable segments are actually associated with this peculiar and dangerous seismogenic behavior. In addition, the established RSF conceptual framework and a detailed characterization of the geological structure of both plates, offers us a powerful tool to analyze the controlling factors behind the persistency of seismic barriers. We concluded that persistent barriers (not traversed by great tsunamigenic earthquakes) are likely related to the eventual meet at the megathrust of anomalous structural features of both converging plates, whereas frequent barriers (traversed by great events but segmenting smaller ones) seem to be related to structures of only one plate. Numerical models of dynamic rupture initiation and propagation in the future that could be inspired in some of our conclusions will test these hypotheses and their applicability to other subduction zones.

The seismic segmentation model that we left available as part of the Supporting Information can be used for a number of applications, being its use for seismic and tsunami hazard at a nation-wide scale one of the most significant. As grids of gravity anomalies are freely available, our method to recognize boundaries of unitary seismic segments from EOF Δg can be easily applied to Sumatra, Japan and Cascadia to be compared with the barrier catalog of Philiposian and Meltzner (2020)

and then to any subduction zone in order to provide viable models of seismic segmentation useful for hazard assessment. The computational codes along with input and output files used in our analysis are freely available at <https://zenodo.org/record/4539046#.YCbuc3VKg5k>; we hope they can be useful for those interested in pursuing similar research projects.

Acknowledgments

This work was partially funded by the National Agency for Research and Development (ANID)/Scholarship Program/DOCTORADO BECAS CHILE/2017—21171169. We also acknowledge partial support by the Millennium Scientific Initiative (ICM) of the Chilean government through grant NC160025 “Millennium Nucleus CYCLO The Seismic cycle along subduction zones”, FONDECYT grants 1181479 and 1190258, the ANID PIA Anillo ACT192169. We gratefully appreciate the suggestions and comments of Jack Loveless, an anonymous reviewer and the Associate Editor.

References Chapter 2

The reference list cited in Chapter 2 is part of the **Thesis Reference** section at the pag 147.

3. Slip behavior of velocity-weakening barriers

Chapter three has been submitted as an article to the journal *Nature Geosciences* on March 22th, 2022.

Slip behavior of velocity-weakening barriers

Diego Molina ^{1,2}, Jean-Paul Ampuero ³, Andrés Tassara ^{1,2}

1 Departamento Ciencias de la Tierra, Facultad de Ciencias Químicas, Universidad de Concepción, Concepción, Chile,

2 Millennium Nucleus The Seismic Cycle Along Subduction Zones CYCLO, Valdivia, Chile,

3 Université Côte d'Azur, IRD, CNRS, Observatoire de la Côte d'Azur, Géoazur, Sophia Antipolis, France,

Abstract

Seismic barriers are fault portions that promote earthquake rupture arrest and fault segmentation. Despite their fundamental role in controlling the maximum magnitude of earthquakes, the nature of seismic barriers is still uncertain. A common interpretation of barriers as having velocity-strengthening (VS) friction, i.e. steady-state friction increases with increasing slip velocity, is inconsistent with the thermal control of friction observed in laboratory experiments which implies that most subducted VS materials eventually turn velocity-weakening (VW) at some depth. Here we examine the possibility of VW barriers by conducting earthquake cycle simulations along a VW megathrust segmented by lateral variations of frictional properties and normal stress. Here we show that VW fault segments display a wide range of behaviors, including permanent barrier behavior. They can be locked during long periods and release their slip deficit either seismically or aseismically. We quantify the efficiency of VW barriers in arresting ruptures by a non-dimensional parameter based on fracture mechanics theory which can be constrained by observations on natural faults. This work provides insights on how tectonic features may control earthquake patterns and advances the theoretical underpinnings of physics-based hazard assessment.

3.1 Introduction

Understanding the mechanisms controlling earthquake arrest and limiting the size of their ruptures, is crucial to elucidate the physics governing seismicity patterns along segmented faults and to advance physics-based seismic hazard assessment. Faults are often segmented into “asperities” experiencing large slip during earthquakes, separated by “barriers” that prevent earthquake propagation (Aki, 1979; Lay and Kanamori, 1981). The origin of barriers in subduction megathrust faults has been attributed to reduced stresses due to past ruptures, ductile behavior at high temperatures (Wang and Bilek, 2014), geometrical fault bends (Wesnousky, 2006), subducted bathymetric anomalies (Contreras and Carrizo, 2011; Sparkes et al., 2010) and upper plate geological structures (Jara-Muñoz et al., 2015; Melnick et al., 2009; Saillard et al., 2017). Barriers frequently overlap with features arising from long-term geological processes, such as geological structures of the overriding plate (Collot et al., 2004) and positive gravity anomalies (Basset and Watts, 2015b), suggesting a persistent barrier behavior. However, some barriers lie in zones of negative or null gravity anomalies, potentially revealing a role of heterogeneous friction (Tassara, 2010; Molina et al., 2021). Moreover, barriers can display non-systematic long-term behavior. Most regions that have acted as seismic barriers during large historical earthquakes present diverse slip behaviors in modern instrumental records, ranging from aseismic to seismic slip. Geodetic observations indicate that regions where earthquakes stop host aseismic slip, either interseismically or postseismically (Wang and Bilek, 2014; Saillard et al., 2017; Plata-Martinez et al., 2021), and areas that once behaved as barriers have participated later in earthquake ruptures (Basset and Watts., 2015a; Ojeda et al., 2020). Seismic barriers have been categorized into persistent, frequent and ephemeral, according to the frequency of earthquakes traversing them (Philibosian and Melzner, 2020). Models with uniform fault friction properties can exhibit spontaneous segmentation and heterogeneous stresses (Horowitz and Ruina, 1989; Cattania, 2019), but cannot explain barriers that persist over time scales much longer than several seismic cycles. Persistent seismic barriers arise more naturally from heterogeneities of material properties controlling fault strength.

A diversity of fault slip patterns can be numerically simulated within the framework of the laboratory-motivated rate-and-state friction (RSF) law (Dieterich, 1979; Tullis,

1988; Marone, 1998). In this framework, fault stability is controlled by the dependence of steady-state friction on slip velocity. In general, velocity-strengthening (VS) regions, where friction increases after a sudden increase in slip velocity, favors slow aseismic slip and earthquake arrest, while velocity-weakening (VW) zones promote earthquake nucleation and rupture propagation due to the decrease of friction following a rapid slip pulse. It seems logical in this context to assume that seismic barriers are VS fault areas segmenting asperities formed by VW zones. A mechanical understanding of VS barriers is well established (Kaneko et al., 2010) and is being integrated in the assessment of the seismic potential along natural faults (Michel et al., 2021). Thus, conceptual models underneath numerical simulations commonly assume a patchy distribution of VS and VW regions to explain the distribution of, respectively, seismic barriers and asperities along faults (Barbot et al., 2012; Noda and Lapusta, 2013; Lui and Lapusta, 2016; Wei and Shi, 2020; Lambert and Lapusta, 2021).

One important implication of the VS-barrier model is that large barriers associated with the along-strike segmentation (and therefore seismic potential) of subduction megathrusts must retain their VS character across the entire plate interface, particularly at temperatures in the range expected inside the seismogenic zone of the megathrust (approx. 150-350°C, Oleskevich et al., 1999, Hippchen and Hyndman, 2008, Volker et al., 2011). However, frictional laboratory experiments show that this is possible only for a small number of studied materials (mostly clay minerals) that maintain a VS behavior at these temperatures (Saffer and Marone, 2003, Okamoto et al., 2018), whereas most of the rocks types and gouges that are relevant in the subduction environment (unaltered and altered rocks of the oceanic and continental plate, subducted sediments, etc) are VW inside this temperature range (Liu and Rice., 2009, Verberne et al., 2015, Hartog et al., 2012, Mitchell et al., 2016, Phillips et al., 2019). Further, even materials that are strongly VS at shallow depth, such as clays, eventually turn VW as they subduct, due to metamorphic processes (Spinelli et al., 2016, Sawai et al., 2016, 2017). Additionally, some natural barriers exhibit intermediate to high geodetically-estimated interseismic coupling (ISC) over wide areas (Moreno et al., 2010, Metois et al., 2016), whereas such values are expected for VS materials only in narrow stress shadow areas around locked asperities (Hetland and Simons, 2010). Thus, it seems unlikely that all

seismic barriers along subduction zones can be characterized by a VS frictional behavior. The alternative is to consider the situation exposed in Fig. 3.1a where the thermal control on RSF frictional properties impose a VW behavior inside the entire seismogenic zone but asperities and barriers emerge as patches dominated, respectively, by unstable or conditionally-stable sliding.

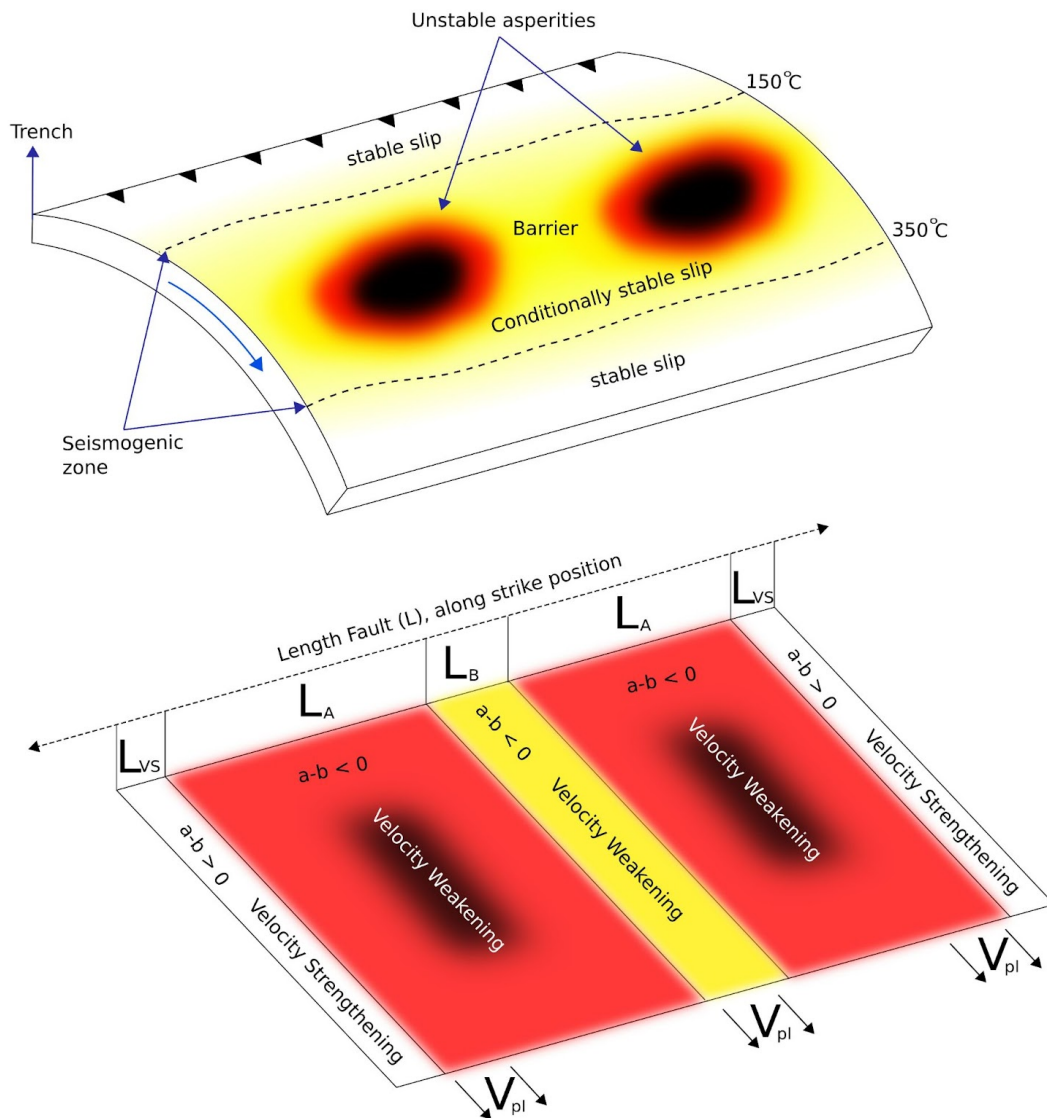


Figure 3.1: Conceptual model and numerical simulation setup. a) Conceptual sketch (not to scale) of a thermally-controlled velocity-weakening (VW, $a-b < 0$) subduction megathrust where seismic asperities and barriers are dominated by unstable and conditionally-stable sliding. b) 2.5D model setup of a fault with two seismogenic asperities (red dark bands), a central VW patch (yellow) whose normal stress σ_n and RSF critical slip distance D_c are varied systematically, and two VS ($a-b < 0$) regions (white) at the extremes of the fault. The fault is infinitely long, with spatially periodic slip along strike, and is loaded by steady slip (constant slip rate V_{pl}) at depths beyond the seismogenic width.

Previous numerical simulations of earthquake cycles at seismogenic faults shows that conditionally-stable VW segments can also promote earthquake arrest (Boatwright and Cocco, 1996, Hori and Miyazaki, 2011), but the spectrum of slip behavior displayed by VW barriers has not been characterized nor understood. Here we investigate slip patterns emerging on seismic barriers along VW faults in earthquake cycle simulations, as a function of parameters controlling the barrier strength. We further recur to fracture mechanics theory to identify factors governing the efficiency of VW barriers in arresting ruptures. Finally, we discuss the implications of our results on seismicity patterns and their possible link with structural features of upper and lower plates.

3.2 Simulating the earthquake cycle around VW barriers

We study how along-strike variations of friction properties and normal stress on a VW RSF fault can promote rupture arrest by performing quasi-dynamic earthquake-cycle simulations using the QDYN software (Luo et al., 2017a). Inspired on the conceptual model of Fig. 3.1a, the setup of our numerical simulations (Fig. 3.1b) considers a fully VW fault plane (i.e. that is characterized by a frictional stability parameter $(a-b) < 0$) embedded in an elastic medium that is surrounded by VS (i.e. $(a-b) > 0$) regions at its extremes and is loaded by uniform steady slip at depths beyond its seismogenic width (see Methods 3.1). We consider a 2.5D approximation that captures the 3D effect of the finite seismogenic width (here, 200 km) at the low computational cost of 2D simulations (see Methods 3.5). The fault contains two unstable seismic asperities of length L_A separated by a central VW patch (hereafter, CVWP) of length L_B . The asperities and the CVWP have different effective normal stress σ_n and RSF critical slip distance D_c . For models presented here, both asperities have fixed properties $L_A = 70$ km, $\sigma_n = 95$ MPa and $D_c = 0.1$ m. On the CVWP, we can independently vary the values of L_B (between 20 and 60 km), σ_n (between 95 and 400 MPa) and D_c (between 0.1 and 0.4 m). All simulations span a large number of earthquake cycles over a period of ~ 10 kyr. In reference simulations without a contrast in the frictional properties of asperities and barrier (no CVWP), all events break the whole fault (see methods 3.1).

3.3 Results

3.3.1 Diverse slip patterns on the central VW patch

Our earthquake cycle simulations produce a wide spectrum of earthquake patterns (Fig. 3.2), spanning aseismic to seismic behavior on the CVWP, similar to those observed in natural seismic barriers. For instance, the CVWP can remain strongly locked for several decades, manifested by high ISC (Fig. 3.2b and 3.2e). The accumulated slip deficit due to this high locking is eventually released seismically or aseismically via mechanisms that differ between simulations with varying D_c and/or σ_n .

In CVWPs defined by varying D_c , as this parameter is increased the nucleation length increases proportionally, making the CVWP to slip aseismically and to act as a barrier for ruptures arriving from the unstable asperities (Extended Data Fig. 1 (See Appendix A2), Fig. 3.2 d-e). These barriers can have intermediate to high ISC values, with slip deficit released mostly as afterslip, which propagates along the barrier and can penetrate the opposite asperity to trigger a new earthquake, or via a bilateral slow slip event (Fig. 3.2e). CVWPs with large D_c contrast with respect to the asperities experience variable ISC, with some cycles exhibiting high ISC and others lower ISC (Fig. 3.2f). The high ISC cycles follow cycles devoid of long after-slip migration, and culminate in earthquakes that break the whole barrier or in smaller earthquakes near the barrier edges (Fig. 3.2 d-e). In contrast, CVWPs having small D_c contrast remain strongly locked during most cycles, leading to earthquakes that break the barrier entirely or partially and produce little afterslip (Extended Data Fig. 2a-b-c (See Appendix A2)).

A CVWP defined by a σ_n contrast also experiences a wide range of behaviors, including the ability to stop earthquakes. CVWPs with high σ_n mostly slip seismically, due to their relatively small nucleation length (inversely proportional to σ_n) and high fault strength (proportional to σ_n) (Extended Data Fig. 1 (See Appendix A2)),

Extended Data Fig. 2d (See Appendix A2)). The latter enhances the locking degree of the CVWP,

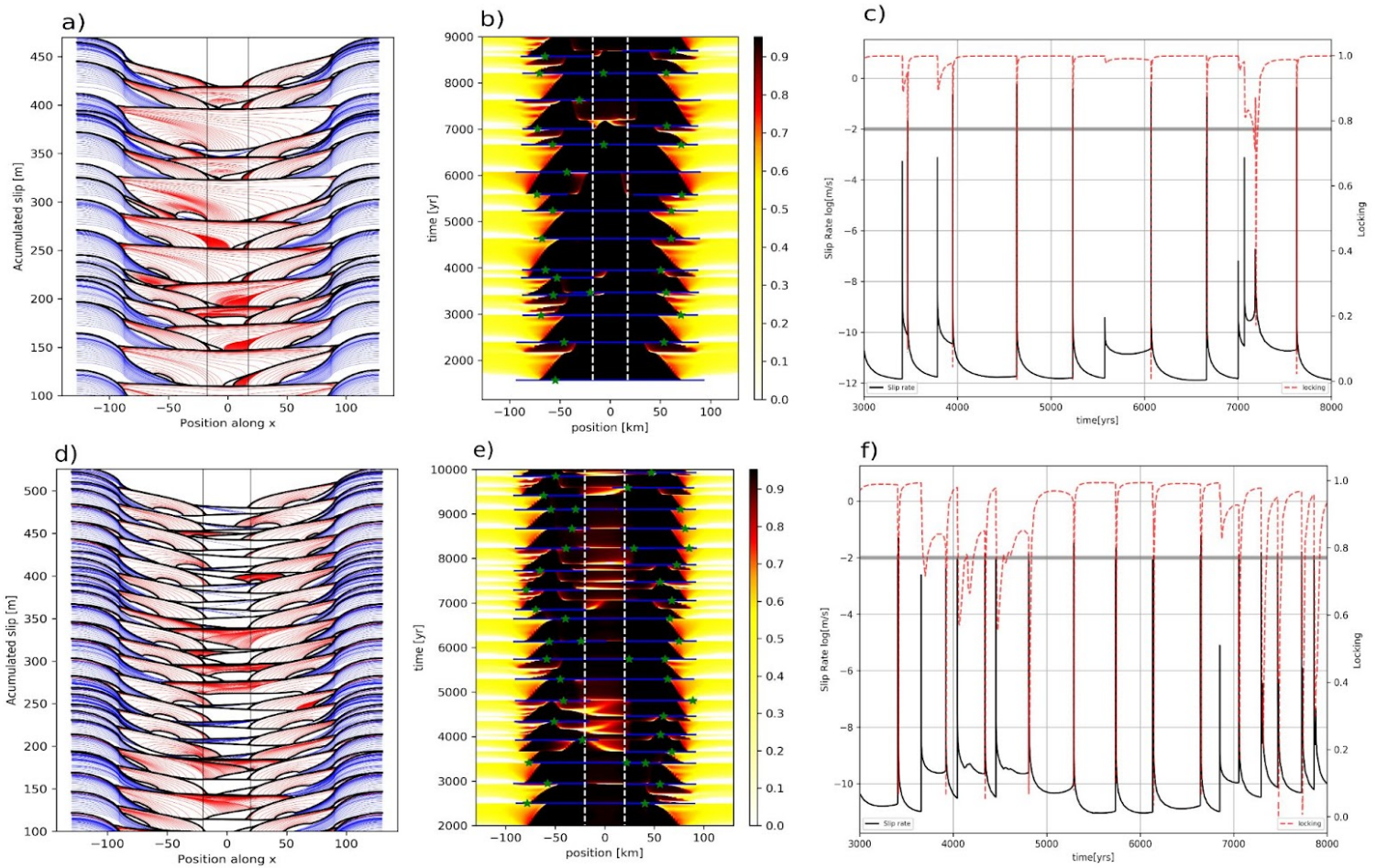


Figure 3.2: Results of seismic cycle simulations producing a frequent (top, a, b, c) and a permanent (bottom, d, e, f) barrier. The frequent barrier is characterized by $\sigma_n = 180 \text{ MPa}$, $L_B = 35 \text{ km}$, whereas the permanent barrier is defined by $D_c = 0.38 \text{ m}$, $L_B = 40 \text{ km}$. a and d) Accumulated slip (y-axis) along the fault (x-axis) during interseismic periods (blue, every 2 years) and during earthquakes (red, every 5 seconds); Black lines depict the start and ending of earthquakes. Vertical lines display the edges of the barrier. b and e) Temporal evolution (y-axis) of the instantaneous interseismic coupling (ISC, calculated as explained in the Methods 3.7) along the simulated fault (x-axis). Blue solid lines show the extent of earthquake ruptures and green stars their epicenters. Dashed white lines indicate the edges of the CVWP. c and f) Instantaneous ISC averaged along the CVWP (red dashed lines) and slip rate averaged across the fault (black solid lines, log scale) as a function of time. The horizontal gray line indicates our chosen threshold to define seismic slip rates, 1 cm/s (see Methods 3.6). Aseismic transients are those that do not reach this threshold. ISC in the CVWP varies throughout the seismic cycle, although the values are most often near 1 (fully locked).

promoting earthquakes that break it completely (Extended Data Fig. 2e (See Appendix A2)). CVWPs with intermediate σ_n can also behave as barriers, stopping ruptures within a short penetration distance, in contrast to the deep penetration found for barriers defined by a high D_c (Fig. 3.2a, Extended Data Fig. 2a (See Appendix A2)). A CVWP that behaves often as a barrier may also host a few large earthquakes because of a high ISC (Fig. 3.2 a-b-c). Earthquakes stopping in the CVWP may also trigger postseismic slip, which penetrates further into the barrier as σ_n is increased (up to twice the value in the asperities), but generally without spanning the whole barrier length (Fig. 3.2b). In some cases, two afterslip fronts coming from each side of the barrier coalesce, triggering a transient slow slip event that spans the whole barrier and part of the asperities (Fig. 3.2b). But a very large σ_n contrast does not lead to a permanent barrier. In a CVWP with σ_n exceeding about twice the value of the asperities, ISC remains high during all cycles, postseismic slip is confined mainly to its edges (Extended Data Fig. 2e-2f (See Appendix A2)), and the percentage of slip released seismically increases with increasing σ_n , without a clear distinction between rapid and slow creep (Extended Data Fig. 1 (See Appendix A2)) (see Methods 3.6).

3.3.2 From aseismic to seismic slip on VW barriers

Our simulations demonstrate that a VW segment can behave as a barrier. For each simulation, we quantify the barrier efficiency by the probability P that an earthquake breaks the whole CVWP. The value of P depends on the barrier properties (Fig. 3.3a-b): P decreases with increasing D_c and has a non-monotonic dependence on σ_n (decrease followed by increase when σ_n exceeds twice the asperities' value). Adopting the nomenclature proposed by Philiposian and Melzner (2020), we define ephemeral barriers by $P \geq 80\%$, frequent barriers by $15\% < P < 80\%$ and permanent barriers by $P \leq 15\%$. Among CVWPs defined by a D_c contrast, those that have a short length do not behave as permanent barriers (see cases with $L_B = 20$ km in Fig. 3.3c). More efficient barriers accommodate more slip aseismically: smaller P values are associated with larger ratios between aseismic and seismic slip (Fig. 3.3c).

3.3.3 Fracture mechanics on VW barriers

To better understand the physics governing VW barriers and to quantify their efficiency, we recur to Linear Elastic Fracture Mechanics (LEFM, see Methods 3.2). LEFM predicts that an earthquake can propagate through a barrier if its static energy release rate G_o is equal or higher than energy dissipated by slip in the barrier (the fracture energy G_c), in particular earthquakes propagate if $G_o \geq G_c$; otherwise they stop. Both G_c and G_o can be computed from the fault stresses obtained in our earthquake cycle simulations (see Methods 3.2).

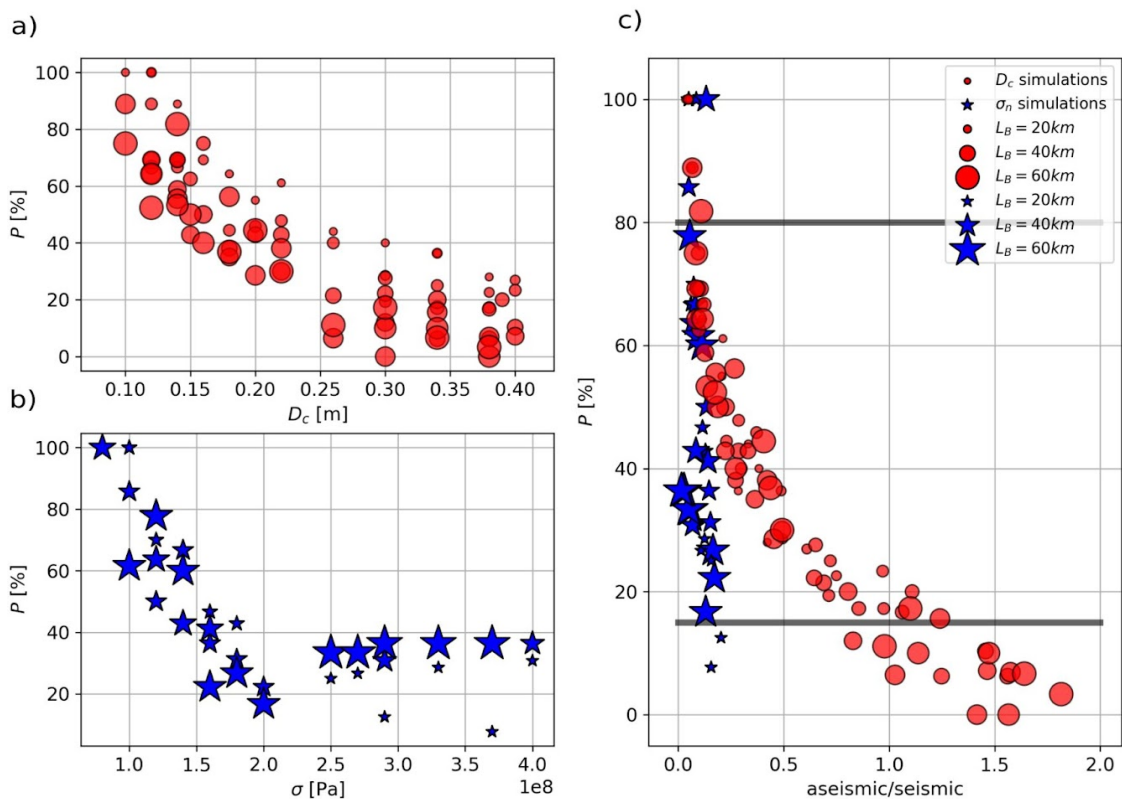


Figure 3.3: The diversity of slip behaviors in VW barriers. Probability (P in percentage) of earthquake ruptures crossing the barrier as a function of D_c (a) in CVWPs defined by a D_c contrast and of σ_n (b) in CVWPs defined a σ_n contrast. (c): Probability (P) of earthquake ruptures crossing the barrier as a function of the ratio of aseismic to seismic slip averaged inside the CVWP (see Methods 3.6), for barriers defined by high D_c (red circles) and by high σ_n (blue stars). Horizontal gray lines separate permanent ($P < 15\%$), frequent ($15\% < P < 80\%$) and ephemeral barriers ($P > 80\%$). Permanent barriers are obtained by increasing D_c but not by increasing σ_n . Symbol sizes are scaled by $L_B =$ length of the CVWP.

Our results indicate that most earthquakes stopping in the barrier satisfy the arrest condition $G_o < G_c$ (Fig. 3.4a).

Noting that G_c is proportional to D_c and σ_n (e.g. Rubin and Ampuero, 2005, equation 24), this explains why barrier efficiency increases with increasing D_c or σ_n . Thus the persistence of natural barriers could be due to spatial variations of frictional properties or normal stress that remain unchanged throughout several seismic cycles. However, our finding that permanent barriers cannot be achieved by increasing indefinitely their σ_n requires a different explanation: noting that the nucleation length is inversely proportional to σ_n , a higher σ_n tends to make the CVWP more unstable, promoting seismic slip. Notably, several natural barriers are located in zones where rupture ends overlap and might experience coseismic slip frequently (Moreno et al., 2010, Ojeda et al., 2020, Philiposian and Melzner, 2020). Our results also indicate that properties of adjacent asperities affect a barrier's efficiency. Ruptures can penetrate further into a barrier if they are more energetic when they reach the barrier, which we quantify by a higher asperity energy G_{oi} defined as the static energy release rate measured when the rupture reaches the end of the initial asperity (Fig. 3.4b).

The barrier/asperity stress drop ratio $\Delta T_b/\Delta T_a$ also influences the rupture propagation inside a barrier. For instance if G_c/G_{oi} is fixed at 1, a lower $\Delta T_b/\Delta T_a$ promotes further rupture penetration. Assuming uniform stress drop on both asperity and barrier, LEFM predicts that the barrier efficiency depends on two non-dimensional parameters, G_c/G_{oi} and $\Delta T_b/\Delta T_a$ (see Methods 3.3). Based on our ensemble of simulations (see Methods 3.3, 3.4), we found a combination of these two non-dimensional parameters that adequately describes the efficiency of a barrier: the probability of earthquakes breaking through the barrier is systematically related to the following “barrier efficiency index” λ (Fig. 3.4c):

$$\lambda = \frac{G_c}{G_{oi}} T^m \quad \text{where } m \text{ and } n \text{ are constants.}$$

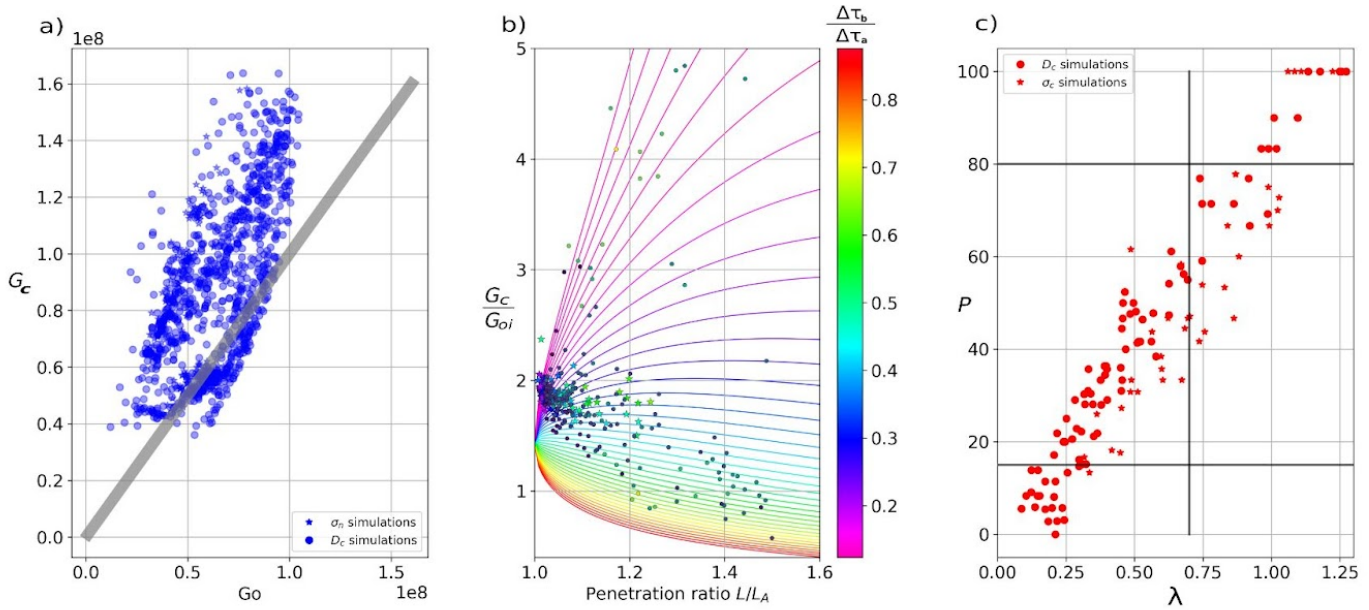


Figure 3.4: Rupture arrest conditions and barrier efficiency based on fracture mechanics. (a) Fracture energy (G_c , equation 3 in Methods 3.2) and energy release rate (G_o , equation 4 in Methods 3.2) numerically evaluated at the final rupture tip of earthquakes that stop at barriers defined by high D_c (stars) and by high σ_n (dots). For reference, the solid gray line shows a 1:1 relation. In most cases, the rupture arrest condition $G_c \geq G_o$ is verified. (b) Ratio between the fracture energy of the barrier (G_c) and the static energy release rate of the asperity rupture (G_{oi}) as a function of total rupture length (L) normalized by the asperity length (L_A), for all the events that stopped within the barrier. Dots are simulation results, with G_c measured using equation 3 at the end of the rupture and G_{oi} evaluated using equation 4 at the end of the asperity. Curves are theoretical estimates of G_c/G_{oi} (equation 12 in Methods 3.3), assuming different values of the ratio of barrier stress drop to asperity stress drop (see legend). (c) Barrier efficiency: probability P of earthquakes crossing the barrier as a function of a dimensionless number λ that encapsulates the effects of energy ratio and stress drop ratio, for barriers defined by a contrast of D_c (circles) and σ_n (stars). Thick horizontal gray lines separate ephemeral ($P > 80\%$), temporary ($15\% < P < 80\%$) and permanent ($P < 15\%$) barrier types. The vertical gray line shows the transition from ephemeral to permanent barriers as a function of λ .

Barriers behave mostly as permanent barriers if $\lambda < 0.3$, as frequent barriers if $\lambda \sim 0.7$, and as ephemeral barriers if $\lambda > 1$. We further developed an adequate approximation of λ based on model input parameters, namely normal stress, barrier frictional properties and barrier size (Supplementary material (See Appendix A2)).

To demonstrate how our model results could be used to evaluate the efficiency of fault barriers in nature, we propose an estimator of λ based on quantities that can be

constrained by observations, in particular by ISC distributions inferred from geodetic data (Supplementary material (See Appendix A2)). We illustrate the proposed approach by evaluating the efficiency of the Arauco barrier in the Chilean subduction zone, around the southern end of the 2010 Mw 8.8 Maule earthquake rupture (Molina et al., 2021). Considering the interseismic period between the 1835 South Chile and 2010 Maule earthquakes, we estimate $\lambda = 0.23$ for the Arauco barrier (Supplementary material (See Appendix A2)), which indicates a permanent barrier. Notably, the Arauco barrier has persistently stopped ruptures in historical and prehistoric records (Melnick et al., 2009, Philiposian and Meltzner, 2020; Molina et al., 2021).

3.4 Discussion

3.4.1 Interseismic coupling pattern on VW barriers

Our results show that areas of high and low ISC do not necessarily correspond to asperities and barriers, respectively, challenging a common interpretation of geodetic observations (Wang and Bilek, 2014). The reported ISC, inferred from an observation window much shorter than an entire seismic cycle, is not necessarily representative of the long-term behavior. Our simulations spanning multiple earthquake cycles support the idea that ISC can be time-dependent despite fault mechanical properties being constant, owing to slow slip transients and extended afterslip (Meltzner et al., 2015; Tsang et al., 2015a).

Remarkably, the long-term ISC (equation 21 in Methods 3.7) in most of our simulations is high (ISC > 0.9), both in permanent and frequent barriers [Extended Data Fig. 3 (See Appendix A2)]. When the low ISC of a barrier is a transient feature, subsequent locking can lead to increased seismic hazard. Conversely, areas with high or intermediate ISC are not necessarily asperities, as elevated ISC can also happen on barriers in our models. The three broad persistent barriers globally identified by Philiposian and Meltzner (2020), two in Chile and one in Mentawai, Sumatra, have intermediate to high ISC (Moreno et al., 2010, Prawirodirdjo et al., 2010). Our models indicate that such natural barriers with very high ISC might arise from lateral heterogeneities of D_c or σ_n within a VW fault: permanent VW barriers

($P < 15\%$) feature $ISC > 0.95$ [Extended Data Fig. 3 (See Appendix A2)], in contrast with the lower values ($ISC < 0.85$) produced by permanent VS barriers (fig. 4 of Kaneko et al., 2010).

Barriers and asperities have been widely associated with VS and VW fault areas, respectively (Kaneko et al., 2010, Barbot et al., 2012, Wei and Shi, 2020; Lambert and Lapusta, 2021). Further research efforts should aim at assessing if the segmentation of subduction zones is primarily driven by heterogeneities of VW materials and therefore re-evaluating the common assumption that barriers are VS areas.

3.4.2 Implications for structural control on earthquake behavior

Several observations suggest that geological structures of upper and lower plates may control the distribution of asperities and barriers along subduction zones (Bassett & Watts, 2015a, 2015b; Wang & Bilek, 2014; Li & Liu, 2017; Molina et al., 2021). For instance, many rupture areas tend to overlap with morphological features such as peninsulas and crustal faults (Collot et al., 2004; Melnick et al., 2009; Saillard et al., 2017; Molina et al., 2021). One possible explanation is that tectonic features affect the distribution of strength of the megathrust, which in turn affects seismicity patterns. Properties controlling fault strength include normal stress and critical slip distance which, as shown in our analysis, modulate barrier efficiency via their effect on the ratios G_c/G_{oi} and $\Delta T_b/\Delta T_a$.

Linking these findings with geological features can give insights on barrier behavior in nature, for instance recognizing that areas with intermediate values of σ_n can promote earthquake arrest. Density heterogeneities in the upper plate are an important source of lateral variations of σ_n along megathrusts (Li and Liu, 2017; Tassara, 2010; Molina et al., 2021). By analyzing gravity anomalies (Molina et al., 2021) it has been proposed that the Arauco barrier in Chile has higher σ_n than surrounding areas. In the Arauco barrier prehistoric and historic earthquake ruptures coming from north and south overlap, driving the zone to participate in coseismic slip (Moreno et al., 2010; Ojeda et al., 2020), which is consistent with both the

description of permanent barrier found in our work (Supplementary material (See Appendix A2)) and with our simulations showing large coseismic slip on CVWP with increased σ_n .

On the other hand, there is yet no clear path to infer D_c at natural scales from geological features. In nature D_c can depend on thermally activated dynamic weakening processes (Brantut, 2020; 2005; Rice, 2006; Onhaka, 2003), fault roughness, gouge thickness and σ_n (Marone et al., 1998, Brantut et al., 2008), and fluid content in the fault zone (Blanpied et al., 1998). Some of these factors might be linked to identifiable subducted seafloor features that contribute to fault roughness and supply wet sediments to the subduction channel (Bassett and Watts, 2015a), thus inducing lateral variations in D_c . Indeed, barriers usually coincide with subducting seamount chains, fracture zones or aseismic ridges (Contreras and Carrizo, 2011; Sparkes et al., 2010; Bassett and Watts, 2015a). Seismicity observed at the flanks of aseismic ridges (Bassett and Watts, 2015a), where a more pronounced megathrust roughness could induce larger D_c , is consistent with small earthquakes nucleating often at the edge of barriers with high D_c in our simulations.

Our study supports that geological characteristics of subducting and overriding plates can impact fault behavior. It also advances physics-based seismic hazard assessment by providing a theoretical framework to use future understandings of how geological structures modulate the spatial distribution of properties controlling fault strength, such as D_c and σ_n , and to anticipate the efficiency of natural fault barriers.

3.5 Methods

3.5.1 Earthquake cycle model setup

We consider a fault governed by the RSF law with the aging law for the state evolution:

$$\frac{\tau}{\sigma_n} = \mu^* + a \ln\left(\frac{V}{V^*}\right) + b \ln\left(\frac{V\theta}{D_c}\right) \quad (1)$$

$$\frac{d\theta}{dt} = 1 - \frac{V\theta}{D_c} \quad (2)$$

Here τ and σ_n are the frictional strength and normal stress on the fault, respectively, V the sliding velocity and θ a state variable, μ^* and V^* are reference values for friction and velocity, respectively, D_c is a critical slip distance for state evolution, and a and b are positive coefficients controlling the velocity and state effects, respectively. The difference $(a - b)$ defines the frictional regime on the fault. If $a - b > 0$, the steady-state friction is Velocity-Strengthening (VS): slip acceleration strengthens the fault, which inhibits earthquake nucleation and propagation, therefore promoting stable slip. If $a - b < 0$, steady-state friction is Velocity-Weakening (VW): friction drops if slip accelerates, promoting unstable slip leading to earthquake nucleation and rupture propagation. Simulations considering the RSF capture spontaneously all the stages of the seismic cycle, including interseismic coupling, nucleation, coseismic ruptures, postseismic afterslip and slow slip transients.

The fault is periodic along strike, deformation is purely dip-slip (antiplane), and frictional properties and normal stress are spatially variable along strike. The fault is embedded in an elastic, linear and isotropic medium and it is loaded by uniform steady slip beyond a width $W_{2.5}$ (see Methods 3.5). We capture the essence of the 3D fault problem while keeping the computations affordable by doing 2.5D simulations: we model a 1D fault in a 2D elastic medium with modifications of the

static stress transfer kernel that incorporate approximately the effect of a finite seismogenic width (see Methods 3.5). We set model parameters to typical values coming from geophysical observations. The imposed frictional width is $W_{2.5} = 1000 \text{ km}$, implying a real seismogenic width of $W = 200 \text{ km}$. We set the elastic shear modulus $\mu = 30 \text{ GPa}$, plate velocity $V_{pl} = 1.5 \times 10^9 \text{ m/s}$ (also set as the reference velocity V^*), asperity normal stress $\sigma_n = 95 \text{ MPa}$ and asperity critical distance $D_c = 1 \times 10^{-1} \text{ m}$. On the central section, σ_n and D_c are systematically varied.

We considered an elementary subduction zone model with two VW asperities separated by a central VW section with different σ_n and D_c . The two asperities have a fixed length $L_A = 70 \text{ km}$ and the central section length is varied from $L_B = 20$ to 60 km (Fig. 3.1). Along the whole fault, $b = 0.019$. Most of the fault is VW ($a - b < 0$), with $a = 0.015$ on the asperities and $a = 0.017$ on the central patch, except for two VS zones ($a - b > 0$) at the outer ends of the asperities of length $L_{vs} = 40 \text{ km}$ and $a = 0.032$. The ratio between segment length and the nucleation length L_∞ defined by Rubin and Ampuero (2005) is $L_A/L_\infty \sim 6.4$ for the asperities. In the CVWP, the ratio L_B/L_∞ varies according to L_B , σ_n and D_c . For the shortest CVWP considered here ($L_B = 20 \text{ km}$), it ranges from 0.45 to 1.8.

We first ran reference simulations spanning 10 kyrs, assuming uniform σ_n and D_c , and varying only L_B . No barrier for earthquake propagation is observed and the ruptures break the whole fault, except for $L_B \geq 45 \text{ km}$, where a couple of events stop within the central VW patch (Extended Data Fig. 4 (See Appendix A2)). We then performed one set of simulations varying D_c between 0.1 and 0.4 m and another set varying σ_n between 95 and 400 MPa. Although in laboratory experiments D_c is on the order of 10^{-5} to 10^{-3} m (Dieterich, 1979; Ohnaka, 1992) or from a few hundred micrometers to a few centimeters (Brantut et al., 2008), seismologically inferred

values of D_c are of order 1 to 10 m (Fukuyama et al., 2003). Thus we believe that D_c values used in our simulations are plausible.

We employ the QDYN software, which simulates earthquake cycles under the quasi-dynamic approximation and using adaptive time-stepping. Simulations span 9 kyrs in models with σ_n contrast and 10 kyrs in models with D_c contrast. The grid cell size Δx ranges from 117 to 136 m. The ratio between the process zone size L_b (Rubin and Ampuero, 2005) and grid cell size is $\frac{L_b}{\Delta x} \sim 14$ in the asperities and up to ~ 48 in the barrier, providing sufficient numerical resolution (Perfettini and Ampuero, 2008). The number of elements on the fault is 2048 in all the simulations.

3.5.2. Energy balance for earthquakes

Linear Elastic Fracture Mechanics (LEFM) provides a theoretical framework to study rupture propagation and arrest. Whether an earthquake can break through a barrier depends on the balance between the mechanical energy available in the incoming rupture (its static energy release rate G_o) and the energy dissipated by slip in the barrier (the fracture energy G_c). Earthquakes propagate if $G_o \geq G_c$; otherwise they stop. In order to prove that this energy condition is satisfied in our simulations, for those earthquakes stopping on the central VW patch we compute G_c and G_o as:

$$G_c = \int_0^{\delta u} (\tau - \tau_o) du \quad (3)$$

where τ is the fault shear stress as a function of slip and τ_o to the residual stress at the final slip, and

$$G_o = \frac{K_o^2}{2\mu} \quad (4)$$

where K_o is the stress intensity factor. For a rupture located between $x = 0$ and $x = l$, K_o is computed by a weighted integral of the spatial distribution of stress drop $\Delta\tau(x)$ as (Rice 1980)

$$K_o = \sqrt{\frac{a}{\pi}} \int_0^{2a} \Delta\tau \left[\frac{1}{\sqrt{a^2 - (x-a)^2}} + \frac{x-a}{a\sqrt{a^2 - (x-a)^2}} \right] dx \quad (5)$$

where $a = l/2$. The weight function gives a larger contribution to the stress drop in areas located close to the rupture front.

To obtain more insights on the parameters controlling earthquake arrest in the central VW barrier, we approximate G_o by assuming uniform stress drop in the asperity, $\Delta\tau_a$, and in the barrier, $\Delta\tau_b$. Then, denoting l_o the asperity length, equation 5 becomes

$$K_o = \sqrt{\frac{a}{\pi}} \int_0^{l_o} \Delta\tau_a \left[\frac{1}{\sqrt{1 - (\frac{x-a}{a})^2}} + \frac{x-a}{a\sqrt{1 - (\frac{x-a}{a})^2}} \right] dx/a + \sqrt{\frac{a}{\pi}} \int_{l_o}^l \Delta\tau_b \left[\frac{1}{\sqrt{1 - (\frac{x-a}{a})^2}} + \frac{x-a}{a\sqrt{1 - (\frac{x-a}{a})^2}} \right] dx/a \quad (6)$$

Using $\int \frac{dn}{\sqrt{1-n^2}} = \arcsin(n) + c$ and $\int \frac{n dn}{\sqrt{1-n^2}} = -\cos[\arcsin(n)] + c$,

$$K_o = \sqrt{\frac{a}{\pi}} \left[\Delta\tau_a \left[\arcsin\left(\frac{x-a}{a}\right) \Big|_0^{l_o} - \cos\left(\arcsin\left(\frac{x-a}{a}\right)\right) \Big|_0^{l_o} \right] + \Delta\tau_b \left[\arcsin\left(\frac{x-a}{a}\right) \Big|_{l_o}^l - \cos\left(\arcsin\left(\frac{x-a}{a}\right)\right) \Big|_{l_o}^l \right] \right] \quad (7)$$

$$K_o = \sqrt{\frac{a}{\pi}} \left[\left(\arcsin\left(\frac{l_o-a}{a}\right) - \arcsin(-1) - \cos\left(\arcsin\left(\frac{l_o-a}{a}\right)\right) + \cos\left(\arcsin(-1)\right) \right) \Delta\tau_a + \left(\arcsin(1) - \arcsin\left(\frac{l_o-a}{a}\right) - \cos\left(\arcsin(1)\right) + \cos\left(\arcsin\left(\frac{l_o-a}{a}\right)\right) \right) \Delta\tau_b \right] \quad (8)$$

$$K_o = \sqrt{\frac{a}{\pi}} \left[\left(\arcsin\left(\frac{l_o-a}{a}\right) - \cos\left(\arcsin\left(\frac{l_o-a}{a}\right)\right) \right) (\Delta\tau_a - \Delta\tau_b) + \frac{\pi}{2} (\Delta\tau_a + \Delta\tau_b) \right] \quad (9)$$

Finally, the static energy release rate is

$$G_o = \frac{\frac{a}{\pi} \left[\left(\arcsin\left(\frac{l_o-a}{a}\right) - \cos\left(\arcsin\left(\frac{l_o-a}{a}\right)\right) \right) (\Delta\tau_a - \Delta\tau_b) + \frac{\pi}{2} (\Delta\tau_a + \Delta\tau_b) \right]^2}{2\mu} \quad (10)$$

For reference, we denote as G_{oi} the static energy release rate of a rupture that breaks only the asperity ($l = l_o$):

$$G_{oi} = \frac{\pi l_o \Delta\tau_a^2}{4\mu} \quad (11)$$

3.5.3. Barrier efficiency λ

We construct a dimensionless parameter to quantify the resistance of the VW patch to earthquake propagation. Using equations 10 and 11 and defining the barrier-to-asperity stress drop ratio $T = \frac{\Delta\tau_b}{\Delta\tau_a}$,

$$G_o/G_{oi} = \frac{l}{\pi^2 l_o} \left[\arcsin\left(\frac{2l_o}{l} - 1\right) - \cos\left(\arcsin\left(\frac{2l_o}{l} - 1\right)\right)(1 - T) + \frac{\pi}{2}(1 + T) \right]^2 \quad (12)$$

We define an energy ratio

$$\Gamma = G_c/G_0 = G_c/G_{oi} \frac{\pi^2 l_o/l}{\left[\arcsin\left(\frac{2l_o}{l} - 1\right) - \cos\left(\arcsin\left(\frac{2l_o}{l} - 1\right)\right)(1 - T) + \frac{\pi}{2}(1 + T) \right]^2} \quad (13)$$

The equilibrium condition $\Gamma = 1$ gives a non-dimensional equation of the form

$$f\left(\frac{l}{l_o}, T, \frac{G_c}{G_{oi}}\right) = 0, \quad (14)$$

Thus the normalized rupture arrest length $\frac{l}{l_o}$ is controlled by the energy ratio $\frac{G_c}{G_{oi}}$ and the stress drop ratio T :

$$\frac{l}{l_o} = g\left(\frac{G_c}{G_{oi}}, T\right) \quad (15)$$

This particular example suggests that the resistance of a barrier to rupture penetration in general depends on the two non-dimensional parameters $\frac{G_c}{G_{oi}}$ and T . A closed-form expression of equation 15 cannot be obtained for an arbitrary distribution of stress drop. To find the best mathematical expression explaining our results, we assumed that resistance of the barrier can be obtained as a multiplication between $\frac{G_c}{G_{oi}}$ and T , leading to

$$\lambda_i = \frac{G_c}{G_{oi}} T^n \quad (16)$$

We then calculated different forms of λ_i varying m and n . For each combination, we fit the data with a linear polynomial form and obtained its residual. Afterwards, we choose the λ_i exhibiting the minor residual. Finally, we found that m and n are -0.9 and 0.76 respectively, allowing the definition of the “” barrier efficiency index” as;

$$\lambda_i = \frac{G_c}{G_{oi}} T^{0.76} \quad (17)$$

3.5.4. Constructing λ

The barrier efficiency index λ depends on the static energy release rate of the asperity, G_{oi} , which we measured in our simulations for all the ruptures arresting in the VW barrier by evaluating equations 4 and 5 when the rupture reaches the end of the asperity, at a rupture length of l_o . Three types of earthquake behavior are considered. For events that stop immediately when the rupture encounters the barrier, we measure G_c and G_{o1} at the rupture end. For earthquakes that penetrate the barrier and stop within it, G_o is again measured at the end of the asperity (G_{o2}), but G_c at the end of the rupture. For the events that break the whole barrier and propagate into the neighboring asperity, G_c is computed when the rupture reaches the end of the barrier and G_o in the asperity-barrier limit (G_{o3}). Finally, a single

averaged value of G_{oi} is obtained considering all the values previously calculated (G_{o1}, G_{o2}, G_{o3}) while the same is done for G_c .

We also measure in each rupture the mean stress drop in the asperity and in the barrier. Then, we average these values among all the events, to estimate a mean value for asperities ($\Delta\tau_a$) and barrier ($\Delta\tau_b$) in each cycle simulation. Once we have calculated $\frac{G_c}{G_{oi}}$, $\Delta\tau_b$ and $\Delta\tau_a$ for each simulation, we compute λ using equation 17.

3.5.5. Calibration of effective rupture width in the 2.5D model

We have performed 2.5D models on QDYN which approximately includes the seismogenic width effect while maintaining low computational costs. The 2.5D model approximates the depth-profile of slip as a half-sinusoid across the seismogenic width W . The slip in 2.5D models corresponds to the peak slip at the middle of the seismogenic depth of a 3D model. However, since the sinusoid approximations is crude, the effective width $W_{2.5}$ used as input in QDYN differs from the real W . In this section we calibrate the relation between $W_{2.5}$ and W , by determining the ratio $W_{2.5}/W$ such that the maximum slip D_{max} of a very long rupture with uniform stress drop $\Delta\tau$ is the same in both 2.5D and 3D models. In the 2.5 model, the stress transfer kernel $K(k) = \frac{\Delta\tau(k)}{D(k)}$ as a function of the spatial wavenumber k is given in equation A.24 of Luo and Ampuero (2018). For very long wavelengths ($k = 0$) it is $K = \pi \frac{\mu}{W_{2.5}}$. Thus we have the following relation $D_{max} = \frac{1}{\pi} \frac{\Delta\tau W_{2.5}}{\mu}$, which is verified numerically. In the 3D model, the peak slip of a very long dip-slip rupture is that of a mode II crack in 2D (vertical cross-section plane). From Dieterich (1992), $D_{max} = \frac{C \Delta\tau W}{\mu}$, where $C = 1.5$ if the Poisson's ratio is $\nu = \frac{1}{4}$. For arbitrary values of ν , we infer that $C = 2(1 - \nu)$. Equating the 2.5D and 3D expressions of D_{max} , we obtain

$$W_{2.5} = 2\pi(1 - \nu)W \quad (18)$$

For a Poisson's ratio of $\nu = \frac{1}{4}$, we get

$$W_{2.5}/W \approx 4.7 \quad (19)$$

Therefore, the $W_{2.5}$ input of QDYN is larger than the real seismogenic width W by a factor of about 5.

3.5.6. Slip rates thresholds defining slip behaviors

We define different types of slip behavior for the barrier based mainly on slip rate thresholds. We say that a point on the barrier experiences seismic slip when its slip rate exceeds 1 cm/s. Aseismic slip (transients) is distinguished between “rapid creep”, at slip rates $> 10^{-6}$ m/s, and “slow creep” otherwise. We say the fault is “strongly locked” when slip velocities are less than 10^{-10} m/s, well below the assumed plate velocity 1.5×10^{-9} m/s. We exclude strongly locked periods when analyzing seismic and aseismic slip distributions [Fig. 3.3c]. The aseismic/seismic slip ratios shown in figure 3.3 are the ratios between seismic slip and aseismic slip portions, and those in figure extended data 1 (See Appendix A2) are ratios between rapid-slow creep and the total accumulated slip. If this ratio increases, the amount of aseismic slip hosted by the barrier increases too.

3.5.7. Interseismic coupling (ISC)

The instantaneous value of interseismic coupling (ISC) is defined here as the fraction of slip deficit rate accommodated by stable creep:

$$ISC(x, t) = 1 - \frac{V(x, t)}{V_{pl}} \quad (20)$$

where V is the slip rate and V_{pl} the long-term slip velocity imposed by plate convergence. The instantaneous $ISC(x, t)$ varies throughout a seismic cycle. We can compute it at all times and at all fault points in our simulations, but we only show it in areas with meaningful values such that $ISC > 0$ ($V < V_{pl}$).

The long-term ISC is calculated at any point on the fault, following Kaneko et al. (2010), as

$$ISC(x) = 1 - \frac{\delta_{int}^{cum}(x)}{V_{pl} T_{int}^{cum}(x)} \quad (21)$$

where T_{int}^{cum} is the sum of the duration of all interseismic periods, defined as periods when $V < V_{pl}$, and δ is the slip accumulated over all the interseismic periods.

Acknowledgments

This work was partially funded by the National Agency for Research and Development (ANID)/Scholarship Program/DOCTORADO BECAS CHILE/2017—21171169. We also acknowledge partial support by the Millennium Scientific Initiative (ICM) of the Chilean government through grant NCN19_167 “Millennium Nucleus CYCLO The Seismic cycle along subduction zones”. We are also thankful to the Geoazur Seismes team which also partially funded the work.

References Chapter 3

The reference list cited in Chapter 3 is part of the **Thesis Reference** section at the pag 161.

4. Discussion

4.1 Frictional structure of the Chilean megathrust and earthquake segmentation

Through the application of the PCA to the gravity anomaly, interseismic locking and basal friction, we have been able to recognize different order segmentations along the Chilean margin. The different found segments are derived from the first mode given by the PCA tool, which explains 44% of the covariance between the proxies. Because the spatial extension of our segments correlates strongly with variation on seismicity and coseismic slip distribution along-strike (Fig. 2.7) and usually modes derived from PCA methods may involve a physical process related to the common spatial variance, we proposed that the first mode represents the first order frictional structure of the Chilean megathrust. From this, we define the first formal segmentation model of the Chilean margin that is based on geophysical inputs instead of rupture extent of earthquakes (Fig. 2.8). The segmentation model comprises unitary segments that are inferred as potential first-order-asperities whilst the boundaries between them are interpreted as seismic barriers.

4.1.1 Physical nature of asperities

The correlation between our segmentation model and seismicity distribution can give us insights on the underlying mechanisms affecting seismic patterns. Variations on seismicity distribution are mostly driven by different strength conditions which ultimately are modulated by the frictional regime on the fault. Observations support that the up-dip and down-dip limit of the seismogenic zone is characterized by the transition from stable to unstable sliding and vice versa, respectively (Pasten-Araya et al., 2022). Such observations are reflecting a segmentation across the megathrust mostly driven by the alternation between VW and VS materials (Wei et al., 2018) (Fig. 2.6). This mixture between VW and VS material has also been applied to explain along-strike fault seismicity patterns (Lui and Lapusta, 2016; Wei and Shi, 2020; Lambert and Lapusta, 2021). However, the presence of large VS areas extending across depth is not consistent with thermal control on friction; that is most rock-types found in the seismogenic zone (150°C-350°C) behave as VW material (Verberne et al., 2015, Hartog et al., 2012, Mitchell et al., 2016, Phillips et

al., 2019). Therefore, latitudinal variations on earthquake patterns are more likely caused by differences in the VW intensity within the seismogenic zone, specifically alternance between unstable regime and conditionally stable regime (equation 1.3). According to Chapter 2, this may explain the strong variation on seismic records when comparing the Central and Southern Andes segments. The former has been the nest for moderate-size earthquakes while the latter segment has been struck by giant ruptures. We suggest that the Central Andes in northern Chile is characterized by the distribution of very unstable asperities provoked by high normal stress. In contrast, negative gravity anomalies in the Southern Andes suggest a decrease in normal stress, favoring a conditionally stable regime. Numerical modeling supports the idea of huge earthquakes propagating through large conditionally stable areas (Hori and Miyazaki, 2011). Moreover, our interpretation of the conditionally stable regime governing the southern Andes must be taken as a first order characterization, since probably earthquake nucleation occurs on very unstable patches unmasked by their reduced size, but surrounded by large conditionally stable areas (Burgmann et al., 2005).

Alternatively, explaining seismic patterns variations could be done through the distribution of sediments on the subduction channel (Ruff et al., 1989). The thick sediments can determine the size of a rupture by regulating the smoothness of the plate interface (Muldashev and Sobolev, 2020). Interestingly, gravity anomalies have been shown to be useful to detect large sediment areas. For instance, a thick sediment layer on Japan's subduction channel has been confirmed by the presence of negative residual gravity (Nakata et al., 2021). Because fluids also will affect the medium density (and thus normal stress), a major presence of sediments with hydrated minerals should also cause a lower gravity signal. Hence, gravity anomalies segmentation could be also representing first-order hydrated sediment distribution causing different slip behavior (Nakata et al., 2021). Since the Southern Andes correlate with negative gravity anomalies, a strong load of wet sediments could be inferred in the subduction channel. The Valdivia and Maule segments are characterized by a more homogeneous and thick sediment layer due to the supply of wet sediments into the trench (Contreras-Reyes et al., 2010), leading then to small variation on stress distribution which provides conditions for propagation of large earthquakes (Ruff et al., 1989). Notably, the presence of wet sediments impact the

effective normal stress, which in turn controls frictional stability (equation 1.3). Within this context, hydrated sediments in the subduction channel can also promote conditionally stable behavior which is consistent with our previous discussions. Conversely, the Central Andes are characterized by a more starving sediment trench mainly because of the arid climate conditions and low energy to transport sediments from the continent to coast (von Huene and Ranero, 2003). The absence of wet sediments in the north of Chile might increase friction, thereby increasing shear stress. Certainly, large shear stress will favor some asperities to earthquake nucleation, but due to lack of a homogeneous thick sediment layer, these stresses are probably not homogeneously distributed. In addition, increased shear stress is not necessarily correlated with large ruptures (Muldashev and Sobolev, 2020). Stress heterogeneities provide unfavorable conditions for propagation of large earthquakes (Wang and Bilek, 2011). This is in agreement with seismic observations on northern Chile showing earthquakes of smaller magnitude and higher recurrence in comparison southwards 33°S (Comte et al., 1986, Dura et al., 2015).

4.1.2 Physical nature of barriers

Differences on the VW effect along strike might control the Chilean seismic segmentation by inducing changes on fault strength. Areas yielding a higher strength respect to surrounding zones will promote earthquake arrest, thus behaving as seismic barriers to rupture propagation. Within our segmentation model context (Fig. 2.8), the boundaries between the segments correspond to barriers. The master segments found for the Chilean margin (those are the maximum length rupture that can occur in a section fault (Philibosian and Meltzner, 2020)) are limited by permanent barriers. Moreover, inside master segments, unitary segments or asperities are found and they likely are delimited by temporal or frequent barriers (Fig. 2.8). Such variable behavior has been attributed to VS material mostly, provoking the fault to slip aseismically and inhibiting earthquake runaway (Kaneko et al., 2010). However, as mentioned before, it is very unlikely that VS behavior extends across all depth, therefore VW zones somehow might be causing earthquakes to stop. Indeed, VW areas have been shown to promote rupture arrest (Boatwright and Cocco, 1996, Hori and Miyazaki, 2011). The numerical simulations of Chapter 3, indicate that barriers can emerge from normal stress and frictional property heterogeneities inside a VW domain (Fig. 3.2). Our results show that VW patches

are capable of stopping earthquakes persistently and frequently. Therefore we infer that barriers, either temporary or persistent, found in the Chilean margin, are governed by a VW behavior, with a tendency towards the conditionally stable regime.

Persistent barriers in our simulations are driven by high RSF critical distance D_c contrast between barrier and asperity, implying that permanent barriers on the Chilean margin are possibly strongly linked to important latitudinal variations on D_c frictional parameter. On the other hand, our simulations show that frequent barriers are provoked by either intermediate values of D_c and σ_n . Hence, temporal barriers found on the Chilean margin are probable driven by intermediate σ_n and D_c contrast between barriers and adjacent seismogenic segments.

4.1.3 Fracture mechanics, implication on earthquake segmentation

In Chapter 3 we demonstrate that the barrier efficiency is enhanced by increasing its fracture energy G_c , which is proportional to D_c and σ_n . This explains why some fault sectors with high-intermediate values of D_c and σ_n favor earthquake arrest (Chapter 3). Accordingly, we infer that permanent barriers in the Chilean case are lying above megathrust zones presenting very high fracture energy G_c . Nevertheless, our results also indicate that static energy release rate of asperities G_{oi} adjacent to barriers also control the barrier efficiency via the energy ratio G_c/G_{oi} . Basically, if a rupture is more energetic when reaches the barrier (higher G_{oi}), the penetration distance within the barrier increases, which is measured with a lower G_c/G_{oi} . Applying this to the master segments previously described -which can be taken as seismogenic segments- we can infer that they might be often characterized by low values of G_{oi} inducing an increase on G_c/G_{oi} ratio and thereby preventing rupture propagation persistently, provoking seismic segmentation.

Further, the asperity elastic energy release rate is proportional to segment length, stress drop and inversely proportional to shear modulus (Chapter 3, equation 4). Since segment lengths are similar along-strike and stress drop has been shown to

be rather constant from global catalogs (Shaw et al., 2009), we can hypothesize that shear modulus could also contribute to control earthquake propagation. Shear modulus is thought to be directly related to rigidity of the surrounding elastic medium. Variations across depth on rigidity has been shown to control the coseismic slip distribution (Sallares and Ranero, 2019), thus it would be no surprising that high values of rigidity over master-segments cause an increase on G_c/G_{oi} , promoting the appearance of permanent barriers as well.

Additionally, the static energy release rate G_{oi} can be understood as the elastic energy stored during the interseismic period (G_{oi} is proportional to $\Delta\tau$, which is related to shear stress modulated by tectonic loading). Because some unitary segments are probably governed by conditionally stable behavior, the interseismic velocities could change from one cycle to other abruptly, which in turn would provoke a time-variable G_{oi} . From this, temporal barriers probably could be driven by a variable G_{oi} , shifting the barrier efficiency, favoring either earthquake arrest or runaway. Further, depending on stress loading history, sometimes G_{oi} will be large enough across several unitary asperities, promoting the synchronization of them in one single rupture inducing large earthquakes occurrence propagating along the entire master segment. This could explain the great variability of earthquake patterns shown in the southern Andes segments which is inferred to be governed by a conditionally stable regime.

On the other hand, the Central Andes presents a frictional regime very unstable, remaining probably no-time-variable if friction conditions do not change importantly, thus exhibiting a rather constant interseismic velocities between seismic cycles. This implies a not very time variable G_c/G_{oi} that is manifested by a less heterogeneous seismic pattern. Nevertheless, certainly larger events have occurred in the past (Easton et al., 2022). This for sure will require an increase on asperity elastic energy G_{oi} or decrease on barrier fracture energy G_c . Such change may be induced by the injection of fluids into the megathrust base, which can decrease normal stress (Moreno et al., 2014) and therefore G_c as well.

4.1.4 Seismogenic width effect on long ruptures

To gain more insights on earthquake segmentation, we theoretically investigated the effect of the seismogenic zone width W_{sz} on the physics of large or very elongated ruptures. Recent works propose that super-cycles on megathrust are strongly influenced by the seismogenic width (Herrendorfer et al., 2015, Muldashev and Sobolev, 2020). Numerical simulations show that for low values of W_{sz} , earthquakes are not able to break an entire fault segment (Weng and Yang 2017). In Chapter 3, it is shown that the energy release rate G_o is length-dependent (equation 11, Chapter 3). However, when the rupture has a length longer than the W_{sz} , G_o is shown to scale with W_{sz} (Marder et al., 1998, Weng-Ampuero, 2019, See Appendix A3). In Chapter 3 (Methods Chapter 3), we occupied $G_c \geq G_o$ as an arrest condition for earthquakes in our simulations, however this is not true for elongated ruptures. When W_{sz} is very small compared with rupture length l , the $G_c = G_o$ condition implies a steady state rupture (Weng and Ampuero, 2019). If $G_c > G_o$, the rupture will slow down during a certain distance before stopping. In the case of a rupture crossing a barrier, if energy release rate of the incoming rupture is similar to the barrier fracture energy it will propagate steadily a distance l_s (equation 16, See Appendix A3). If the barrier size is shorter than this distance l_s , the earthquake can easily propagate along the following asperity. For the case of permanent barriers found in our simulations, it can be noted that some percentage of earthquakes can traverse them. In nature, it could be that some persistent areas described as permanent barriers can host the propagation of some earthquakes because $G_c \simeq G_o$ at some stage of the cycle, explaining for instance why the 1730 metropolitan earthquake (Carvajal et al., 2017) was able to break the broad persistent barrier described in Chapter 2. We previously discussed some mechanisms involved in the decreasing/increasing of fracture energy or asperity energy release rate (e.g fluid injection at the megathrust base). Interestingly, l_s is proportional to the seismogenic width, implying that the rupture can propagate a higher distance with steady state velocity if W_{sz} increases. Notably, the seismogenic width has been shown to be proportional to the distance between the trench and the coastal line (Bejar-Pizarro et

al., 2013). Saillard et al., 2017 observed that the distance between the trench and the coast is higher in the Southern Andes than the Central Andes. Thereby we can assume that the averaged W_{sz} is wider in the Southern Andes, implying that some ruptures can easily propagate for some barriers in this segment, promoting the existence of very large ruptures (Fig. 4.1). Testing these statements will require the implementation of numerical modeling but considering fully dynamic simulations, since inertial forces are not well incorporated within quasi-dynamic simulations (QDYN), which are important to study the acceleration phase of earthquakes.

4.2 Relation between the frictional structure and geological features, implications on spatial and temporal persistence of seismic segmentation

We have seen that earthquake segmentation is strongly influenced by the frictional structure of the megathrust and energy quantities, therefore understanding the factors exerting control on it will certainly improve our knowledge about future earthquake patterns. This is important because the lack of registers concerning an entire seismic cycle do not provide enough time observational period to elucidate whether current earthquake segmentation is representative of long term behavior. Insights on temporal persistence of seismic segmentation may come from spatial correspondence between rupture extent of large earthquakes and tectonic features. Special attention has had the correlation of coseismic distribution along strike with gravity anomalies (Alvarez et al., 2014; Song and Simons, 2003). A first interpretation of this relation was made by Song and Simon (2003). They show that high coseismic slip patches lie beneath negative gravity anomalies zones. They proposed that negative gravity anomalies correspond to high friction areas, which in turn induce a high coupling state, dragging the fore-arc down and thus provoking a negative signature in gravity. Later, it was shown that both negative and positive gravity anomalies could be related to coseismic slip distribution (Basset and Watts, 2015a, 2015b). Tassara (2010) showed that gravity anomalies do not respond to changes in friction in the plate interface, rather they reflect large fore-arc density variation along the trench. Because density is directly related to the weight of the medium, it has an effect on the vertical stress above the megathrust base (Fig. 4.1). In Chapter 2, we observed that the peak of the friction PC was located where coseismic slip was maximum. In the case of gravity EOF, this also is maximized

where friction has a peak (Fig. 2.6). Following the suggestions by Song and Simons (2003), we could infer that low friction is dominant, which overturned our previous observation of friction peak. Because of this inconsistency, we support that gravity reflects changes on the density structure mostly of the overriding plate and not friction. Specifically, the changes evidenced by $\text{EOF}\Delta g$ along the trench are probably showing a link between the fore-arc density structure and spatial seismic segmentation, whose effects on frictional stability might be driven by normal stress variations (Fig. 4.1). Indeed, a first order density distribution obtained for the entire Chilean margin depicts a clear correlation with the first order seismic segmentation derived in Chapter 2 (Fig. 2.9). Assuming that the density structure of the fore arc is a long term feature, it implies that seismic segmentation should persist over geological time scale.

Remembering that recognized master segments derived from our PCA implementation are delimited by persistent seismic barriers, it is worth asking whether these discontinuities on segmentation are somehow modulated by the geological structure. In figure 2.9, the main oceanic features being subducted beneath the Southamerica plate are shown, together with first order crustal structure lying on the same plate. Six of the seven recognized persistent barriers are roughly correlated with seamount chains, fracture zones and aseismic ridges. Further, most of the worldwide persistent barriers reported by Philibosian and Meltzner (2020) are located where oceanic features subduct. Previous studies suggest that the presence of large seafloor anomalies enhance the normal stress, provoking an increment of coupling state (Scholz, 1997). Nonetheless, this is contradictory with the relatively low locking degree shown by geodetic observations in those areas (Wang and Bilek, 2014). Later, it was proposed that large positive bathymetric anomalies lying above the oceanic plate produce a flexural effect, which in turn generates more space to be occupied by wet sediments coming from the continent (Basset and Watts, 2015a). If these sediments subduct at very large depth, it is probably that its main effect is to decrease the fault strength and thus promote a low coupling signal. Nevertheless, a low locking degree is not always the case and some permanent barriers have experienced rather intermediate to high locking state (Moreno et al., 2010; Metois et al., 2016). This is in agreement with our numerical results showing that permanent barriers can indeed be characterized by intermediate and high coupling (Fig. 2.2f).

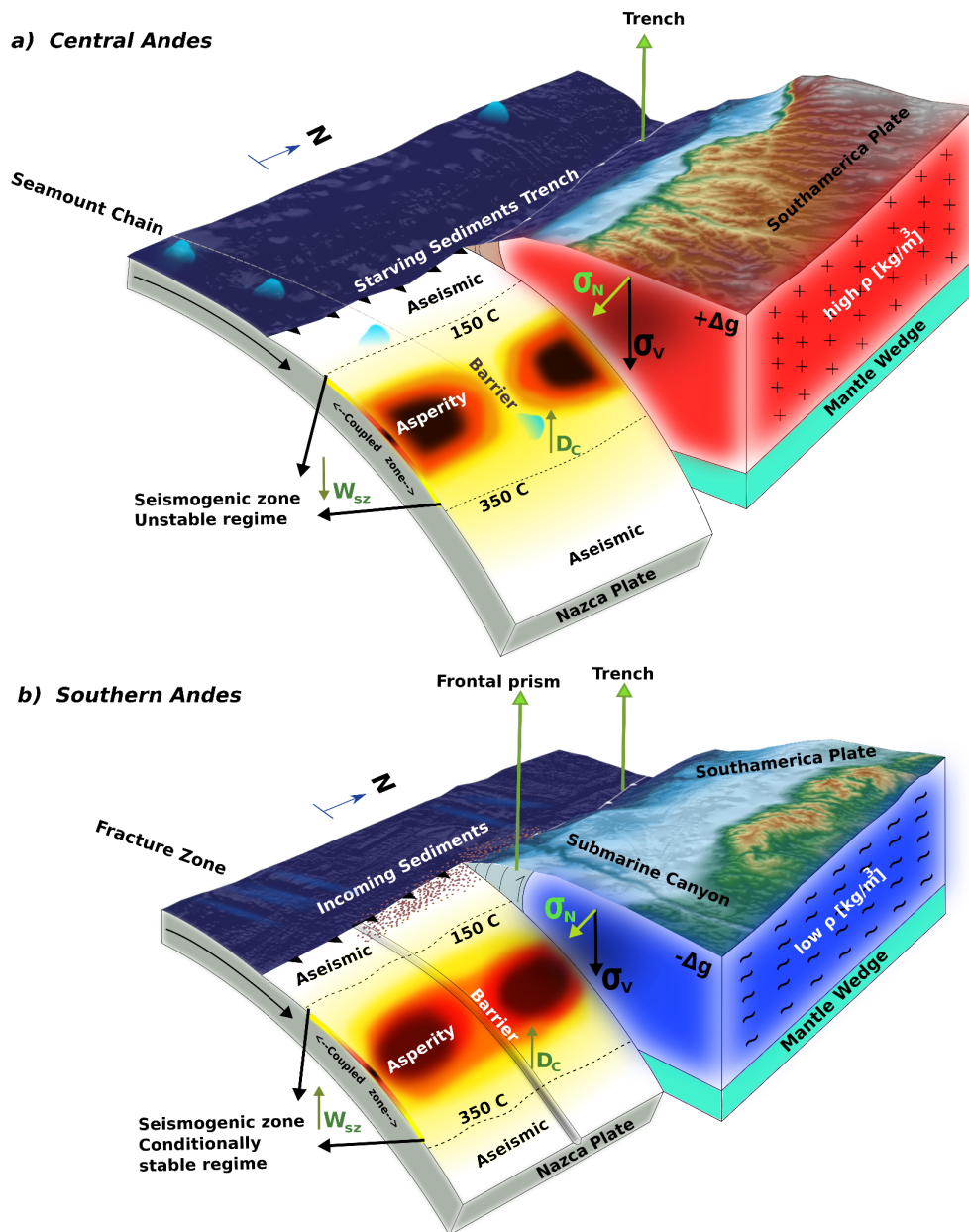


Figure 4.1 Seismotectonic illustration of Central and Southern Andes : Warm colors display the frictional structure which comprises seismic asperities and barriers. From dark to light the degree of coupling in the plate interface. On top, the topography and bathymetry taken from GEBCO_2019 grid.

a: Central Andes. Red color (positive gravity anomaly $+\Delta g$) in the overriding plate is related to an elevated density driven by an intrusive unit which ultimately increases the normal stress (vertical stress) above the seismogenic zone provoking a very unstable regime.

b: Southern Andes. The blue color (negative gravity anomaly $-\Delta g$) in the continental plate depicts a metamorphic unit which decreases density respect to the Central Andes, therefore decreasing normal stress and consequently favoring a conditionally stable regime. Note that the Southern Andes is characterized by a trench with sediment supply thanks to the humid climate. In contrast, because of the arid climate, the Central Andes has a starving sediment trench. The subduction of oceanic features enhance seafloor roughness, increasing D_c parameter and thus promoting the emergence of seismic barriers. Differences on the seismogenic width are displayed.

We previously mentioned that the most important parameter inhibiting earthquake propagation persistently is the RSF critical distance D_c . Studies suggest that D_c is proportional to seafloor roughness and fluid content in the fault (Marone et al., 1998; Blanpied et al., 1998). These fault properties can easily be linked to subducted seamount chains, aseismic ridges and fracture zones, which contribute to increase seafloor roughness and supply wet sediments to the subduction channel (Fig. 4.1). This may induce along-trench variation on D_c distribution, hence playing a role on the frictional structure and earthquake segmentation (Fig. 4.1). In addition, oceanic geological features are also long term structures. This implies that their effect on D_c parameters might be persistent, which is in agreement with permanent barriers description in Chile, supporting a long term characteristic seismic segmentation. However these statements must be carefully considered, since we mentioned that seismic cycles have been partially recorded and we cannot confidently ensure the existence of permanent barriers only from historical and instrumental data. That is, some permanent barriers actually might not be permanent and they might come from other mechanisms, for instance change on normal stress which promote temporal barriers.

Similarly, master segment boundaries also correlate spatially with the presence of crustal faults. In fact, for the Maule rupture area this observation is very clear and supports previous works suggesting an upper plate control on seismic behavior (Jara et al., 2015). Crustal faults can reflect important lateral discontinuities on density structure of the margin, therefore their existence might involve normal stress changes. Hence the presence of geological features of both plates probably control the value of frictional properties and normal stress which in turn may reinforce the effect on fracture energy and thus prevent earthquake propagation. Likewise, frequent barriers within the master segments also correlate with crustal faults and fracture zones. These structures probably increases D_c and σ_n but their values are not that high as it could be on permanent barriers, for instance because abundant sediments mask fracture zone roughness (Fig. 4.1). This prone the barrier to either stop or favor rupture propagation depending on the history of fault behavior (temporal barriers), provoking the megathrust seismic behavior to evolve more

randomly (e.g. creep episodes followed by coupling). This also can be defined as a slip pattern and it will persist over time due to its dependency with long term tectonic features.

Importantly, the interaction between megathrust seismic cycle and fore-arc deformation probably involve feedback processes, implying that frictional structure of the megathrust has also contributed to the current morphology of the Andes Cordillera and/or coastal Cordillera. Some authors have proposed that the rate-strengthening nature of some barriers prone the fault to creep mostly, trespassing anelastic deformation to the upper-plate inducing permanent deformation and thus construction of high peninsulas (Saillard et al., 2017). They argue that the alternance between very weakening asperities and stable zones driven by VS material can explain the permanent deformation observed along the Chilean margin. However, our results suggest that the seismogenic zone is laterally predominated by VW regime, implying that creep areas might not be the only factor playing a role on permanent deformation related to peninsulas. Accumulation of permanent deformation has also been shown to occur due to shortening on rupture area peripheria of large earthquakes above stick-slip segments (Rosenau et al., 2009). Whatever be the case behind permanent high uplift rate on the fore-arc, it seems to respond to variation on frictional structure of the megathrust, therefore also supporting the persistence of it over geological time scale.

4.3 Long and short term earthquake behavior at first order segmentation scale

Remembering that the northern Chilean margin has been described as possessing a very unstable frictional regime (attributed mostly to a denser upper plate) (Fig. 4.1), we could infer that coupling is rapidly enhanced after earthquakes, producing a decrease in their return period. This is in agreement with the predominant short observed earthquake recurrence time (~100 yrs) northwards 33°S (Nishenko, 1985). In consequence, the amount of moderate size earthquakes occurring on the Central Andes should show an opposite tendency simply because as recurrence time decreases, the number of earthquakes increases. In fact, in terms of solely seismicity of moderate-low magnitude, the north of Chile concentrates a major

number of nucleations compared with the south of the country, which is consistent with a predominant unstable frictional regime (Fig. 2.7). We believe then that this seismic pattern evidenced by current observations corresponds to the short-term behavior. Whether this seismic behavior can be extrapolated over geological time scale, needs the fault to maintain its frictional properties without important changes over several seismic cycles. Since we previously argued that geology exert a primary control on strength conditions, we can assume that short term earthquake behavior inferred on the Central Andes is representative of the long-term behavior as well. Certainly, the lack of large earthquakes records, similar to Valdivia 1960 or Maule 2010, does not guarantee that nucleation of huge earthquakes have not occurred in the past (Easton et al., 2022). As we said in previous sections, it could happen that multiple asperities fail on one single long rupture due to synchronization of stress build up or because frequent barriers may shift from arrest to favor rupture propagation. All these causes might be triggered by transient phenomena induced by fluid circulation or evolution of the system itself, which ultimately will change fault shear stress and thus enhance rupture propagation conditions. Further, although the nucleation of this type of event should be rare, the associated seismic risk could be underestimated in the area.

In contrast to the Central Andes, our results suggest that the frictional regime predominating the Southern Andes is mostly a conditionally stable regime (Fig. 4.1). This allow the megathrust to host an ample range of seismic patterns, which involve the fault to slip either seismically or aseismically. The presence of conditionally stable areas has been used as a necessary condition for the megathrust to be the nest of giant earthquakes, as for instance, the Tohoku 2011 event (Hori and Miyazaki, 2011). Hence, our results indicate that southwards 33°S, the Chilean margin meets the necessary conditions to participate in large earthquakes, which is evidenced by the recents Valdivia 1960 and Maule 2010 events. At the same time, the interseismic period on a fault section can dramatically change if the frictional regime is conditionally stable. Indeed, our simulation supports this, and they show that low locking in some sectors is a transient phenomena triggered by long-lived postseismic effects of past rupture (Fig. 2.2). A conditionally stable regime could prone a creeping fault section to lock abruptly, inducing variable interseismic locking which can increase seismic hazard, or vice-versa. This is in agreement with the

variable earthquake pattern displayed on the southern Andes, where we have the occurrence of moderate size earthquakes and also the nucleation of giant events. Therefore, this mixture of large and moderate size earthquakes striking the Southern Andes is an intrinsic characteristic of the zone, being a short-term quality of the margin. Likewise, the nature of conditionally stable behavior has been attributed to geological features of the system, suggesting that this behavior also represents long-term behavior. Surprisingly, our simulations indicate that variable seismic patterns do not necessarily obey to changes in strength conditions triggered by fluid injection or mineral dehydration, therefore persistent geological control is totally consistent with heterogeneous rupture patterns throughout time. Finally, in order to study deeply and quantitatively the seismic hazard for the Chilean margin, we dedicate the following entire section to it.

4.4 Implication (Application) on seismic potential

The size and temporal recurrence of earthquakes are one of the most important parameters to be considered in earthquake hazard. Predicting when the next earthquake will nucleate is one of the main interests in studies of the seismic potential of a given region. This is because megathrust earthquakes are one of the most devastating natural hazards in the world. In Chapter 2, the natural segmentation arised from the PCA methodology has a direct impact on multiple rupture scenarios that the Chilean margin can host. Integrating this model segmentation on probabilistic earthquake hazard and tsunami modeling could certainly improve the risk mitigation measurements developed in Chile so far. For instance, several tsunami scenarios can be modeled by considering as sources slip distributions along strike (Carvajal et al., 2017). From our model segmentation, several stochastic slip models can be built to construct possible earthquake rupture sequences and thereby investigate how tsunamis could vary. Further, the same work could be applied to explore under which conditions crustal faults could be re-activated, this via changes on Coulomb stress which depend on co-seismic slip distributions (Cortés-Aranda et al., 2021).

Whether several unitary segments identified in the Chilean margin will synchronize to trigger one single large rupture may depend on the nature of barriers delimiting such

sections. Considering LEFM, in Chapter 3 we have developed a robust theoretical analysis to derive a barrier efficiency parameter, that is to quantify the ability of barriers to prevent earthquake runaway. The λ parameter is proportional to the barrier fracture energy over the asperity static energy release rate G_c/G_{oi} and stress drop of the asperity over the one of the barrier $\frac{\Delta\tau_a}{\Delta\tau_b}$. λ was applied to our quasi-dynamic rupture modeling results and was successfully tested (Fig. 3.4c). By inspection of figure 3.4 c, it can be noted that permanent barriers are characterized by λ values < 0.3 while that ephemeral barriers correspond to $\lambda > \sim 1$. Otherwise, they behave as frequent or temporal. In order to obtain a parameter applicable to natural barriers, we have proposed an estimator of λ based on quantities that can be constrained by observations (See Appendix A2). To demonstrate that λ can be useful to predict the behavior of natural barriers, we apply it to the Arauco barrier located in the Southern Andes (See Appendix A2). Our analysis yields a predicted λ of 0.22 which indicates a permanent barrier. This is in agreement with our description of the Arauco peninsula as a persistent barrier. Therefore our work could be used to describe the behavior of natural barriers identified on our segmentation model, thereby supporting or invalidating our barrier description (Chapter 2, Fig. 2.8). Further, with a quantitative classification of the several barriers, we could assess the probability of them to inhibit rupture propagation. This can be integrated into the construction of a more constrained earthquake scenario needed to assess more confidently the seismic hazard associated in a specific area.

Improving even more hazard assessments on the Chilean margin could be done by estimating, for instance, the time return of the next earthquake hosted in some master segment described in Chapter 2. Here, Linear Elastic Fracture Mechanics (LEFM) takes a fundamental role, since it has been used to calculate the rupture potential (Φ) of large earthquakes, that is to anticipate the final size of a rupture (Weng and Ampuero 2020). The mathematical expression of Φ can be written as follows;

$$\Phi(L1, L2) = \int_{L_1}^{L_2} \frac{(1 - \frac{G_c}{G_{mix}}) dl}{W} \quad (4.1)$$

where G_c is the rupture fracture energy and G^{mix} corresponds to the energy release rate for a mixed-long rupture, that is considering oblique slip. W is defined as the seismogenic width and L_1 and L_2 the initial and final position of a fault segment. We say that a rupture will propagate over the entire segment $[L_1, L_2]$ when $\Phi(L1, L2) > 0$. Weng and Ampuero (2020) applied this equation to the Valdivia segment using scaling relation between the energy quantities and final slip, providing an alternative to calculate G_c/G_o , that is

$$G_c/G_o = BWD^{n-2}/C\mu \quad (4.2)$$

where B and C are constants, μ the shear modulus and D the final slip. Equation 4.1 and 4.2 predict that the fault needs to accumulate a critical slip deficit D^{crit} to host very long ruptures. Combining this with the slip deficit of a given segment, allows to estimate the largest possible size of an earthquake (Weng-Ampuero, 2020 (fig 4)).

Assessing whether the rupture will runaway or arrest once the earthquake nucleates will depend on where the runaway segment intersects with the rupture potential which is illustrated as the time-dependent evolution of the seismic segmentation (Weng and Ampuero, 2019). In order to estimate the rupture potential of the Chilean margin and thereby assessing the seismic hazard of master segments, we have applied this methodology considering interseismic locking. We must emphasize that we followed the same methodology carried out by Weng and Ampuero (2020) but considering a variable seismogenic width. The variable seismogenic width is obtained by considering the place where the interseismic locking is lower than 0.3 in the trench perpendicular direction.

We decided to calculate the rupture potential to three different zones in Chile, but with some overlapped areas which do not affect the results. First, we analyzed the rupture potential of the segment between 37° and 44° S, allowing a direct comparison with Weng-Ampuero 2020 who studied the same area. It can be observed from figure 4.2 that the elapsed time after the 1960 earthquake needed to occur for a similar event is ~350 years, which is in agreement with recurrence time

for the area (Cisterna et al., 2005). The main difference between our estimated time-dependent rupture potential and the one calculated by Weng-Ampuero 2020 is to move the rupture potential curve towards the left. This implies a shorter time return for a giant Valdivia earthquake type (Figure 4.2) with respect to the one obtained by Weng-Ampuero 2020. The shorter recurrence time come from the incorporation of a space variable seismogenic width, highlighting the relevance of W in earthquake dynamics and thus seismic hazards.

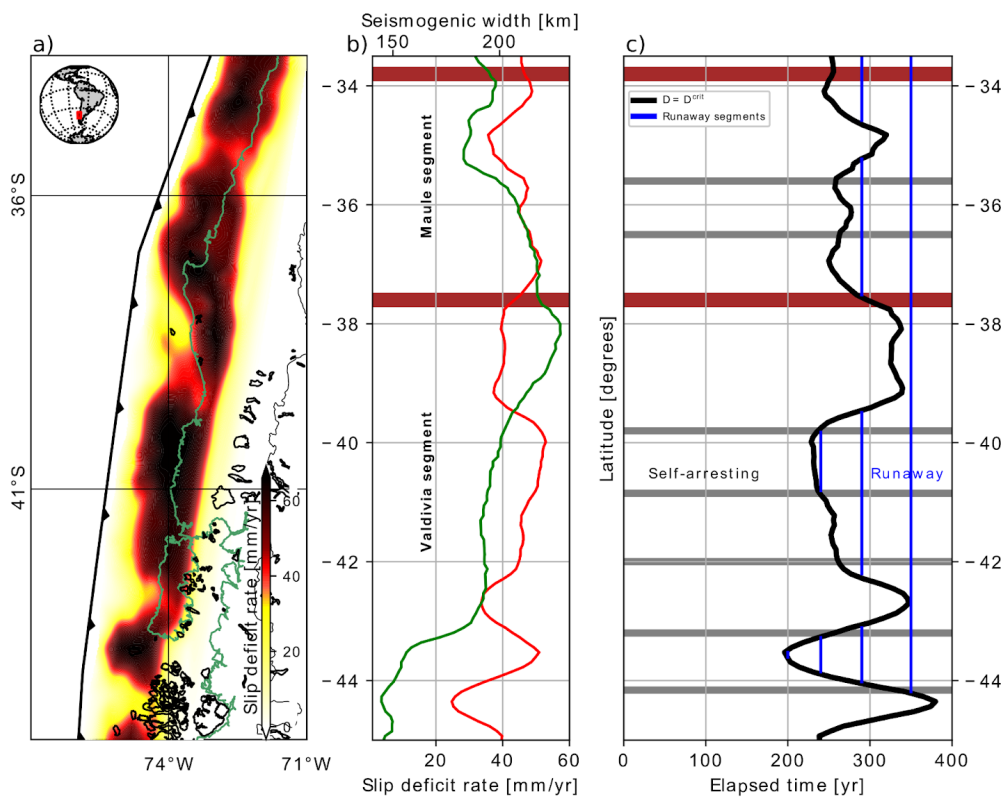


Figure 4.2 Time dependent seismic hazard assessment (Valdivia segment). **a** : Warm colors display the slip deficit rate for the Valdivia segment. Green lines depict the location of the seismogenic width, being variable along the trench. **b**: Red solid line represents the latitudinal averaged slip deficit rate. In green solid line the seismogenic width, being variable along the trench. **c**: Black thick line corresponds to the elapsed time required to the megathrust accumulate the critical slip favorable to large events occurring in the Chilean subduction zone. Blue vertical lines represent the possible size of earthquakes propagating across the margin. Intersections between blue and black line display the end of the possible rupture. Horizontal gray lines the urinary segment boundaries representing temporal barriers whereas thick brown horizontal lines depict the permanent barriers delimiting master segments reported in Chapter 2.

Now, the area between 19°S and 30°S presents a rupture potential much more variable than the Valdivia segment (Fig 4.2-Fig. 4.3). Likewise, the return time for a very long rupture seems to be shorter than the Southern Andes. Our results indicate that an earthquake similar to the one nucleated in 1877 in the Iquique segment with an estimated magnitude of 8.8 (Beck et al., 1998) could occur after ~250 years. Considering that since 1877 have transpired 143 years, we could suggest that the Iquique segment needs to accumulate more slip deficit to reach a critical slip and thus host a large event. Another important master segment that has not yet experienced the largest rupture is the Copiapo segment, which was the nest for the great 1922 M9.0 Caldera earthquake (Beck et al., 1998).

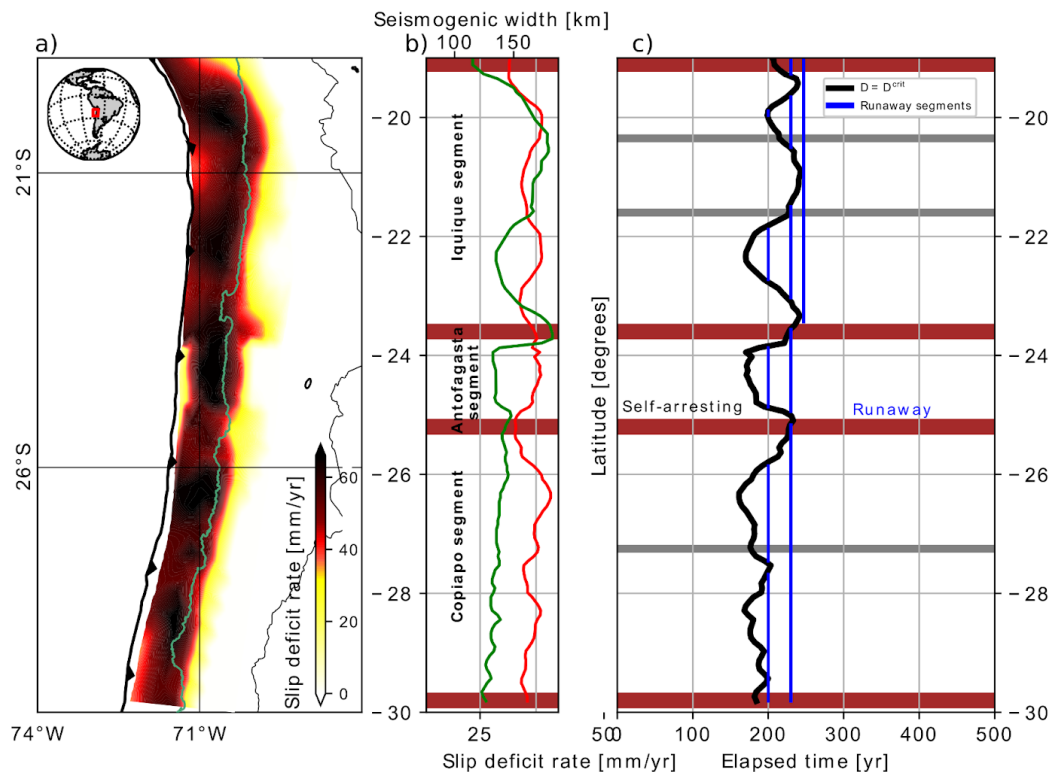


Figure 4.3 Time dependent seismic hazard assessment (Iquique, Antofagasta and Copiapo segments). a : Warm colors display the slip deficit rate for Iquique, Antofagasta and Copiapo segments. Green lines depict the location of the coast-line. b: Red solid line represents the latitudinal averaged slip deficit rate. In green solid line the seismogenic width, being variable along the trench. c: Black thick line corresponds to the elapsed time required to the megathrust accumulate the critical slip favorable to large events occurring in the Chilean subduction zone. Blue vertical lines represent the possible size of earthquakes propagating across the margin. Intersections between blue and black line display the end of the possible rupture. Horizontal gray lines the urinary segment boundaries representing temporal barriers whereas thick brown horizontal lines depict the permanent barriers delimiting master segments reported in Chapter 2.

Figure 4.4 shows that a runaway rupture breaking the same segment again could be possible after ~240 years, but within the following decades is an unlikely possibility since the elapsed time since that big event is only 88 years. Definitely this doesn't mean that earthquakes of moderate size can not occur in the near future. Certainly, one of the most anomalous events recognized thanks to historical records is the huge 1730 earthquake that broke a portion of the margin in the center of Chile (Valparaiso segment) between 30° and ~36° S, with a rupture area similar to the 1960 Valdivia earthquake and with an estimated magnitude of Mw9 (Carvajal et al., 2017; Ruiz and Madariaga, 2018). Such a large event seems to have crossed the only broad permanent barrier in Chile, being overlapped later by the 1751 earthquake, with a similar size towards south (Fig 2.8). Our results indicate that a return period for such a big event is approximately 280 year (Fig. 4.4). Incredible, since 1730 have already passed 290 years, suggesting then a probably similar rupture within the following decades. The impact on seismic hazards are important since over the area, most of the population is concentrated. Additionally such a big earthquake could cause a huge tsunami, generating a lot of damage on the most important harbors of the country. However, because this segment is located over a mix between unstable and conditionally stable frictional regime, locking pattern could abruptly vary, causing the stress build up change dramatically, accelerating the next big earthquake or delaying the nucleation phase. Additionally, historical evidence has supported that the predecessor of the 2010 Mw8.8 Maule earthquake was the one described by Darwin in 1835 (Melnick et al., 2012). Nevertheless, paleo tsunami records point out a smaller tsunami compared to the 2010 case (Ely et al., 2014), implying that probably 1835 did not break the Maule master segment entirely but only its southern portion (Ruiz and Madariaga, 2018). This leads to the 1751 event as a candidate for being the one big earthquake before Maule 2010. Further, rupture potential shows that the master segment would require ~300 years to experience a large rupture (Fig. 4.4). Remarkably, until 2010 the time since 1751 was 260 years, which is consistent with the amount of time necessary to the segment hosting a big earthquake again. Not surprisingly, the rupture potential has a latitudinal distribution that correlates with the unitary segments distribution exhibited in Chapter 2, providing clues on how important parameters may be modulating the seismic segmentation over Chilean margin. For instance, it can be noted in figure 4.4 that the rupture potential roughly coincides with the distribution of past ruptures, such 1837

and 1737 events, supporting previous works showing that these earthquakes probably do not break the same segment of 1960 event (Hocking et al., 2021). These findings suggest that rupture potential estimations could partially improve our understanding of the conditions auspicious to the master segments being able to host huge earthquakes. Also, gives insights on parameters controlling the seismic segmentation, which could be tested by applying this methodology to other similar regions. Finally, rupture potential helps to obtain recurrence time for large earthquakes, being this parameter essential to assess the earthquake potential across the Chilean subduction zone.

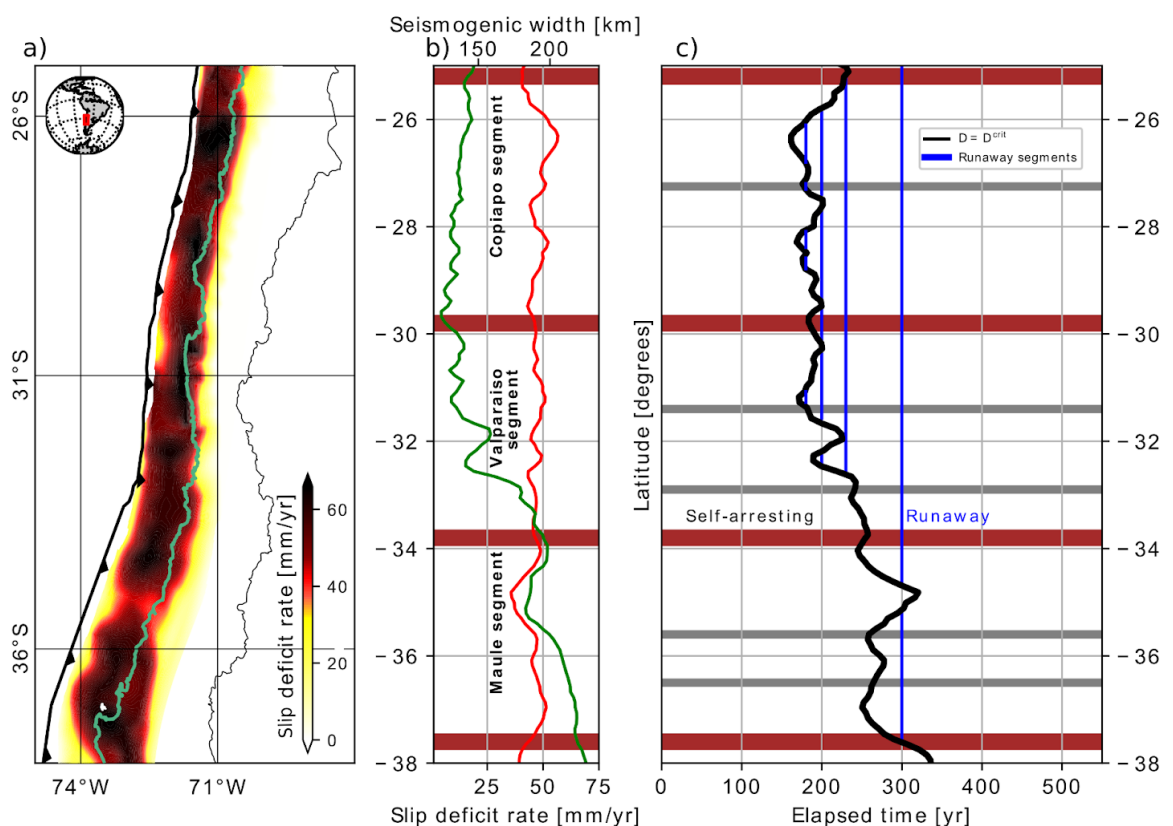


Figure 4.4 Time dependent seismic hazard assessment (Maule and Valparaíso segments). a : Warm colors display the slip deficit rate for Maule and Valparaíso segments. Green lines depict the location of the seismogenic width, being variable along the trench. **b:** Red solid line represents the latitudinal averaged slip deficit rate. In green solid line the seismogenic width, being variable along the trench. **c:** Black thick line corresponds to the elapsed time required to the megathrust accumulate the critical slip favorable to large events occurring in the Chilean subduction zone. Blue vertical lines represent the possible size of earthquakes propagating across the margin. Intersections between blue and black line display the end of the possible rupture. Horizontal gray lines the urinary segment boundaries representing temporal barriers whereas thick brown horizontal lines depict the permanent barriers delimiting master segments reported in Chapter 2.

5. Conclusions

The main aim of this thesis was to investigate the frictional structure of the Chilean megathrust and its link with the geological structure of both the upper and lower plates (Fig. 1.3).

The spatial correlation between the geophysical and geological proxies (gravity anomalies, interseismic locking and basal friction) with the seismicity distribution across the Chilean margin reveals the interplay between upper-lower plate properties and the megathrust frictional regime. In particular, the density structure of the fore arc inferred from gravity anomalies exhibits a marked segmentation along-strike, exerting control on the megathrust frictional stability through its effect on normal stress. Our results suggest that the Central Andes segment is characterized by a heavier forearc, promoting a very unstable regime whilst the Southern Andes comprises a less heavy fore-arc which in turns favor a conditionally stable regime. We proposed that these first order differences can explain why the Southern Andes seems to be the net of great earthquakes while in the Central Andes this type of event is rare. At minor scale ($10^2 km$), we identify unitary segments interpreted as potential seismic asperities delimited by seismic barriers. There is a spatial correspondence between the segments found and incoming oceanic features of the Nazca plate. Notably, most of the permanent barriers coincide with aseismic ridges and seamount chains, suggesting a tectonic control on earthquake segmentation along-strike.

The thermal control on friction suggests that the physical nature of seismic barriers should be VW material, and not VS as it has been commonly assumed. The numerical simulations of the seismic cycle demonstrate that lateral heterogeneities in σ_n and D_c parameters within a VW domain can promote earthquake arrest and thus act as seismic barriers. Further, the slip behavior hosted by the VW barriers is similar to that experienced by natural barriers, therefore they are better analogues than VS-barriers. Remarkably, our simulations show that VW barriers present intermediate-high ISC, which is a kinematic feature displayed by natural barriers along several subduction zones. Our research challenges the common interpretation of locked patches as strong seismic asperities and reformulates the way we

understand earthquake segmentation. Additionally, we conclude that the strong correlation between geology and earthquake patterns is caused by latitudinal variations of σ_n and D_c , the former modulated mostly by the fore-arc density structure and the latter controlled by seafloor roughness and water content in the subduction channel. Because these tectonic features are long term characteristics, its effect on the frictional structure should be persistent throughout several seismic cycles, supporting that the megathrust frictional structure prevails over time and thus seismic segmentation as well. Hence this thesis supports the hypothesis work announced in Chapter 1, providing insights on the mechanisms of earthquake arrest and fault segmentation.

On the other hand, results of Chapter 2 and 3 have strong implications on seismic hazard assessments. The segmentation derived from the PCA, enables the construction of the first formal segmentation of the Chilean margin based on geophysical/geological proxies instead of historical records of past earthquakes. This methodology offers an opportunity to constrain and create segmentation models on other subduction zones lacking seismic records. Consequently, the segmentation model can be used to constrain co-seismic slip scenarios to investigate the necessary conditions to trigger crustal fault reactivation and/or to model tsunami dynamics. Likewise, based on theoretical results (fracture mechanics), we create a non-dimensional parameter λ to quantitatively measure the barrier efficiency of natural barriers. We show how λ can be used to anticipate the barrier behavior on real faults. Therefore this thesis strongly improves and advances the theoretical underpinnings of physics-based hazard assessment. Furthermore, we estimate the rupture potential along the entire Chilean margin, providing some theoretical discussion about the time-dependent seismic risk of the different segments described in this work.

Finally, this contribution highlights the underlying mechanism behind earthquake segmentation combining multiple methodologies, providing a robust analysis tool that can be easily reproduced by those related to earthquake physics and seismic hazards. We hope that from the results discussed in this thesis, the science community will be benefited and inspired to pursue the hidden earthquake knowledge waiting to be discovered.

6. Appendix

6.1 (A1) Supplementary Material Chapter 1

Frictional Segmentation of the Chilean Megathrust From a Multivariate Analysis of Geophysical, Geological, and Geodetic Data

Diego Molina ^{1,2}, Andrés Tassara ^{1,2}, Rodrigo Abarca ³, Daniel Melnick ^{2,4}, and Andrea Madella ⁵

1 Departamento Ciencias de la Tierra, Facultad de Ciencias Químicas, Universidad de Concepción, Concepción, Chile,

2 Millennium Nucleus The Seismic Cycle Along Subduction Zones CYCLO, Valdivia, Chile,

3 Departamento de Geofísica, Facultad de Ciencias Físicas y Matemáticas, Universidad de Concepción, Concepción, Chile,

4 Instituto de Ciencias de la Tierra, TAQUACh, Universidad Austral de Chile, Valdivia, Chile,

5 Institut für Geowissenschaften, Universität Tübingen, Tübingen, Germany

Published on *Journal of Geophysical Research* on July 23th, 2020

Contents of this file

Introduction

Text S1

Table S1

Figure S1- Figure S2

Introduction

The files attached to this document are 1) an explanatory text describing the details of the Principal Component Analysis (PCA) method applied in this study, and 2) a table containing the vertices of unitary seismic segments identified by us. The data used for this work is fully available in open sources or previous papers.

Text S1.

Development and Implementation of Principal Component Analysis. Principal Component Analysis (PCA) uses an orthogonal transformation over observations of possible correlated variables in order to obtain a new set of coordinates of linearly uncorrelated variables that concentrate along their axes most of the covariance of the data. We follow the methodological approach of Venegas (2001) and her notation for the analysis of time series of a common time window that are associated with a set of different locations (meteorological stations in her case) distributed in space. In our case, instead of time series, we consider trench-perpendicular profiles of a common length that are distributed along the trench axis. We define a number M ($=120$) of trench-perpendicular profiles that are separated 20 km along the trench and ordered from north ($m=1$) to south ($m=M$). Each profile is formed by N ($=200$) points spaced 0.9 km and covering a length of 180 km from the trench axis in the west ($n=1$) to a point in the main Andean cordillera in the east ($n=N$). We arrange the M trench-perpendicular profiles as rows of a coordinate matrix P of dimensions $M \times N$. The construction of matrix P implies that we will focus on the along-trench variability of the major trench-perpendicular features contained in the data. Once the P matrix is constructed, we interpolated the value of each proxy (from grids computed as shown in section 3.2) at the (m,n) coordinates and created one data matrix D_p for

each of proxy p . Then, we centered and normalized each D_p matrix by subtracting the average value and dividing them by its standard deviation. This is a necessary step that ensures the spatial comparability of the different proxies (e.g. Venegas, 2001; Brethertone et al., 1992)

Our implementation of PCA can be applied to one individual proxy or combinations of them (i.e. Brethertone et al., 1992). These combinations are obtained by concatenation of the considered D_p matrices so that the final dimensions of the full data matrix D will be $C \times M \times N$ (or $CM \times N$ for simplicity), where C is the number of combined proxies. The next step is to obtain the covariance matrix of D , which by definition will be a square matrix of dimensions $CM \times CM$, and its respective eigenvectors E^k and eigenvalues λ_k . We refer to the k indexes as modes, which are ordered following the rank of their eigenvalues λ_k from the highest ($k=1$) to the lowest ($k=CN$). Commonly, only the first K modes are considered since they explain much of the covariance of the data (Venegas, 2001; Smith 2002). To quantify the amount of the variability explained by each mode k , it is useful to compute the percentage that the corresponding eigenvalue λ_k represents with respect to the total sum. Each mode k is associated with an eigenvector E^k (also called Empirical Orthogonal Functions EOFs) that in our case represents the along-trench variability of a particular trench-perpendicular characteristic pattern. For analyses that combine two or three proxies ($C > 1$), we split the eigenvectors to obtain one E^k for each proxy. Then we stack the first K EOFs in a matrix E_p for each proxy p that contains K column eigenvectors of length M (i.e. each matrix E_p has dimensions $M \times K$).

For each proxy, the trench-perpendicular variation of the K number of EOFs is obtained by projecting the data matrix D_p onto each eigenvector, which in matrix

notation can be written as $A_p = E_p^T * D_p$. Each matrix A_p has dimensions $K \times N$, since E_p^T (the transpose of E_p) is $K \times M$ and D_p is $M \times N$, and therefore A_p is independent of the number of trench-perpendicular profiles M . The rows of the A_p matrices are known as the Principal Components (PCs) of the data, each of them associated with a particular mode k , and provide information on the trench-perpendicular variability of the along-trench pattern informed by a given EOF. Finally, the actual spatial distribution of each proxy can be reconstructed by multiplying its matrix E_p (containing the K EOF columns of length M) with its principal component matrix A_p (containing the K PC rows of length N), and then remapping the obtained values at each (n,m) matrix position to their original map coordinate. If K were equal to N , then the reconstructed maps must be exactly identical to the original maps; however, in general the first modes that explain much of the data variability are most relevant, and therefore reconstructed maps may appear as a simplified first-order version of their original inputs.

Table S1.

Vertices of unitary seismic segments. Unitary seismic segment presented in main text figure 8 are identified by an Identification Code (IC) in the first column formed by letters referring to the master seismic segment at which they belongs (I=Iquique 1877, A=Antofagasta 1995, C=Copiapo 1922, VP=Valparaiso 1730, M=Maule 2010, VD=Valdivia 1960) and a number referring to its north-south location inside the respective master segment. Columns 2 to 5 list the geographic coordinates of respectively northwest, northeast, southeast and southwest vertices delimiting each unitary segment.

IC	NW	NE	SE	SW
I1	-19.1, -71.7	-18.41, -70	-20.16, -69.35	-20.35, -71.26
I2	-20.35, -71.26	-20.16, -69.35	-21.65, -69.27	-21.6, -71.2
I3	-21.6, -71.2	-21.65, -69.27	-23.7, -69.38	-23.6, -71.33
A1	-23.6, -71.33	-23.7, -69.38	-25.55, -69.51	-25.2, -71.46
C1	-25.2, -71.46	-25.55, -69.51	-27.55, -69.89	-27.25, -71.87
C2	-27.25, -71.87	-27.55, -69.89	-29.98, -70.34	-29.8, -72.4
VP1	-29.8, -72.4	-29.98, -70.34	-31.98, -70.55	-31.4, -72.62
VP2	-31.4, -72.62	-31.98, -70.55	-33.45, -70.89	-32.9, -72.92
VP3	-32.9, -72.92	-33.45, -70.89	-34.46, -71.26	-33.8, -73.27
M1	-33.8, -73.27	-34.46, -71.26	-36.16, -72.05	-35.6, -74.14
M2	-35.6, -74.14	-36.16, -72.05	-36.87, -72.33	-36.5, -74.52
M3	-36.5, -74.52	-36.87, -72.33	-37.8, -72.57	-37.6, -74.82
VD1	-37.6, -74.82	-37.8, -72.57	-38.85, -72.71	-38.6, -75
VD2	-38.6, -75	-38.85, -72.71	-40.01, -72.83	-39.8, -75.14
VD3	-39.8, -75.14	-40.01, -72.83	-41.15, -73	-40.85, -75.34
VD4	-40.85, -75.34	-41.15, -73	-42.18, -73.18	-42.00, -75.58
VD5	-42.00, -75.58	-42.18, -73.18	-43.36, -73.33	-43.2, -75.79
VD6	-43.2, -75.79	-43.36, -73.33	-44.25, -73.38	-44.16, -75.88

Figure S1 and Figure S2.

These figures were produced to show the similarity of the first order along-trench patterns recognized by the PCA method when applied to different interseismic geodetic locking grids. For this we considered our concatenated locking grid (see section 3.2.3 in main text) along with grids published by Metois et al. (2016, hereafter

M16) and Saillard et al. (2017, hereafter S17). We first cut our locking grid till 38°S, which is the southward extent of M16 and S17. Then, we applied our PCA method to each locking grid in an isolated way (i.e. $C=1$) in order to obtain their individual first-order spatial patterns (i.e. $k=1$).

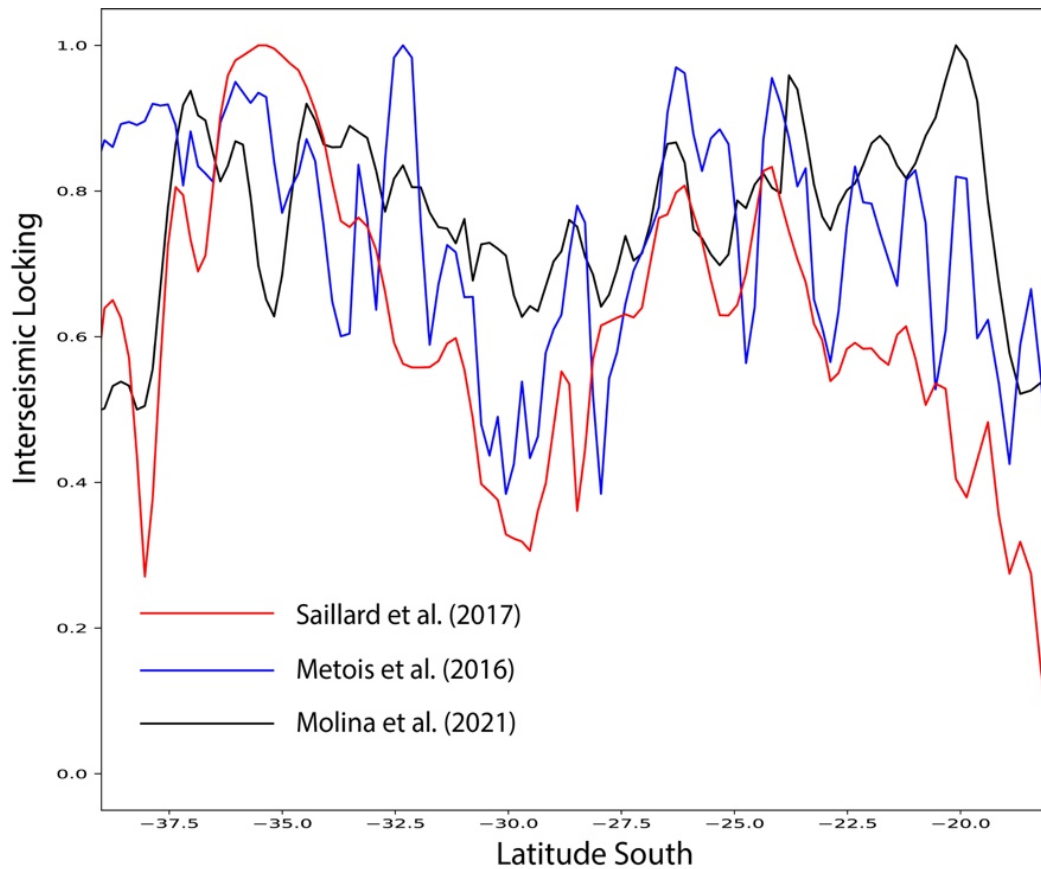


Figure S1. Empirical Orthogonal Functions (EOFs) for the first PCA mode ($k=1$) of different interseismic locking grids. We note a rather similar long wavelength (1000 km) along-trench tendency and a general coincidence in the location of short wavelength (100 km) fluctuations of this tendency, although the amplitude of the signal and spatial gradients may differ.

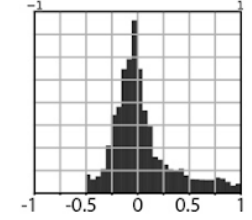
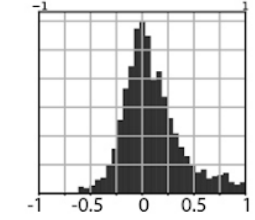
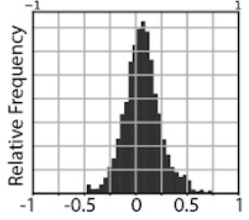
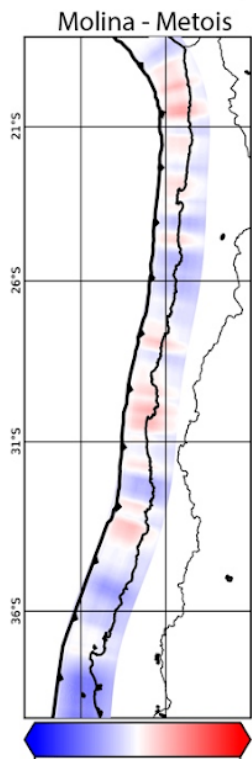
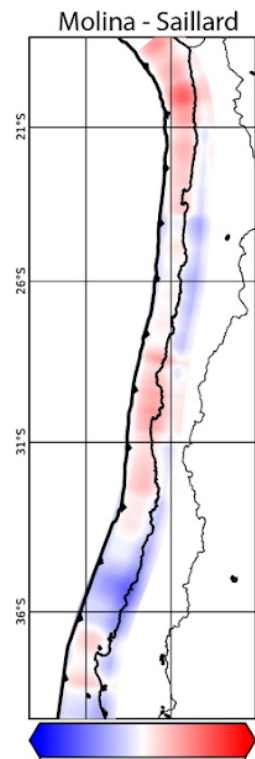
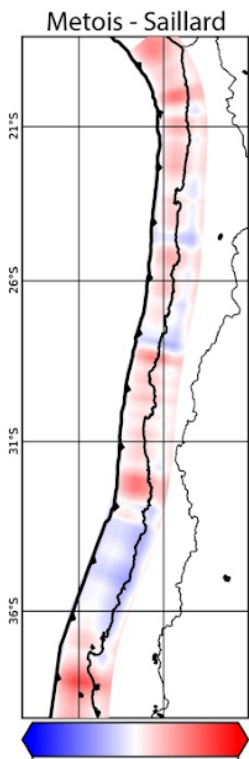
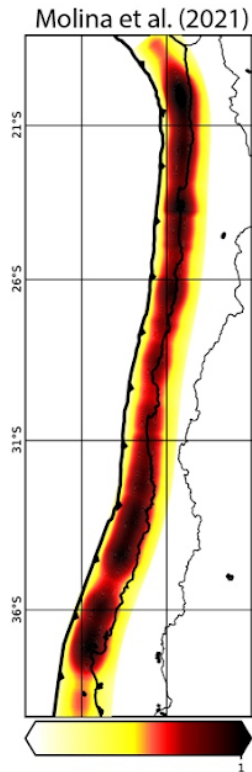
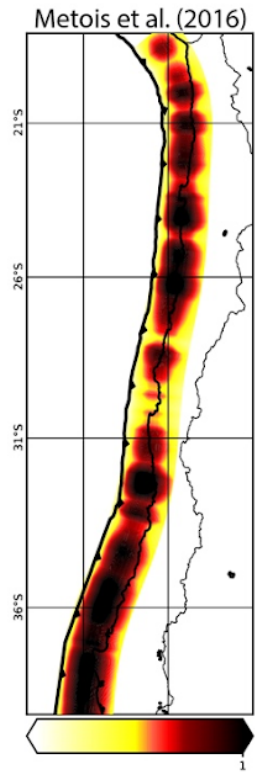
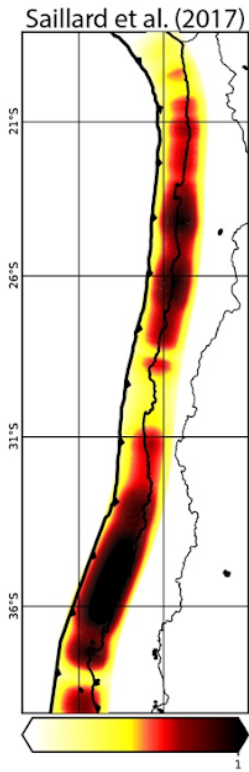


Figure S2. Reconstructed spatial distributions of different locking grids for $k=1$ (upper panel). As a consequence of the similarity in their EOFs, we note that these maps are rather similar one to each other, mostly in the along-strike distribution of highs and lows of locking, which is the most relevant feature considered in our analysis. This analysis is complemented with (mid panel) maps where we plotted the difference between pairs of locking grids and (lower panel) histograms showing the frequency distribution of these differences. These figures further demonstrate the first order similarity between different locking grids, with residuals clearly showing a gaussian distribution around zero for the three possible combinations.

6.2 (A2) Supplementary Material Chapter 2

Slip behavior of velocity-weakening barriers

Diego Molina-Ormazabal ^{1,2}, Jean-Paul Ampuero ³, Andrés Tassara ^{1,2}

1 Departamento Ciencias de la Tierra, Facultad de Ciencias Químicas, Universidad de Concepción, Concepción, Chile,

2 Millennium Nucleus The Seismic Cycle Along Subduction Zones CYCLO, Valdivia, Chile,

3 Université Côte d'Azur, IRD, CNRS, Observatoire de la Côte d'Azur, Géoazur, Sophia Antipolis, France,

Cite: Molina, D., Tassara, A., Abarca, R., Melnick, D., & Madella, A. (2021). Frictional segmentation of the Chilean megathrust from a multivariate analysis of geophysical, geological, and geodetic data.

Journal of Geophysical Research: Solid Earth, 126, e2020JB020647.

<https://doi.org/10.1029/2020JB020647>

Figures Extended data

Contents

1. Figure Extended data 1
2. Figure Extended data 2
3. Figure Extended data 3
4. Figure Extended data 4

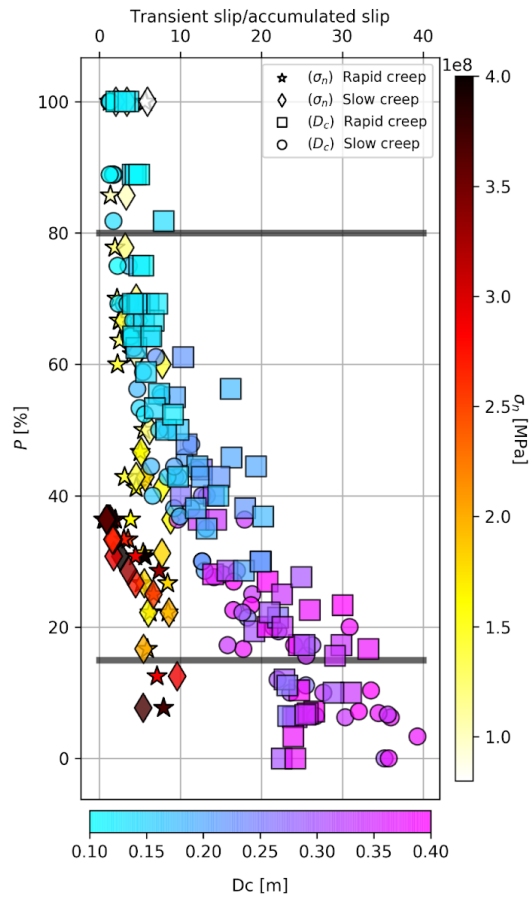


Figure Extended data 1: The diversity of slip behavior in VW barrier types. P as a function of the percentage of rapid creep slip (stars and squares) and slow creep slip (crosses and circles) relative to the total accumulated slip (**see Methods 3.5.6**). A large transient slip relative to the total accumulated slip means an increase in the amount of aseismic slip hosted by the CVWP (x-axis). As D_c is increased (violet colors), the aseismic slip increases too. The same is observed in simulation with normal stress contrast (with values up to twice the asperity σ_n), but when σ_n exceeds twice the asperities' value (red colors), the transient slip decreases, implying an increment in the seismic slip within the CVWP. Further, a smaller ratio between transient and total accumulated slip means major seismic slip within the CCVWP. Warm and cool colors depict variations in σ_n and D_c values respectively whereas vertical gray solid lines display barrier type depending on probability P .

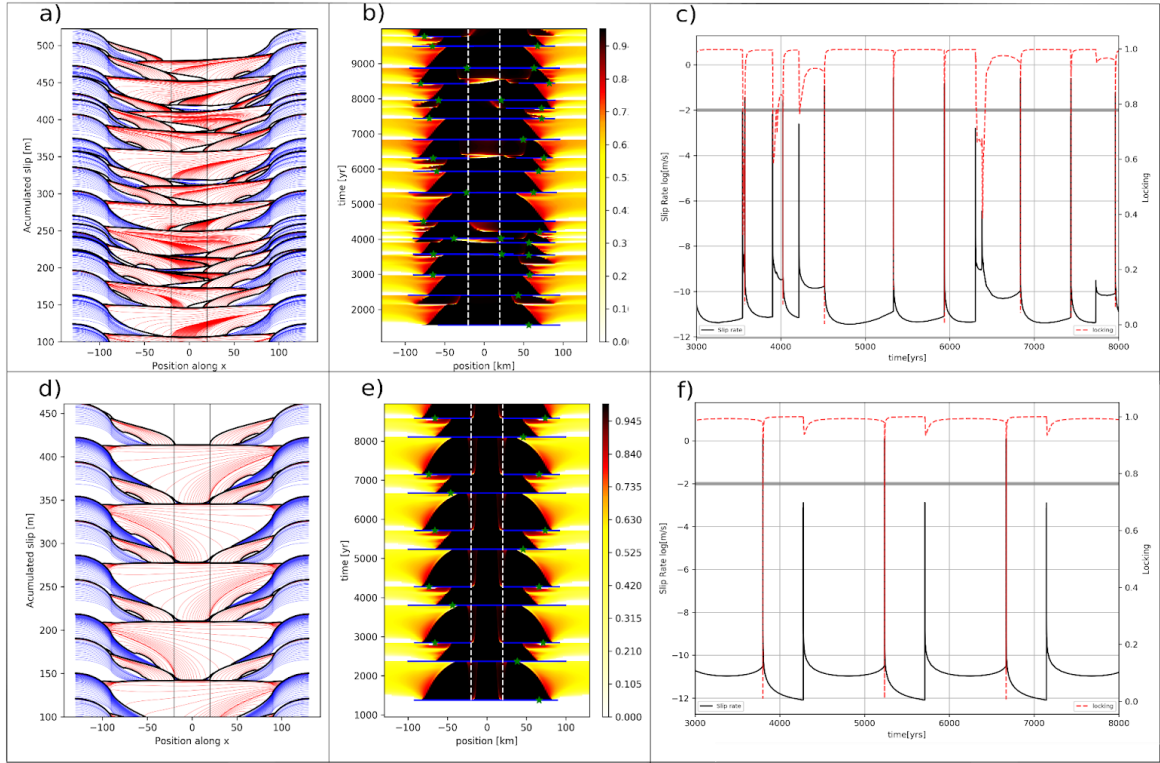


Figure Extended data 2: Seismic cycle simulations of frequent barriers. The barrier has a length of 40 km and is defined by (top) a low $D_c = 0.18 m$ and (bottom) a high $\sigma_n = 370 MPa$. a,d): Accumulated slip profiles along the fault during interseismic periods (blue, every 2 years) and during earthquakes (red, every 5 seconds); Black lines depict the start and ending of earthquakes. Solid black lines display the edges of the CVWP. b,e): space-time distribution of instantaneous ISC (equation 20, see Methods 3.5.7). Blue solid lines and green stars show the rupture length and epicenter of earthquakes, respectively. Dashed white lines indicate the edges of the CVWP. c,f): Instantaneous ISC averaged across the CVWP (red dashed lines) and slip rate averaged across the whole fault (black solid lines) as a function of time. The horizontal gray line indicates our chosen threshold for seismic slip rates, 1 cm/s. ISC varies throughout the seismic cycle, although the values are most often close to 1 (fully locked). Some transients are aseismic, their slip rates do not reach seismic velocities.

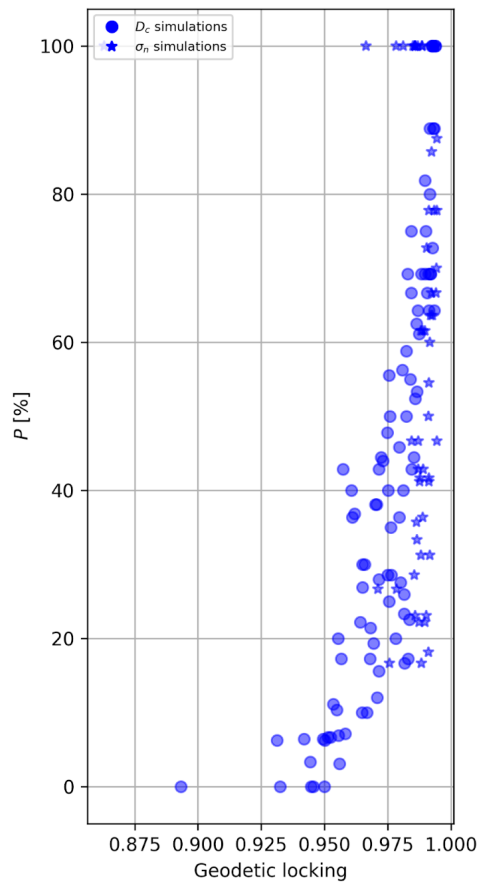


Figure Extended data 3: Long-term interseismic coupling in the CVWP. For each simulation, the long-term ISC is computed at each point inside the CVWP using equation 21 (see **Methods A7**) and then averaged spatially across the CVWP. Blue circles and stars correspond to simulations with D_c and σ_n contrast, respectively. Most values are higher than 0.95, implying that in the long term, some barriers can display high ISC.

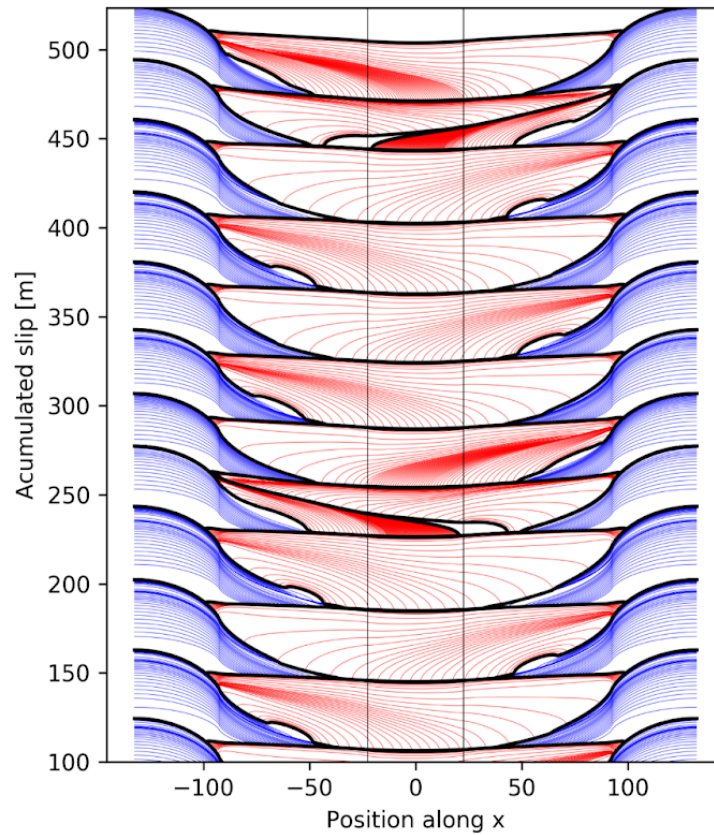


Figure Extended data 4: Reference seismic cycle simulation. Cumulative slip profiles along the fault during interseismic periods (blue, every 2 years) and during earthquakes (red, every 5 seconds); Black lines depict the start and ending of earthquakes. Reference model with uniform $D_c = 0.1 m$ and $\sigma_n = 95 MPa$ (there is a small increase of a in a 45 km-long CVWP). **b)** A model with very high $\sigma_n = 220 MPa$ in a 60 km-long CVWP.

Slip behavior of velocity-weakening barriers

Diego Molina-Ormazabal^{1,2}, Jean-Paul Ampuero³, Andrés Tassara^{1,2}

1 Departamento Ciencias de la Tierra, Facultad de Ciencias Químicas, Universidad de Concepción, Concepción, Chile,

2 Millennium Nucleus The Seismic Cycle Along Subduction Zones CYCLO, Valdivia, Chile,

3 Université Côte d'Azur, IRD, CNRS, Observatoire de la Côte d'Azur, Géoazur, Sophia Antipolis, France,

Submitted to *Nature Geosciences* on March, 22, 2022

Supplementary material

Contents

1. Predicting barrier efficiency
2. Estimating the efficiency of natural barriers

Predicting barrier efficiency λ

While equation 17 needs to be computed from model outputs, a posteriori, here we propose an a priori estimator of λ based on model inputs. We develop scaling relationships between asperity stress drop ($\Delta\tau_a$) and fault input parameters, σ_n , D_c and L_B . For each simulation, we compute the mean stress drop across the asperity for all earthquakes halting at the barrier or breaking it entirely. For a given set of simulations with fixed D_c (or σ_n) but varying L_B , we estimate the asperity stress drop ($\Delta\tau_{am}$) averaged among all different L_B cases. We find an almost linear relation between $\Delta\tau_{am}$ and D_c (or σ_n) **[Fig. S1, left panel]**, with best-fitting relations of the following form:

$$\widehat{\Delta\tau}_{am} = a_1 + a_2 \times D_c \quad \text{and} \quad \widehat{\Delta\tau}_{am} = b_1 + b_2 \times \sigma_n \quad (22)$$

where a_1, a_2, b_1 and b_2 are constants. Similarly, we derive a scaling relation for the barrier stress drop ($\Delta\tau_b$).

For simulations with the same barrier length L_B , we take the mean stress drop across the central VW patch for each earthquake, then average among all the events in the simulation set with variable D_c (or σ_n) to obtain a mean barrier stress drop ($\Delta\tau_{bm}$). We find an inverse relation between $\Delta\tau_{bm}$ and L_B , which is more clear in the set with variable D_c **[Fig. S1, right panel]**, with best-fitting relations of the form:

$$\widehat{\Delta\tau}_{bm} = a_3 + a_4 \times L_b \quad \text{and} \quad \widehat{\Delta\tau}_{bm} = b_3 + b_4 \times L_b \quad (23)$$

for the variable D_c and variable σ_n sets, respectively, where a_3, a_4, b_3 and b_4 are constants.

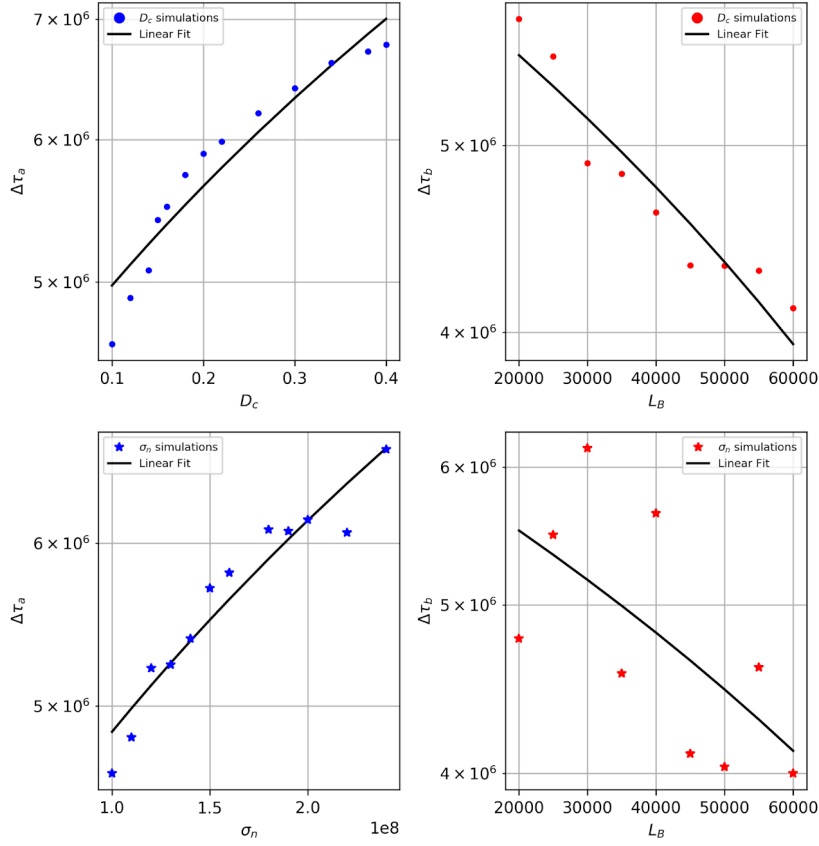


Figure S1: Stress drop dependency with D_c , σ_n or barrier length L_B observed from the earthquake simulations. Left panels: Blue dots and stars depict representative asperity stress drop $\Delta\tau_{am}$ values as a function of frictional parameters D_c and σ_n respectively. The black solid line represents a linear polynomial used to fit the values, which allows us to obtain a scaling relation between $\Delta\tau_{am}$ and D_c or σ_n (equation 22). Right panels: Red dots and stars display average barrier stress drop $\Delta\tau_{bm}$ depending on barrier length (L_B) (equation 23). The black solid line fits the values, showing an inverse relation between barrier stress drop and its length. These linear fits provide another scaling relation used to predict the barrier efficiency λ .

$$G_{cp} = \frac{bD_c \sigma_n [\ln(V\theta/D_c)]^2}{2} \quad (24)$$

In particular, in this expression G_c is proportional to the product $D_c \sigma_n$ of the two fault parameters varied in our simulations. Both, G_{1opx} and G_{cp} are displayed on figure S2.

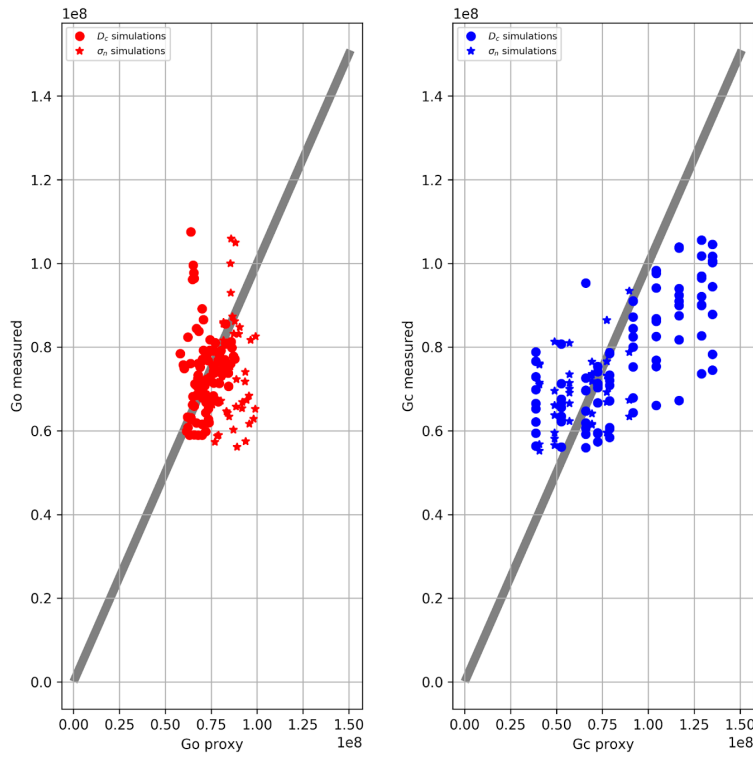


Figure S2: G_o and G_c mean values from simulations (originally used to estimate λ , Methods 3.5.3) compared with G_{cp} and G_{1opx} proxies mean values calculated considering stress drop dependency with D_c , σ_n and barrier length L_B [Figure S1]. Left panel: Red stars and circles are estimations for G_{1opx} computed for a given value of L_B and D_c (or σ_n) considering stress drop dependency shown in Figure S1 and equation 10 (this work). Then it is compared with the mean G_o (used to estimate λ), which is displayed in the y-axis. Right panel: Blue circles (or blue stars) represent G_{cp} (Rubin-Ampuero 2005, **equation 24**) considering the same values of D_c (or σ_n). Then the values are compared with the original G_c average values coming from the simulations (see Methods 3.5.4). Gray solid line is the straight line with slope 1, shown for reference. These G_c and G_o proxies together with the stress drop predictions (**Fig. S1, Fig. S2**) are finally used to obtain a predicted λ_p (**Fig. S3**)

These scaling relations are then used in equations 10 to estimate G_{oi} for each simulation (see Methods 3). Then, the proxy predicted for the asperity static energy release rate is called G_{1opx} .

To estimate the fracture energy associated to rate-and-state friction, we adopt the estimate derived by Rubin and Ampuero (2005):

Finally, the predicted λ_p constrained by our proxies is

$$\lambda_p = \frac{G_c}{G_{1opx}} T^m \quad (25)$$

In Figure S3 it can be noted that λ_p is able to reproduce the main tendencies of the original barrier efficiency index derived from our simulations (measured λ).

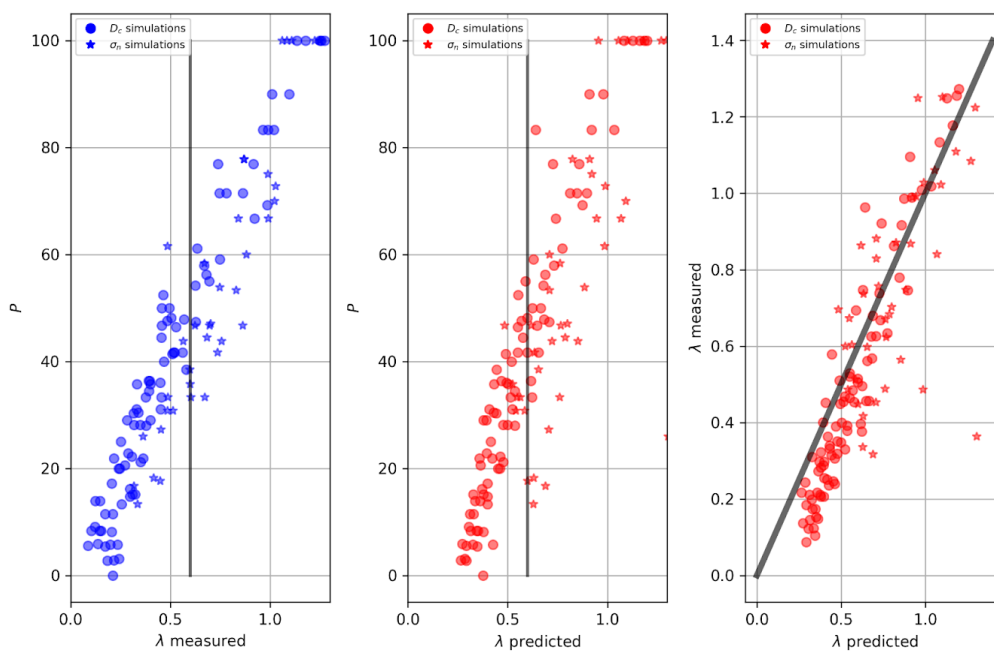


Figure S3: Measured and predicted λ compared with the probability P (Percentage of events breaking the barrier). Left: Blue circles and stars represent estimations of barrier efficiency derived from simulations where D_c and σ_n have been varied respectively [Figure 4c]. **Middle:** predicted values of λ obtained from G_c, G_o proxies (G_{1opx}, G_{cp} , **Figure S2,**) and stress drop scaling (**equations 22, 23**) with frictional and geometrical parameters (D_c, σ_n circles and stars respectively). Red represents λ_p (**equation 25**). Vertical gray line shows the threshold of temporary or permanent barriers. For $\lambda < 0.3$ the probability of having permanent barrier increases and for $\lambda > 1$ the probability of having temporary barrier increases too. **Right:** Measured λ values [y-axis] as a function of predicted λ_p [x-axis]. Solid gray line displays the slope 1 reflecting 1 to 1 correlation.

Estimating the efficiency of natural barriers

Natural seismic barriers can be categorized through the efficiency barrier parameter λ derived in this work (equation 17) by devising estimates of the quantities involved (G_c , G_{oi} and $\Delta\tau$) based on observable quantities. While the simulations conducted here assumed rate-and-state friction, fault friction at the natural scale is expected to involve additional weakening processes. In the absence of a universal friction law for faults, following Weng and Ampuero (2020), we consider an empirical relation between G_c and final slip S of the form $G_c \sim BS^n$, where $B \approx 3$ and $n \approx 0.7$ are constants constrained by seismological observations. We estimate the asperity energy as $G_{oi} = \frac{\pi L_A \Delta\tau_A^2}{4\mu}$ where $\Delta\tau_A \sim \mu S_A/L_A$ is the stress drop on the asperity, S_A its slip and L_A its length. Using these relations and equation 17, we define a new barrier efficiency proxy:

$$\lambda' = \left[\frac{4L_A B S_B^n}{\pi \mu S_A^2} \right]^m \left[\frac{S_B L_A}{S_A L_B} \right]^n$$

where L_A and L_B are the asperity and barrier lengths, respectively, and S_B and S_A are the final averaged slip on the barrier and asperity, respectively.

As an example, we evaluate the proxy λ' for the Chilean margin around the southern end of the rupture area of the 2010 Maule earthquake. We estimate the length of the Maule South Segment ($L_A = 124 \text{ km}$) and the Arauco barrier ($L_B = 50 \text{ km}$) and the depth-averaged slip deficit from fault locking models based on geodetic data (**Figure S4; Molina et al., 2021; Moreno et al., 2010**). The slip deficit is obtained by multiplying the slip deficit rate (**Fig. S4 a**) and the time elapsed since the last big earthquake in 1835, and is then averaged across the seismogenic depth (**Fig. S4 b**). The resulting values are $S_B = 5.6 \text{ m}$ and $S_A = 6.8 \text{ m}$, which yield $\lambda' = 0.23$, categorizing the Arauco peninsula as a permanent barrier based on Fig 4c.

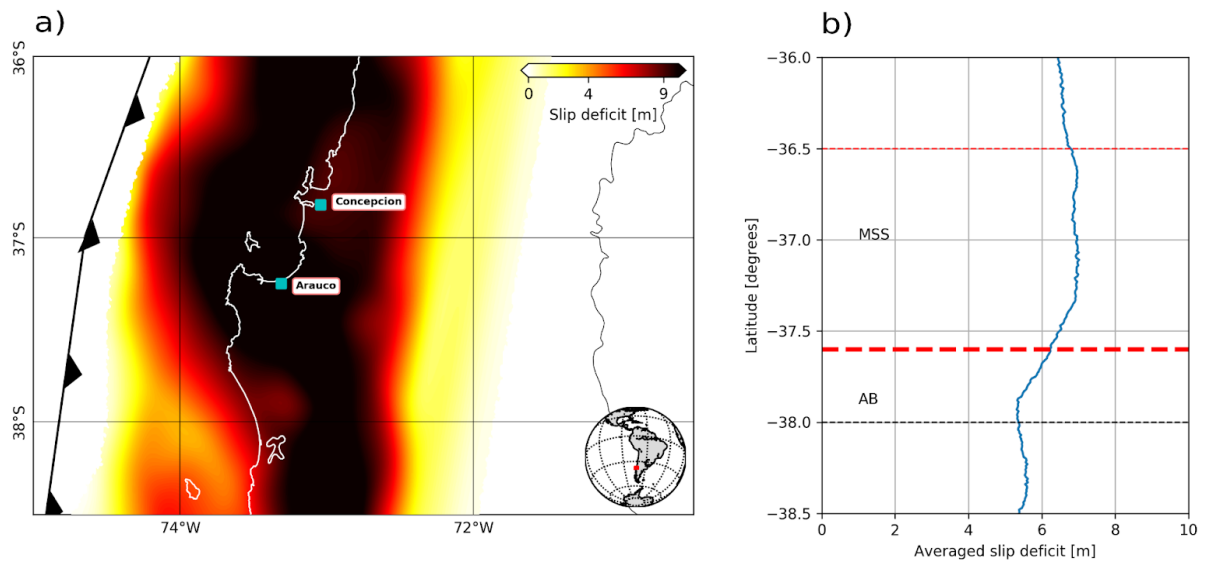


Figure S4: Slip deficit for the Maule earthquake area. a) Slip deficit in 2010 over the rupture area of the 2010 Maule earthquake considering 175 years of accumulation period since the last big earthquake in the region in 1835. b) Along-strike distribution of depth-averaged slip deficit (blue curve). Dashed red lines indicate the boundaries of the Maule South Segment (MSS). The thicker red line and black line indicate the boundaries of the Arauco barrier (AB).

6.3 (A3) Seismogenic width effect on seismic barriers

The dynamic propagation of earthquakes can be understood in the context of Linear Elasticity Fracture Mechanics (LEFM). During the interseismic phase, the accumulated elastic energy is stored along the fault as the potential energy of the system. Part of this energy is later released as an earthquake. At the rupture tip, where the crack is advancing, this elastic energy takes the form of radiated seismic waves and fracture energy G_c which is the dissipated energy. Also G_c is viewed as a material property characterizing the required energy to initiate sliding on the fault. To maintain a stable rupture growth, an energy balance must be satisfied which implies the equality between the fracture energy G_c and G_o . G_o is the static energy release rate, the energy flowing into the crack tip per unit of area and often it can be interpreted as the consumed energy during quasi-static growing crack. Fracture energy can be measured at each point of the fault as follows:

$$G_c = \int_0^{\delta} [\tau(\delta) - \tau_r] d\delta \quad (1)$$

Where δ is the slip and τ the tractions. The subscript r denotes the residual. In a circular crack G_o depends on the rupture radius and stress drop history along the fault. When the rupture becomes elongated, for instance when its length (L) exceeds the seismogenic width (W), G_o depends on W rather than L . Considering that $G_o = \frac{K_o^2}{2\mu}$ is calculated based on the static stress intensity factor (K_o), we proceed to use the K_o for long ruptures derived by Weng and Ampuero (2020) and taken here at zero rupture speed:

$$K_o = \sqrt{\frac{2}{\pi}} \int_0^L \frac{\Delta\tau(x)}{[L-x]^{1/2}} \exp\left(-\frac{x-L}{\gamma W}\right) dx \quad (2),$$

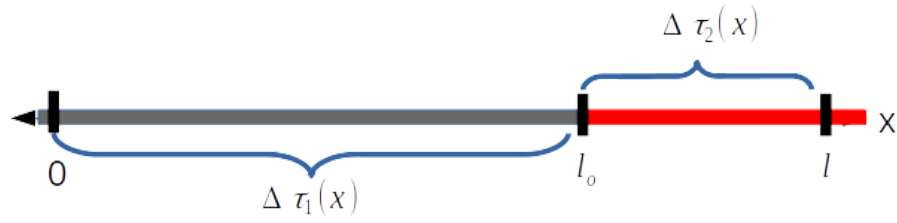
where $\gamma = \frac{1}{2\pi}$. If the stress drop $\Delta\tau$ is homogeneous along the fault, the stress intensity factor is:

$$K_o = \Delta\tau \sqrt{2\gamma W} * \operatorname{erf} \left\{ \sqrt{\frac{L}{\gamma W}} \right\} \quad (4),$$

where erf is the error function. For large rupture aspect ratio L/W , the argument of erf becomes large enough and $\operatorname{erf} \sim 1$. So, for elongated ruptures, the static stress intensity factor is:

$$K_o = \Delta\tau \sqrt{\frac{W}{\pi}} \quad (5)$$

and the static energy release rate is $G_o = \frac{\Delta\tau^2 W}{2\mu\pi}$ (6)



Scheme 1: Rupture propagation considering one large asperity (gray line) and one barrier (red line).

Let's consider an earthquake that breaks an asperity and penetrates into a region where fracture energy is higher (a barrier). The asperity of length l_o has a constant stress drop $\Delta\tau_1$. The broken portion of the barrier has length $l - l_o$ with a constant stress drop $\Delta\tau_2$. The total stress intensity factor has contributions from the asperity stress drop and the barrier stress drop: $K_{ot} = K_a + K_b$. Assuming $l_o/W \gg 1$ and taking equation (2), we rewrite K_{ot} as:

$$K_{ot} = \sqrt{\frac{2}{\pi}} \int_0^{l_o} \frac{\Delta\tau_1}{[l-x]^{1/2}} \exp\left(\frac{x-l}{\gamma W}\right) dx + \sqrt{\frac{2}{\pi}} \int_{l_o}^l \frac{\Delta\tau_2}{[l-x]^{1/2}} \exp\left(\frac{x-l}{\gamma W}\right) dx \quad (7)$$

Applying substitution method: $\int \frac{\exp(\frac{x-l}{a})}{[l-x]^{1/2}} dx = -\sqrt{a\pi} \operatorname{erf}\left\{\sqrt{\frac{l}{a}}\right\}$. Using this result in equation (7), we have

$$K_{ot} = \sqrt{\frac{2}{\pi}} \left[-\Delta\tau_1 \sqrt{W\pi\gamma} \operatorname{erf}\left\{\sqrt{\frac{l-x}{w\gamma}}\right\} \Big|_0^{l_o} - \Delta\tau_2 \sqrt{W\pi\gamma} \operatorname{erf}\left\{\sqrt{\frac{l-x}{w\gamma}}\right\} \Big|_{l_o}^l \right] \quad (8)$$

Replacing γ ,

$$K_{ot} = -\sqrt{\frac{2}{\pi}} \left[\Delta\tau_1 \sqrt{W/2} \operatorname{erf}\left\{\sqrt{\frac{2\pi(l-x)}{w}}\right\} \Big|_0^{l_o} + \Delta\tau_2 \sqrt{W/2} \operatorname{erf}\left\{\sqrt{\frac{2\pi(l-x)}{w}}\right\} \Big|_{l_o}^l \right] \quad (9)$$

$$K_{ot} = -\sqrt{\frac{2}{\pi}} \left[\Delta\tau_1 \sqrt{W/2} \left(\operatorname{erf}\left\{\sqrt{\frac{2\pi(l-l_o)}{w}}\right\} - \operatorname{erf}\left\{\sqrt{\frac{2\pi l}{w}}\right\} \right) + \Delta\tau_2 \sqrt{W/2} \left(\operatorname{erf}\left\{\sqrt{\frac{2\pi(l-l)}{w}}\right\} - \operatorname{erf}\left\{\sqrt{\frac{2\pi(l-l_o)}{w}}\right\} \right) \right] \quad (10)$$

$$K_{ot} = -\sqrt{\frac{2}{\pi}} \left[\Delta\tau_1 \sqrt{\frac{w}{2}} \left(\operatorname{erf}\left\{\sqrt{\frac{2\pi(l-l_o)}{w}}\right\} - \operatorname{erf}\left\{\sqrt{\frac{2\pi l}{w}}\right\} \right) - \Delta\tau_2 \sqrt{\frac{w}{2}} \operatorname{erf}\left\{\sqrt{\frac{2\pi(l-l_o)}{w}}\right\} \right] \quad (11)$$

Note that $erf\{\sqrt{\frac{2\pi l}{w}}\} \approx 1$ because the argument is large enough considering an elongated rupture. However the penetration length in the barrier can be comparable to W and thus the error function is different from 1. One way to deal with this case is to take the Taylor expansion of the error function, $erf(x) = \frac{2}{\sqrt{\pi}} (x - \frac{x^3}{5} + \frac{x^5}{10} \dots)$. In this

case $x = \sqrt{\frac{2\pi(l-lo)}{W}}$. Therefore considering just the first term of the erf Taylor expansion, we have that $erf\left\{\sqrt{\frac{2\pi(l-lo)}{W}}\right\} = \frac{2}{\sqrt{\pi}}\sqrt{\frac{2\pi(l-lo)}{W}}$.

Then equation (10) is rewritten and the total stress intensity factor is

$$K_{ot} = -\sqrt{\frac{2}{\pi}}[\Delta\tau_1\sqrt{\frac{w}{2}}\left(\frac{2}{\sqrt{\pi}}\sqrt{\frac{2\pi(l-lo)}{W}}\right) - 1] - \Delta\tau_2\sqrt{\frac{w}{2}}\frac{2}{\sqrt{\pi}}\sqrt{\frac{2\pi(l-lo)}{W}} \quad (12)$$

$$K_{ot} = \Delta\tau_1\sqrt{W/\pi} - 2\Delta\tau_1\sqrt{1/\pi}\sqrt{2(l-lo)} + 2\Delta\tau_2\sqrt{1/\pi}\sqrt{2(l-lo)} \quad (13)$$

$$K_{ot} = \frac{1}{\sqrt{\pi}}[\Delta\tau_1\sqrt{W} + 2(\Delta\tau_2 - \Delta\tau_1)\sqrt{2(l-lo)}] \quad (14)$$

As the static energy release rate is proportional to the stress intensity factor such as $G_o = \frac{K_{ot}^2}{2\mu}$

$$G_o = \frac{1}{2\mu\pi}[\Delta\tau_1\sqrt{W} + 2(\Delta\tau_2 - \Delta\tau_1)\sqrt{2(l-lo)}]^2 \quad (15)$$

Therefore equation 11 represents an approximation to the static energy release rate for very elongated ruptures penetrating in a barrier with length similar to W .

It was established before that a condition to have steady ruptures, the fracture energy must be equal to the static energy release rate $G_c = G_o$. Replacing G_o for equation 11, the energy balance is

$$G_c = \frac{1}{2\mu\pi}[\Delta\tau_1\sqrt{W} + 2(\Delta\tau_2 - \Delta\tau_1)\sqrt{2(l-lo)}]^2 \quad (16)$$

$$\sqrt{2\mu\pi G_c} = \Delta\tau_1\sqrt{W} + 2(\Delta\tau_2 - \Delta\tau_1)\sqrt{2(l-lo)} \quad (17)$$

Taking (13) and dividing by $\Delta\tau_1\sqrt{W}$

$$\sqrt{\frac{2\mu\pi G_c}{\Delta\tau_1^2 W}} = 1 + 2\left(\frac{\Delta\tau_2}{\Delta\tau_1} - 1\right)\sqrt{2(l-lo)/W} \quad (18)$$

Having in mind equation (5) and defining $T = \frac{\Delta\tau_2}{\Delta\tau_1}$, we have that

$$\left(\sqrt{\frac{G_c}{G_{oa}}} - 1\right) \frac{1}{2(T-1)} = \sqrt{2(l - lo)/W} \quad (19)$$

where G_{oa} is the asperity static energy release rate.

Finally, the rupture will propagate at steady velocity a distance:

$$l_s = (l - lo) = \frac{W}{8} \left(\sqrt{\frac{G_c}{G_{oa}}} - 1\right)^2 \left(\frac{1}{T-1}\right)^2 \quad (20)$$

7. Thesis References

1. Aki, K., Asperities, barriers, characteristic earthquakes, and strong motion prediction, *J. Geophys. Res.*, 89(B7)1984.
2. Orlando Álvarez, Silvina Nacif, Mario Gimenez, Andres Folguera, Carla Braitenberg, GOCE derived vertical gravity gradient delineates great earthquake rupture zones along the Chilean margin, *Tectonophysics*, Volume 622, 2014, Pages 198-215, ISSN 0040-1951, <https://doi.org/10.1016/j.tecto.2014.03.011>.
3. Beck, S., Barrientos, S., Kausel, E., & Reyes, M. (1998). Source characteristics of historic earthquakes along the central Chile subduction zone. *Journal of South American Earth Sciences*, 11, 115–129. [https://doi.org/10.1016/S0895-9811\(98\)00005-4](https://doi.org/10.1016/S0895-9811(98)00005-4)
4. Béjar-Pizarro, M., Socquet, A., Armijo, R. *et al.* Andean structural control on interseismic coupling in the North Chile subduction zone. *Nature Geosci* 6, 462–467 (2013). <https://doi.org/10.1038/ngeo1802>
5. Bürgmann, R., Kogan, M. G., Steblov, G. M., Hilley, G., Levin, V. E., and Apel, E. (2005), Interseismic coupling and asperity distribution along the Kamchatka subduction zone, *J. Geophys. Res.*, 110, B07405, doi:[10.1029/2005JB003648](https://doi.org/10.1029/2005JB003648).
6. Boatwright, J., and Cocco, M. (1996), Frictional constraints on crustal faulting, *J. Geophys. Res.*, 101(B6), 13895– 13909, doi:[10.1029/96JB00405](https://doi.org/10.1029/96JB00405).
7. Carvajal, M., Cisternas, M., & Catalán, P. A. (2017). Source of the 1730 Chilean earthquake from historical records: Implications for the future tsunami hazard on the coast of Metropolitan Chile. *Journal of Geophysical Research: Solid Earth*, 122, 3648–3660. <https://doi.org/10.1002/2017JB014063>
8. Cisternas, M., Atwater, B. F., Torrejón, F., Sawai, Y., Machuca, G., Lagos, M., et al. (2005). Predecessors of the giant 1960 Chile earthquake. *Nature*, 437, 404–407. <https://doi.org/10.1038/nature03943>
9. Contreras-Reyes, E., & Carrizo, D. (2011). Control of high oceanic features and subduction channel on earthquake ruptures along the Chile-Peru subduction zone. *Physics of the Earth and Planetary Interiors*, 186, 49–58. <https://doi.org/10.1016/j.pepi.2011.03.002>
10. Contreras-Reyes, E., E. R. Flueh, and I. Grevemeyer (2010), Tectonic control on sediment accretion and subduction off south central Chile: Implications for coseismic rupture processes of the 1960 and 2010 megathrust earthquakes, *Tectonics*, 29, TC6018, doi:[10.1029/2010TC002734](https://doi.org/10.1029/2010TC002734).
11. J. Cortés-Aranda, R. González, V. Fernández, L. Astudillo, M. Miller, D. Molina, A. Oviedo, Neotectonic evidence for Late Quaternary reverse faulting in the northern Chile outer forearc (22.5°S-23°S): Implications for seismic hazard, *Journal of South American Earth Sciences*, Volume 109, 2021, 103219, ISSN 0895-9811, <https://doi.org/10.1016/j.jsames.2021.103219>.

12. Hayes, G. P., Moore, G. L., Portner, D. E., Hearne, M., Flamme, H., Furtney, M., & Smoczyk, G. M. (2018). Slab2, a comprehensive subduction zone geometry model. *Science*, 362, 58–61. <https://doi.org/10.1126/science.aat4723>
13. Dahlen, F. A. (1984). Noncohesive critical Coulomb wedges: An exact solution. *Journal of Geophysical Research*, 89, 10125–10133. <https://doi.org/10.1029/JB089iB12p10125>
14. Davis, D., Suppe, J., Dahlen, F.A., 1983. Mechanics of fold-and- thrust belts and accretionary wedges. *Journal of Geophysical Research* 88 (B2), 1153–1172.
15. Dieterich, J. H., Time-dependent friction and the mechanics of stick-slip, *J. Geophys. Res.*, 116 , 790–806, 1978.
16. Gabriel Easton, José González-Alfaro, Angelo Villalobos, Gabriel Álvarez, Diego Melgar, Sergio Ruiz, Bernardo Sepúlveda, Manuel Escobar, Tomás León, Juan Carlos Báez, Tatiana Izquierdo, Maximiliano Forch, Manuel Abad; Complex Rupture of the 2015 Mw 8.3 Illapel Earthquake and Prehistoric Events in the Central Chile Tsunami Gap. *Seismological Research Letters* 2022; doi: <https://doi.org/10.1785/0220210283>
17. Lisa L. Ely, Marco Cisternas, Robert L. Wesson, Tina Dura; Five centuries of tsunamis and land-level changes in the overlapping rupture area of the 1960 and 2010 Chilean earthquakes. *Geology* 2014;; 42 (11): 995–998. doi: <https://doi.org/10.1130/G35830.1>
18. Folguera, A., Gianni, G. M., Encinas, A., Álvarez, O., Orts, D., Echaurren, A., et al., 2018. Neogene growth of the Patagonian Andes. In A. Folguera, E. Contreras-Reyes, N. Heredia, A. Encinas, B. Iannelli, V. Oliveros, et al. (Eds.), *The evolution of the Chilean-Argentinean Andes*, Springer Earth System Sciences (pp. 475–501). Springer International Publishing. https://doi.org/10.1007/978-3-319-67774-3_19
19. Fossum, A. F., and L. B. Freund (1975). Nonuniformly moving shear crack model of a shallow focus earthquake mechanism, *J. Geophys. Res.* 80, no. 23, 3343–3347, doi: 10.1029/JB080i023p03343.
20. Herrendörfer, R., van Dinther, Y., Gerya, T. *et al.* Earthquake supercycle in subduction zones controlled by the width of the seismogenic zone. *Nature Geosci* 8, 471–474 (2015). <https://doi.org/10.1038/ngeo2427>
21. Hocking, E.P., Garrett, E., Aedo, D. et al. Geological evidence of an unreported historical Chilean tsunami reveals more frequent inundation. *Commun Earth Environ* 2, 245 (2021). <https://doi.org/10.1038/s43247-021-00319-z>
22. Lamb, S., 2006. Shear stresses on megathrusts: Implications for mountain building behind subduction zones. *Journal of Geophysical Research* 111 (B07401). doi:10.1029/2005JB003916.
23. Legrand, D., Tassara, A., & Morales, D. (2012). Megathrust asperities and clusters of slab dehydration identified by spatiotemporal characterization of seismicity below the Andean margin. *Geophysical Journal International*, 191(3), 923–931.

24. León, T., Vargas, G., Salazar, D., Goff, J., Guendon, J. L., Andrade, P., & Alvarez, G. (2019). Geo-archeological records of large Holocene tsunamis along the hyperarid coastal Atacama Desert in the major northern Chile seismic gap. *Quaternary Science Reviews*, 220, 335–358. <https://doi.org/10.1016/j.quascirev.2019.07.038>
25. J.P. Loveless, M.E. Pritchard, N. Kukowski, Testing mechanisms of subduction zone segmentation and seismogenesis with slip distributions from recent Andean earthquakes, *Tectonophysics*, Volume 495, Issues 1–2, 2010, Pages 15-33, ISSN 0040-1951, <https://doi.org/10.1016/j.tecto.2009.05.008>.
26. Loveless, J. P. & Meade, B. J. Spatial correlation of interseismic coupling and coseismic rupture extent of the 2011 MW=9.0 Tohoku-Oki earthquake. *Geophys. Res. Lett.* 38, L17306 (2011).
27. Jara-Muñoz, J., Melnick, D., Brill, D., & Strecker, M. R. (2015). Segmentation of the 2010 Maule Chile earthquake rupture from a joint analysis of uplifted marine terraces and seismic-cycle deformation patterns. *Quaternary Science Reviews*, 113, 171–192. <https://doi.org/10.1016/j.quascirev.2015.01.005>
28. Judith Marinier, Céline Beauval, Jean-Mathieu Nocquet, Mohamed Chlieh, Hugo Yepes; Earthquake Recurrence Model for the Colombia–Ecuador Subduction Zone Constrained from Seismic and Geodetic Data, Implication for PSHA. *Bulletin of the Seismological Society of America* 2021;; 111 (3): 1508–1528. doi: <https://doi.org/10.1785/0120200338>
29. Kempf, P., Moernaut, J., Van Daele, M., Pino, M., Urrutia, R., & De Batist, M. (2020). Paleotsunami record of the past 4300 years in the complex coastal lake system of Lake Cucao, Chiloé Island, south central Chile. *Sedimentary Geology*, 401, 105644. <https://doi.org/10.1016/j.sedgeo.2020.105644>
30. Meade, B.J., Conrad, C.P., 2008. Andean growth and the deceleration of South American subduction: Time evolution of a coupled orogen-subduction system. *Earth and Planetary Science Letters* 275 (1–2), 93–101.
31. Melnick, D., Bookhagen, B., Strecker, M. R., & Echtler, H. P. (2009). Segmentation of megathrust rupture zones from fore-arc deformation patterns over hundreds to millions of years, Arauco peninsula, Chile. *Journal of Geophysical Research*, 114. <https://doi.org/10.1029/2008JB005788>
32. Melnick, D.; Moreno, M.; Cisternas, M.; Tassara, A. 2012, Darwin' seismic gap closed by the 2010 Maule earthquake. *Andean Geology* 39 (3): 558-563. doi:<http://dx.doi.org/10.5027/andgeoV39n3-a11>
33. Métois, M., Vigny, C., & Socquet, A. (2016). Interseismic Coupling, megathrust earthquakes and seismic swarms along the Chilean Subduction Zone (38°–18°S). *Pure and Applied Geophysics*, 173, 1431–1449. <https://doi.org/10.1007/s00024-016-1280-5>
34. Mitiyasu Ohnaka; A physical basis for earthquakes based on the elastic rebound model. *Bulletin of the Seismological Society of America* 1976;; 66 (2): 433–451
35. Moernaut, J., Van Daele, M., Fontijn, K., Heirman, K., Kempf, P., Pino, M., et al. (2018). Larger earthquakes recur more periodically: New insights in the megathrust earthquake cycle

- from lacustrine turbidite records in south-central Chile. *Earth and Planetary Science Letters*, 481, 9–19. <https://doi.org/10.1016/j.epsl.2017.10.016>
36. Moreno, M., Rosenau, M., & Oncken, O. (2010). 2010 Maule earthquake slip correlates with pre-seismic locking of Andean subduction zone. *Nature*, 467, 198–202. <https://doi.org/10.1038/nature09349>
 37. Muldashev, I. A., & Sobolev, S. V. (2020). What controls maximum magnitudes of giant subduction earthquakes? *Geochemistry, Geophysics, Geosystems*, 21, e2020GC009145. <https://doi.org/10.1029/2020GC009145>
 38. Nakata, R., Hori, T., Miura, S. *et al.* Presence of interplate channel layer controls of slip during and after the 2011 Tohoku-Oki earthquake through the frictional characteristics. *Sci Rep* 11, 6480 (2021). <https://doi.org/10.1038/s41598-021-86020-9>
 39. Pastén-Araya, F., Potin, B., Azúa, K., Sáez, M., Aden-Antoniów, F., Ruiz, S., *et al.* (2022). Along-dip segmentation of the slip behavior and rheology of the Copiapó ridge subducted in north-central Chile. *Geophysical Research Letters*, 49, e2021GL095471. <https://doi.org/10.1029/2021GL095471>
 40. Philiposian, B. & Meltzner, A. J. Segmentation and supercycles: a catalog of earthquake rupture patterns from the Sumatran Sunda megathrust and other well-studied faults worldwide. *Quaternary Sci. Rev.* 241, 106390 (2020).
 41. Protti, M. *et al.* Nicoya earthquake rupture anticipated by geodetic measurement of the locked plate interface. *Nat. Geosci.* 7, 117–121 (2014).
 42. Rong, Y., Jackson, D. D., and Kagan, Y. Y. (2003), Seismic gaps and earthquakes, *J. Geophys. Res.*, 108, 2471, doi:10.1029/2002JB002334, B10.
 43. Rubin, A. M., and Ampuero, J.-P. (2005), Earthquake nucleation on (aging) rate and state faults, *J. Geophys. Res.*, 110, B11312, doi:10.1029/2005JB003686.
 44. Ruff L.J. (1989) Do Trench Sediments Affect Great Earthquake Occurrence in Subduction Zones?. In: Ruff L.J., Kanamori H. (eds) *Subduction Zones Part II. Pageoph Topical Volumes*. Birkhäuser Basel. https://doi.org/10.1007/978-3-0348-9140-0_9
 45. Ruiz, S., & Madariaga, R. (2018). Historical and recent large megathrust earthquakes in Chile. *Tectonophysics*, 733, 37–56. <https://doi.org/10.1016/j.tecto.2018.01.015>
 46. Saillard, M., Audin, L., Rousset, B., Avouac, J.-P., Chlieh, M., Hall, S. R., *et al.* (2017). From the seismic cycle to long-term deformation: Linking seismic coupling and Quaternary coastal geomorphology along the Andean megathrust. *Tectonics*, 36, 241–256. <https://doi.org/10.1002/2016TC004156>
 47. Sallarès, V., Ranero, C.R. Upper-plate rigidity determines depth-varying rupture behaviour of megathrust earthquakes. *Nature* 576, 96–101 (2019). <https://doi.org/10.1038/s41586-019-1784-0>

48. Schwartz, D. P., and Coppersmith, K. J. (1984), Fault behavior and characteristic earthquakes: Examples from the Wasatch and San Andreas Fault Zones, *J. Geophys. Res.*, 89(B7), 5681– 5698, doi:10.1029/JB089iB07p05681.
49. Christopher H. Scholz, Christopher Small; The effect of seamount subduction on seismic coupling. *Geology* 1997;; 25 (6): 487–490. doi: [https://doi.org/10.1130/0091-7613\(1997\)025<0487:TEOSSO>2.3.CO;2](https://doi.org/10.1130/0091-7613(1997)025<0487:TEOSSO>2.3.CO;2)
50. Bruce E. Shaw; Constant Stress Drop from Small to Great Earthquakes in Magnitude-Area Scaling. *Bulletin of the Seismological Society of America* 2009;; 99 (2A): 871–875. doi: <https://doi.org/10.1785/0120080006>
51. Song, T.-R. A., & Simons, M. (2003). Large trench-parallel gravity variations predict seismogenic behavior in subduction zones. *Science*, 301, 630–633. <https://doi.org/10.1126/science.1085557>
52. Tassara, A., Götze, H.-J., Schmidt, S., & Hackney, R. (2006). Three-dimensional density model of the Nazca plate and the Andean continental margin. *Journal of Geophysical Research*, 111, B09404. <https://doi.org/10.1029/2005JB003976>
53. Tassara, A., & Yáñez, G. (2003). Relación entre el espesor elástico de la litosfera y la segmentación tectónica del margen andino (15–47°S). *Revista Geologica de Chile*, 30. <https://doi.org/10.4067/S0716-02082003000200002>
54. Tassara, A. (2010). Control of forearc density structure on megathrust shear strength along the Chilean subduction zone. *Tectonophysics*, 495, 34–47. <https://doi.org/10.1016/j.tecto.2010.06.004>
55. von Huene, R., and Ranero, C. R. (2003), Subduction erosion and basal friction along the sediment-starved convergent margin off Antofagasta, Chile, *J. Geophys. Res.*, 108, 2079, doi:10.1029/2001JB001569, B2.
56. Wei, M., Kaneko, Y., Shi, P., & Liu, Y. (2018). Numerical modeling of dynamically triggered shallow slow slip events in New Zealand by the 2016 Mw 7.8 Kaikoura earthquake. *Geophysical Research Letters*, 45, 4764– 4772. <https://doi.org/10.1029/2018GL077879>
57. Wesson, R. L., Melnick, D., Cisternas, M., Moreno, M. & Ely, L. L. Vertical deformation through a complete seismic cycle at Isla Santa Maria, Chile. *Nat. Geosci.* 8, 547–551 (2015).
58. Weng, H., Ampuero, JP. Continuum of earthquake rupture speeds enabled by oblique slip. *Nat. Geosci.* 13, 817–821 (2020). <https://doi.org/10.1038/s41561-020-00654-4>
59. Weng, H., and Yang, H. (2017), Seismogenic width controls aspect ratios of earthquake ruptures, *Geophys. Res. Lett.*, 44, 2725– 2732, doi:10.1002/2016GL072168.

References Chapter 2

1. Aki, K. (1979). Characterization of barriers on an earthquake fault. *Journal of Geophysical Research*, 84, 6140. <https://doi.org/10.1029/JB084iB11p06140>

2. Avouac, J.-P. (2015). From geodetic imaging of seismic and aseismic fault slip to dynamic modeling of the seismic cycle. *Annual Review of Earth and Planetary Sciences*, 43, 233–271. <https://doi.org/10.1146/annurev-earth-060614-105302>
3. Barbot, S., Lapusta, N., & Avouac, J.-P. (2012). Under the hood of the earthquake machine: Toward predictive modeling of the seismic cycle. *Science*, 336, 707–710. <https://doi.org/10.1126/science.1218796>
4. Bassett, D., Sandwell, D. T., Fialko, Y., & Watts, A. B. (2016). Upper-plate controls on co-seismic slip in the 2011 magnitude 9.0 Tohoku-Oki earthquake. *Nature*, 531, 92–96. <https://doi.org/10.1038/nature16945>
5. Bassett, D., & Watts, A. B. (2015a). Gravity anomalies, crustal structure, and seismicity at subduction zones: 1. Seafloor roughness and subducting relief. *Geochemistry, Geophysics, Geosystems*, 16, 1508–1540. <https://doi.org/10.1002/2014GC005684>
6. Bassett, D., & Watts, A. B. (2015b). Gravity anomalies, crustal structure, and seismicity at subduction zones: 2. Interrelationships between fore-arc structure and seismogenic behavior. *Geochemistry, Geophysics, Geosystems*, 16, 1541–1576. <https://doi.org/10.1002/2014GC005685>
7. Beck, S., Barrientos, S., Kausel, E., & Reyes, M. (1998). Source characteristics of historic earthquakes along the central Chile subduction zone. *Journal of South American Earth Sciences*, 11, 115–129. [https://doi.org/10.1016/S0895-9811\(98\)00005-4](https://doi.org/10.1016/S0895-9811(98)00005-4)
8. Béjar-Pizarro, M., Socquet, A., Armijo, R., Carrizo, D., Genrich, J., & Simons, M. (2013). Andean structural control on interseismic coupling in the North Chile subduction zone. *Nature Geoscience*, 6(5), 462–467. <https://doi.org/10.1038/ngeo1802>
9. Bilek, S. L., & Lay, T. (2002). Tsunami earthquakes possibly widespread manifestations of frictional conditional stability. *Geophysical Research Letters*, 29, 181–184. <https://doi.org/10.1029/2002GL015215>
10. Bilek, S. L., & Lay, T. (2018). Subduction zone megathrust earthquakes. *Geosphere*, 14, 1468–1500. <https://doi.org/10.1130/GES01608.1>
11. Bilek, S. L., Lay, T., & Ruff, L. J. (2004). Radiated seismic energy and earthquake source duration variations from teleseismic source time functions for shallow subduction zone thrust

- earthquakes: Source time functions shallow subduction. *Journal of Geophysical Research*, 109. <https://doi.org/10.1029/2004JB003039>
12. Bishop, B. T., Beck, S. L., & Zandt, G. (2019). Segmentation in continental forearcs: Links between large-scale overriding plate structure and seismogenic behavior associated with the 2010 M 8.8 Maule, Chile earthquake. *Tectonophysics*, 767, 228164. <https://doi.org/10.1016/j.tecto.2019.228164>
 13. Blanpied, M. L., Lockner, D. A., & Byerlee, J. D. (1991). Fault stability inferred from granite sliding experiments at hydrothermal conditions. *Geophysical Research Letters*, 18, 609–612. <https://doi.org/10.1029/91GL00469>
 14. Bravo, F., Koch, P., Riquelme, S., Fuentes, M., & Campos, J. (2019). Slip Distribution of the 1985 Valparaíso earthquake constrained with seismic and deformation data. *Seismological Research Letters*. <https://doi.org/10.1785/0220180396>
 15. Bürgmann, R. (2018). The geophysics, geology and mechanics of slow fault slip. *Earth and Planetary Science Letters*, 495, 112–134. <https://doi.org/10.1016/j.epsl.2018.04.062>
 16. Bürgmann, R., Kogan, M. G., Steblov, G. M., Hilley, G., Levin, V. E., & Apel, E. (2005). Interseismic coupling and asperity distribution along the Kamchatka subduction zone. *Journal of Geophysical Research*, 110, B07405. <https://doi.org/10.1029/2005JB003648>
 17. Carena, S. (2011). Subducting-plate topography and nucleation of great and giant earthquakes along the South American Trench. *Seismological Research Letters*, 82, 629–637. <https://doi.org/10.1785/gssrl.82.5.629>
 18. Carlo, D. L., Lay, T., Ammon, C. J., & Zhang, J. (1999). Rupture Process of the 1995 Antofagasta Subduction Earthquake ($M_w = 8.1$). In Sauber, J., & Dmowska, R. (Eds.), *Seismogenic and tsunamigenic processes in shallow subduction zones*. (pp. 677–708). Birkhäuser Basel. https://doi.org/10.1007/978-3-0348-8679-6_13
 19. Carvajal, M., Cisternas, M., & Catalán, P. A. (2017). Source of the 1730 Chilean earthquake from historical records: Implications for the future tsunami hazard on the coast of Metropolitan Chile. *Journal of Geophysical Research: Solid Earth*, 122, 3648–3660. <https://doi.org/10.1002/2017JB014063>
 20. Charrier, R., Pinto, L., & Rodríguez, M. P. (2007). Tectonostratigraphic evolution of the Andean Orogen in Chile. In *The geology of Chile* (pp. 21–114).

21. Chlieh, M., Avouac, J. P., Sieh, K., Natawidjaja, D. H., & Galetzka, J. (2008). Heterogeneous coupling of the Sumatran megathrust constrained by geodetic and paleogeodetic measurements. *Journal of Geophysical Research*, 113, B05305. <https://doi.org/10.1029/2007JB004981>
22. Chlieh, M., de Chabali er, J. B., Ruegg, J. C., Armijo, R., Dmowska, R., Campos, J., & Feigl, K. L. (2004). Crustal deformation and fault slip during the seismic cycle in the North Chile subduction zone, from GPS and InSAR observations. *Geophysical Journal International*, 158, 695–711. <https://doi.org/10.1111/j.1365-246X.2004.02326.x>
23. Cisternas, M., Atwater, B. F., Torrej on, F., Sawai, Y., Machuca, G., Lagos, M., et al. (2005). Predecessors of the giant 1960 Chile earthquake. *Nature*, 437, 404–407. <https://doi.org/10.1038/nature03943>
24. Cisternas, M., Garrett, E., Wesson, R., Dura, T., & Ely, L. L. (2018). Reprint of Unusual geologic evidence of coeval seismic shaking and tsunamis shows variability in earthquake size and recurrence in the area of the giant 1960 Chile earthquake. *Marine Geology*, 396, 54–66. <https://doi.org/10.1016/j.margeo.2018.01.005>
25. Collot, J.-Y., Marcaillou, B., Sage, F., Michaud, F., Agudelo, W., Charvis, P., et al. (2004). Are rupture zone limits of great subduction earthquakes controlled by upper plate structures? Evidence from multichannel seismic reflection data acquired across the northern Ecuador-southwest Colombia margin. *Journal of Geophysical Research*, 109. <https://doi.org/10.1029/2004JB003060>
26. Comte, D., & Pardo, M. (1991). Reappraisal of great historical earthquakes in the northern Chile and southern Peru seismic gaps. *Natural Hazards*, 4, 23–44. <https://doi.org/10.1007/BF00126557>
27. Contreras-Reyes, E., & Carrizo, D. (2011). Control of high oceanic features and subduction channel on earthquake ruptures along the Chile-Peru subduction zone. *Physics of the Earth and Planetary Interiors*, 186, 49–58. <https://doi.org/10.1016/j.pepi.2011.03.002>
28. Cubas, N., Avouac, J.-P., Souloumiac, P., & Leroy, Y. (2013). Megathrust friction determined from mechanical analysis of the forearc in the Maule earthquake area. *Earth and Planetary Science Letters*, 381, 92–103. <https://doi.org/10.1016/j.epsl.2013.07.037>
29. Dahlen, F. A. (1984). Noncohesive critical Coulomb wedges: An exact solution. *Journal of Geophysical Research*, 89, 10125–10133. <https://doi.org/10.1029/JB089iB12p10125>

30. Davis, D., Suppe, J., & Dahlen, F. A. (1983). Mechanics of fold-and-thrust belts and accretionary wedges. *Journal of Geophysical Research*, 88, 1153. <https://doi.org/10.1029/JB088iB02p01153>
31. Davydenko, A. Y., & Grayver, A. V. (2014). Principal component analysis for filtering and leveling of geophysical data. *Journal of Applied Geophysics*, 109, 266–280. <https://doi.org/10.1016/j.jappgeo.2014.08.006>
32. Delouis, B., Philip, H., Dorbath, L., & Cisternas, A. (1998). Recent crustal deformation in the Antofagasta region (northern Chile) and the subduction process. *Geophysical Journal International*, 132, 302–338. <https://doi.org/10.1046/j.1365-246x.1998.00439.x>
33. den Hartog, S. A. M., Peach, C. J., de Winter, D. A. M., Spiers, C. J., & Shimamoto, T. (2012). Frictional properties of megathrust fault gouges at low sliding velocities: New data on effects of normal stress and temperature. *Journal of Structural Geology*, 38, 156–171. <https://doi.org/10.1016/j.jsg.2011.12.001>
34. Dielforder, A., Hetzel, R., & Oncken, O. (2020). Megathrust shear force controls mountain height at convergent plate margins. *Nature*, 582, 225–229. <https://doi.org/10.1038/s41586-020-2340-7>
35. Dieterich, J. H. (1981). Constitutive properties of faults with simulated gouge. In *Mechanical behavior of crustal rocks: The handin volume* (Vol. 24). <https://doi.org/10.1029/GM024p0103>
36. Fagereng, Å. (2011). Wedge geometry, mechanical strength, and interseismic coupling of the Hikurangi subduction thrust, New Zealand. *Tectonophysics*, 507(1–4), 26–30.
37. Folguera, A., Gianni, G. M., Encinas, A., Álvarez, O., Orts, D., Echaurren, A., et al., 2018. Neogene growth of the Patagonian Andes. In A. Folguera, E. Contreras-Reyes, N. Heredia, A. Encinas, B. Iannelli, V. Oliveros, et al. (Eds.), *The evolution of the Chilean-Argentinean Andes*, Springer Earth System Sciences (pp. 475–501). Springer International Publishing. https://doi.org/10.1007/978-3-319-67774-3_19
38. Froidevaux, C., & Isacks, B. L. (1984). The mechanical state of the lithosphere in the Altiplano-Puna segment of the Andes. *Earth and Planetary Science Letters*, 71, 305–314. [https://doi.org/10.1016/0012-821X\(84\)90095-5](https://doi.org/10.1016/0012-821X(84)90095-5)
39. Fuller, C. W., Willett, S. D., & Brandon, M. T. (2006). Formation of forearc basins and their influence on subduction zone earthquakes. *Geology*, 34(2), 65–68.

40. Gerstenberger, M. C., Marzocchi, W., Allen, T., Pagani, M., Adams, J., Danciu, L., et al. (2020). Probabilistic seismic hazard analysis at regional and national scales: State of the art and future challenges. *Review of Geophysics*, 58. <https://doi.org/10.1029/2019RG000653>
41. Haberland, C., Rietbrock, A., Lange, D., Bataille, K., & Dahm, T. (2009). Structure of the seismogenic zone of the southcentral Chilean margin revealed by local earthquake traveltome tomography. *Journal of Geophysical Research*, 114. <https://doi.org/10.1029/2008JB005802>
42. Hayes, G. P. (2017). The finite, kinematic rupture properties of great-sized earthquakes since 1990. *Earth and Planetary Science Letters*, 468, 94–100.
43. Hayes, G. P., Moore, G. L., Portner, D. E., Hearne, M., Flamme, H., Furtney, M., & Smoczyk, G. M. (2018). Slab2, a comprehensive subduction zone geometry model. *Science*, 362, 58–61. <https://doi.org/10.1126/science.aat4723>
44. He, X., Hua, X., Yu, K., Xuan, W., Lu, T., Zhang, W., & Chen, X. (2015). Accuracy enhancement of GPS time series using principal component analysis and block spatial filtering. *Advances in Space Research*, 55, 1316–1327. <https://doi.org/10.1016/j.asr.2014.12.016>
45. Hicks, S. P., Rietbrock, A., Ryder, I. M. A., Lee, C.-S., & Miller, M. (2014). Anatomy of a megathrust: The 2010 M8.8 Maule, Chile earthquake rupture zone imaged using seismic tomography. *Earth and Planetary Science Letters*, 405, 142–155. <https://doi.org/10.1016/j.epsl.2014.08.028>
46. [epsl.2014.08.028](https://doi.org/10.1016/j.epsl.2014.08.028)
47. Hua, Y., Zhao, D., Toyokuni, G., & Xu, Y. (2020). Tomography of the source zone of the great 2011 Tohoku earthquake. *Nature communications*, 11(1), 1–7.
48. Hyndman, R. D., & Wang, K. (1993). Thermal constraints on the zone of major thrust earthquake failure: The Cascadia Subduction Zone. *Journal of Geophysical Research*, 98, 2039–2060. <https://doi.org/10.1029/92JB02279>
49. Jara-Muñoz, J., Melnick, D., Brill, D., & Strecker, M. R. (2015). Segmentation of the 2010 Maule Chile earthquake rupture from a joint analysis of uplifted marine terraces and seismic-cycle deformation patterns. *Quaternary Science Reviews*, 113, 171–192. <https://doi.org/10.1016/j.quascirev.2015.01.005>
50. Ji, K. H., & Herring, T. A. (2013). A method for detecting transient signals in GPS position time-series: Smoothing and principal component analysis. *Geophysical Journal International*, 193, 171–186. <https://doi.org/10.1093/gji/ggt003>

51. Kagan, Y. Y., & Jackson, D. D. (1991). Long-term earthquake clustering. *Geophysical Journal International*, 104, 117–134. <https://doi.org/10.1111/j.1365-246X.1991.tb02498.x>
52. Kanamori, H. (2014). The diversity of large earthquakes and its implications for hazard mitigation. *Annual Review of Earth and Planetary Sciences*, 42, 7–26. <https://doi.org/10.1146/annurev-earth-060313-055034>
53. Kelleher, J. A. (1972). Rupture zones of large South American earthquakes and some predictions. *Journal of Geophysical Research*, 77, 2087–2103. <https://doi.org/10.1029/JB077i011p02087>
54. Kempf, P., Moernaut, J., Van Daele, M., Pino, M., Urrutia, R., & De Batist, M. (2020). Paleotsunami record of the past 4300 years in the complex coastal lake system of Lake Cucao, Chiloé Island, south central Chile. *Sedimentary Geology*, 401, 105644. <https://doi.org/10.1016/j.sedgeo.2020.105644>
55. Kendrick, E., Bevis, M., Smalley, R., Brooks, B., Vargas, R. B., Lauría, E., & Fortes, L. P. S. (2003). The Nazca-South America Euler vector and its rate of change. *Journal of South American Earth Sciences*, 16, 125–131. [https://doi.org/10.1016/S0895-9811\(03\)00028-2](https://doi.org/10.1016/S0895-9811(03)00028-2)
56. Koge, H., Fujiwara, T., Kodaira, S., Sasaki, T., Kameda, J., Kitamura, Y., et al. (2014). Friction properties of the plate boundary megathrust beneath the frontal wedge near the Japan Trench: An inference from topographic variation. *Earth Planets and Space*, 66, 153. <https://doi.org/10.1186/s40623-014-0153-3>
57. Kopp, H., Flueh, E. R., Papenberg, C., & Klaeschen, D. (2004). Seismic investigations of the O'Higgins Seamount Group and Juan Fernández Ridge: Aseismic ridge emplacement and lithosphere hydration. *Tectonics*, 23. <https://doi.org/10.1029/2003TC001590>
58. Kositsky, A. P., & Avouac, J.-P. (2010). Inverting geodetic time series with a principal component analysis-based inversion method. *Journal of Geophysical Research*, 115, B03401. <https://doi.org/10.1029/2009JB006535>
59. Lamb, S. (2006). Shear stresses on megathrusts: Implications for mountain building behind subduction zones. *Journal of Geophysical Research*, 111, B07401. <https://doi.org/10.1029/2005JB003916>
60. Lamb, S., & Davis, P. (2003). Cenozoic climate change as a possible cause for the rise of the Andes. *Nature*, 425, 792–797. <https://doi.org/10.1038/nature02049>

61. Lay, T., & Kanamori, H. (1981). An asperity model of large earthquake sequences. In D. W. Simpson, & P. G. Richards (Eds.), *Earthquake prediction, an international review*, Maurice Ewing series (pp. 579–592). American Geophysical Union. <https://doi.org/10.1029/ME004p0579>
62. Lay, T., Kanamori, H., Ammon, C. J., Koper, K. D., Hutko, A. R., Ye, L., et al. (2012). Depth-varying rupture properties of subduction zone megathrust faults. *Journal of Geophysical Research*, 117. <https://doi.org/10.1029/2011JB009133>
63. Legrand, D., Tassara, A., & Morales, D. (2012). Megathrust asperities and clusters of slab dehydration identified by spatiotemporal characterization of seismicity below the Andean margin. *Geophysical Journal International*, 191(3), 923–931.
64. León, T., Vargas, G., Salazar, D., Goff, J., Guendon, J. L., Andrade, P., & Alvarez, G. (2019). Geo-archeological records of large Holocene tsunamis along the hyperarid coastal Atacama Desert in the major northern Chile seismic gap. *Quaternary Science Reviews*, 220, 335–358. <https://doi.org/10.1016/j.quascirev.2019.07.038>
65. Li, D., & Liu, Y. (2017). Modeling slow-slip segmentation in Cascadia subduction zone constrained by tremor locations and gravity anomalies. *Journal of Geophysical Research: Solid Earth*, 122, 3138–3157. <https://doi.org/10.1002/2016JB013778>
66. Li, S., Moreno, M., Bedford, J., Rosenau, M., & Oncken, O. (2015). Revisiting viscoelastic effects on interseismic deformation and locking degree: A case study of the Peru-North Chile subduction zone. *Journal of Geophysical Research: Solid Earth*, 120, 4522–4538. <https://doi.org/10.1002/2015JB011903>
67. Liu, X., & Zhao, D. (2018). Upper and lower plate controls on the great 2011 Tohoku-Oki earthquake. *Scientific Advances*, 4, eaat4396. <https://doi.org/10.1126/sciadv.aat4396>
68. Llenos, A. L., & McGuire, J. J. (2007). Influence of fore-arc structure on the extent of great subduction zone earthquakes. *Journal of Geophysical Research*, 112, B09301. <https://doi.org/10.1029/2007JB004944>
69. Loveless, J. P., & Meade, B. J. (2011). Stress modulation on the San Andreas fault by interseismic fault system interactions. *Geology*, 39, 1035–1038. <https://doi.org/10.1130/G32215.1>

70. Maksymowicz, A. (2015). The geometry of the Chilean continental wedge: Tectonic segmentation of subduction processes off Chile. *Tectonophysics*, 659, 183–196. <https://doi.org/10.1016/j.tecto.2015.08.007>
71. Marone, C. (1998). The effect of loading rate on static friction and the rate of fault healing during the earthquake cycle. *Nature*, 391, 69–72. <https://doi.org/10.1038/34157>
72. Marshall, J. S., & Anderson, R. S. (1995). Quaternary uplift and seismic cycle deformation. *Geological Society of America Bulletin*, 107, 0463–0473. [https://doi.org/10.1130/0016-7606\(1995\)107<0463:quascd>2.3.co;2](https://doi.org/10.1130/0016-7606(1995)107<0463:quascd>2.3.co;2)
73. Mccaffrey, R., Stein, S., & Freymueller, J. (2002). Crustal block rotations and plate coupling. *Geodynamics Series*, 30, 101–122.
74. McCann, W. R., Nishenko, S. P., Sykes, L. R., & Krause, J. (1979). Seismic gaps and plate tectonics: Seismic potential for major boundaries. In M. Wyss (Ed.), *Earthquake prediction and seismicity patterns* (pp. 1082–1147). Birkhäuser Basel. https://doi.org/10.1007/978-3-0348-6430-510.1007/978-3-0348-6430-5_2
75. Melnick, D., Bookhagen, B., Strecker, M. R., & Echtler, H. P. (2009). Segmentation of megathrust rupture zones from fore-arc deformation patterns over hundreds to millions of years, Arauco peninsula, Chile. *Journal of Geophysical Research*, 114. <https://doi.org/10.1029/2008JB00578>
76. Métois, M., Socquet, A., & Vigny, C. (2012). Interseismic coupling, segmentation and mechanical behavior of the central Chile subduction zone. *Journal of Geophysical Research*, 117. <https://doi.org/10.1029/2011JB008736>
77. Métois, M., Vigny, C., & Socquet, A. (2016). Interseismic Coupling, megathrust earthquakes and seismic swarms along the Chilean Subduction Zone (38°–18°S). *Pure and Applied Geophysics*, 173, 1431–1449. <https://doi.org/10.1007/s00024-016-1280-5>
78. Moernaut, J., Van Daele, M., Fontijn, K., Heirman, K., Kempf, P., Pino, M., et al. (2018). Larger earthquakes recur more periodically: New insights in the megathrust earthquake cycle from lacustrine turbidite records in south-central Chile. *Earth and Planetary Science Letters*, 481, 9–19. <https://doi.org/10.1016/j.epsl.2017.10.016>
79. Moreno, M., Haberland, C., Oncken, O., Rietbrock, A., Angiboust, S., & Heidbach, O. (2014). Locking of the Chile subduction zone controlled by fluid pressure before the 2010 earthquake. *Nature Geoscience*, 7, 292–296. <https://doi.org/10.1038/ngeo2102>

80. Moreno, M., Li, S., Melnick, D., Bedford, J. R., Baez, J. C., Motagh, M., et al. (2018). Chilean megathrust earthquake recurrence linked to frictional contrast at depth. *Nature Geoscience*, 11, 285–290. <https://doi.org/10.1038/s41561-018-0089-5>
81. Moreno, M., Melnick, D., Rosenau, M., Baez, J., Klotz, J., Oncken, O., et al. (2012). Toward understanding tectonic control on the Mw 8.8 2010 Maule Chile earthquake. *Earth and Planetary Science Letters*, 321–322, 152–165. <https://doi.org/10.1016/j.epsl.2012.01.006>
82. Moreno, M., Rosenau, M., & Oncken, O. (2010). 2010 Maule earthquake slip correlates with pre-seismic locking of Andean subduction zone. *Nature*, 467, 198–202. <https://doi.org/10.1038/nature09349>
83. Moreno, M. S., Bolte, J., Klotz, J., & Melnick, D. (2009). Impact of megathrust geometry on inversion of coseismic slip from geodetic data: Application to the 1960 Chile earthquake. *Geophysical Research Letters*, 36. <https://doi.org/10.1029/2009GL039276>
84. Motagh, M., Schurr, B., Anderssohn, J., Cailleau, B., Walter, T. R., Wang, R., & Villotte, J. P. (2010). Subduction earthquake deformation associated with 14 November 2007, Mw 7.8 Tocopilla earthquake in Chile: Results from InSAR and aftershocks. *Tectonophysics*, 490(1–2), 60–68. <https://doi.org/10.1016/j.tecto.2010.04.033>
85. Müller, R. D., Seton, M., Zahirovic, S., Williams, S. E., Matthews, K. J., Wright, N. M., et al. (2016). Ocean basin evolution and global-scale plate reorganization events since Pangea breakup. *Annual Review of Earth and Planetary Sciences*, 44, 107–138. <https://doi.org/10.1146/annurev-earth-060115-012211>
86. Noda, H., & Lapusta, N. (2013). Stable creeping fault segments can become destructive as a result of dynamic weakening. *Nature*, 493, 518–521. <https://doi.org/10.1038/nature11703>
87. Ojeda, J., Ruiz, S., del Campo, F., & Carvajal, M. (2020). The 21 May 1960 Mw 8.1 Concepción Earthquake: A deep megathrust foreshock that started the 1960 Central-South Chilean seismic sequence. *Seismological Research Letters*, 91(3), 1617–1627. <https://doi.org/10.1785/0220190143>
88. Okada, Y. (1985). Surface deformation due to shear and tensile faults in a half-space. *Bulletin of the Seismological Society of America*, 75, 1135–1154.
89. Oleskevich, D. A., Hyndman, R. D., & Wang, K. (1999). The updip and downdip limits to great subduction earthquakes: Thermal and structural models of Cascadia, south Alaska, SW

- Japan, and Chile. *Journal of Geophysical Research*, 104, 14965–14991. <https://doi.org/10.1029/1999JB900060>
90. Perfettini, H., Avouac, J.-P., Tavera, H., Kositsky, A., Nocquet, J.-M., Bondoux, F., et al. (2010). Seismic and aseismic slip on the Central Peru megathrust. *Nature*, 465, 78–81. <https://doi.org/10.1038/nature09062>
91. Peyrat, S., Madariaga, R., Buforn, E., Campos, J., Asch, G., & Vilotte, J. P. (2010). Kinematic rupture process of the 2007 Tocopilla earthquake and its main aftershocks from teleseismic and strong-motion data. *Geophysical Journal International*, 182, 1411–1430. <https://doi.org/10.1111/j.1365-246X.2010.04685.x>
92. Philipposian, B., & Meltzner, A. J. (2020). Segmentation and supercycles: A catalog of earthquake rupture patterns from the Sumatran Sunda Megathrust and other well-studied faults worldwide. *Quaternary Science Reviews*, 241, 106390. <https://doi.org/10.1016/j.quascirev.2020.106390>
93. Rangelova, E., van der Wal, W., Braun, A., Sideris, M. G., & Wu, P. (2007). Analysis of Gravity Recovery and Climate Experiment time-variable mass redistribution signals over North America by means of principal component analysis. *Journal of Geophysical Research*, 112, F03002. <https://doi.org/10.1029/2006JF000615>
94. Rodríguez-Pérez, Q., & Zuñiga, F. R. (2018). Imaging b -value depth variations within the Cocos and Rivera plates at the Mexican subduction zone. *Tectonophysics*, 734–735, 33–43. <https://doi.org/10.1016/j.tecto.2018.03.019>
95. Ruina, A. (1983). Slip instability and state variable friction laws. *Journal of Geophysical Research*, 88, 10359–10370. <https://doi.org/10.1029/JB088iB12p10359>
96. Ruiz, S., & Madariaga, R. (2018). Historical and recent large megathrust earthquakes in Chile. *Tectonophysics*, 733, 37–56. <https://doi.org/10.1016/j.tecto.2018.01.015>
97. Ruiz, S., Metois, M., Fuenzalida, A., Ruiz, J., Leyton, F., Grandin, R., et al. (2014). Intense foreshocks and a slow slip event preceded the 2014 Iquique Mw 8.1 earthquake. *Science*, 345, 1165–1169. <https://doi.org/10.1126/science.1256074>
98. Saillard, M., Audin, L., Rousset, B., Avouac, J.-P., Chlieh, M., Hall, S. R., et al. (2017). From the seismic cycle to long-term deformation: Linking seismic coupling and Quaternary coastal geomorphology along the Andean megathrust. *Tectonics*, 36, 241–256. <https://doi.org/10.1002/2016TC004156>

99. Sandwell, D. T., Müller, R. D., Smith, W. H. F., Garcia, E., & Francis, R. (2014). New global marine gravity model from CryoSat-2 and Jason-1 reveals buried tectonic structure. *Science*, 346, 65–67. <https://doi.org/10.1126/science.1258213>
100. Savage, J. C. (1983). A dislocation model of strain accumulation and release at a subduction zone. *Journal of Geophysical Research*, 88, 4984–4996. <https://doi.org/10.1029/JB088iB06p04984>
101. Scholz, C. H. (1998). Earthquakes and friction laws. *Nature*, 391, 37–42. <https://doi.org/10.1038/34097>
102. Schurr, B., Asch, G., Hainzl, S., Bedford, J., Hoechner, A., Palo, M., et al. (2014). Gradual unlocking of plate boundary controlled initiation of the 2014 Iquique earthquake. *Nature*, 512, 299–302. <https://doi.org/10.1038/nature13681>
103. Seno, T. (2009). Determination of the pore fluid pressure ratio at seismogenic megathrusts in subduction zones: Implications for strength of asperities and Andean-type mountain building. *Journal of Geophysical Research*, 114, B05405. <https://doi.org/10.1029/2008JB005889>
104. Seno, T., & Yamasaki, T. (2003). Low-frequency tremors, intraslab and interplate earthquakes in Southwest Japan—from a viewpoint of slab dehydration. *Geophysical Research Letters*, 30. <https://doi.org/10.1029/2003GL018349>
105. Smith, L. (2002). A tutorial on principal component analysis. Technical Report OUCS-2002-12. In Department of computer science. University of Otago. Retrieved from <http://www.cs.otago.ac.nz/research/techreports.php>
106. Sobiesiak, M., Meyer, U., Schmidt, S., Götze, H.-J., & Krawczyk, C. M. (2007). Asperity generating upper crustal sources revealed by b-value and isostatic residual anomaly grids in the area of Antofagasta, Chile. *Journal of Geophysical Research*, 112, B12308. <https://doi.org/10.1029/2006JB004796>
107. Sobolev, S. V., & Babeyko, A. Y. (2005). What drives orogeny in the Andes? *Geologica*, 33(8), 617–620. <https://doi.org/10.1130/g21557.1>
108. Song, T.-R. A., & Simons, M. (2003). Large trench-parallel gravity variations predict seismogenic behavior in subduction zones. *Science*, 301, 630–633. <https://doi.org/10.1126/science.1085557>
109. Sparkes, R., Tilmann, F., Hovius, N., & Hillier, J. (2010). Subducted seafloor relief stops rupture in South American great earthquakes: Implications for rupture behavior in the 2010

- Maule, Chile earthquake. *Earth and Planetary Science Letters*, 298, 89–94. <https://doi.org/10.1016/j.epsl.2010.07.029>
110. Sykes, L. R., & Nishenko, S. P. (1984). Probabilities of occurrence of large plate rupturing earthquakes for the San Andreas, San Jacinto, and Imperial faults, California, 1983-2003. *Journal of Geophysical Research*, 89, 5905–5927. <https://doi.org/10.1029/JB089iB07p05905>
111. Tassara, A. (2010). Control of forearc density structure on megathrust shear strength along the Chilean subduction zone. *Tectonophysics*, 495, 34–47. <https://doi.org/10.1016/j.tecto.2010.06.004>
112. Tassara, A., & Echaurren, A. (2012). Anatomy of the Andean subduction zone: Three-dimensional density model upgraded and compared against global-scale models. *Geophysical Journal International*, 189(1), 161–168.
113. Tassara, A., Götze, H.-J., Schmidt, S., & Hackney, R. (2006). Three-dimensional density model of the Nazca plate and the Andean continental margin. *Journal of Geophysical Research*, 111, B09404. <https://doi.org/10.1029/2005JB003976>
114. Tassara, A., & Yáñez, G. (2003). Relación entre el espesor elástico de la litosfera y la segmentación tectónica del margen andino (15–47°S). *Revista Geologica de Chile*, 30. <https://doi.org/10.4067/S0716-02082003000200002>
115. Tilmann, F., Zhang, Y., Moreno, M., Saul, J., Eckelmann, F., Palo, M., et al. (2016). The 2015 Illapel earthquake, central Chile: A type case for a characteristic earthquake? *Geophysical Research Letters*, 43, 574–583. <https://doi.org/10.1002/2015GL066963>
116. Tormann, T., Enescu, B., Woessner, J., & Wiemer, S. (2015). Randomness of megathrust earthquakes implied by rapid stress recovery after the Japan earthquake. *Nature Geoscience*, 8, 152–158. <https://doi.org/10.1038/ngeo2343>
117. Vargas, G., Ortlieb, L., Chapron, E., Valdes, J., & Marquardt, C. (2005). Paleoseismic inferences from a high-resolution marine sedimentary record in northern Chile (23°S). *Tectonophysics*, 399, 381–398. <https://doi.org/10.1016/j.tecto.2004.12.031>
118. Venegas, S. (2001). Statistical methods for signal detection in climate (Rep No 2, Danish Center for Earth System Science (DCESS)).
119. Victor, P., Sobiesiak, M., Glodny, J., Nielsen, S. N., & Oncken, O. (2011). Long-term persistence of subduction earthquake segment boundaries: Evidence from Mejillones

- Peninsula, northern Chile. *Journal of Geophysical Research*, 116, B02402. <https://doi.org/10.1029/2010jb007771>
120. Wallace, L. M., Beavan, J., McCaffrey, R., & Darby, D. (2004). Subduction zone coupling and tectonic block rotations in the North Island, New Zealand. *Journal of Geophysical Research*, 109, B12406. <https://doi.org/10.1029/2004JB003241>
121. Wang, K., & Bilek, S. L. (2014). Invited review paper: Fault creep caused by subduction of rough seafloor relief. *Tectonophysics*, 610, 1–24. <https://doi.org/10.1016/j.tecto.2013.11.024>
122. Wang, K., & Dixon, T. (2004). “Coupling” Semantics and science in earthquake research. *Eos Transactins AGU*, 85, 180. <https://doi.org/10.1029/2004EO180005>
123. Wang, K., & Hu, Y. (2006). Accretionary prisms in subduction earthquake cycles: The theory of dynamic Coulomb wedge. *Journal of Geophysical Research*, 111. <https://doi.org/10.1029/2005JB004094>
124. Wang, K., & Tréhu, A. M. (2016). Invited review paper: Some outstanding issues in the study of great megathrust earthquakes-The Cascadia example. *Journal of Geodynamics*, 98, 1–18. <https://doi.org/10.1016/j.jog.2016.03.010>
125. Wells, R. E., Blakely, R. J., Sugiyama, Y., Scholl, D. W., & Dinterman, P. A. (2003). Basin-centered asperities in great subduction zone earthquakes: A link between slip, subsidence, and subduction erosion? *Journal of Geophysical Research*, 108. <https://doi.org/10.1029/2002JB002072>
126. Wells, R. E., Blakely, R. J., Wech, A. G., McCrory, P. A., & Michael, A. (2017). Cascadia subduction tremor muted by crustal faults. *Geology*, 45, 515–518. <https://doi.org/10.1130/G38835.1>
127. Wiemer, S., & Wyss, M. (1997). Mapping the frequency-magnitude distribution in asperities: An improved technique to calculate recurrence times? *Journal of Geophysical Research*, 102, 15115–15128. <https://doi.org/10.1029/97JB00726>
128. Wilks, D. S. (2016). Modified “Rule N” procedure for principal component (EOF) truncation. *Journal of Climate*, 29, 3049–3056. <https://doi.org/10.1175/JCLI-D-15-0812.1>
129. Yamamoto, Y., Obana, K., Kodaira, S., Hino, R., & Shinohara, M. (2014). Structural heterogeneities around the megathrust zone of the 2011 Tohoku earthquake from

tomographic inversion of onshore and offshore seismic observations. *Journal of Geophysical Research: Solid Earth*, 119, 1165–1180. <https://doi.org/10.1002/2013JB010582>

130. Yue, H., Lay, T., Rivera, L., An, C., Vigny, C., Tong, X., & Báez Soto, J. C. (2014). Localized fault slip to the trench in the 2010 Maule, Chile Mw = 8.8 earthquake from joint inversion of high-rate GPS, teleseismic body waves, InSAR, campaign GPS, and tsunami observations. *Journal of Geophysical Research: Solid Earth*, 119, 7786–7804. <https://doi.org/10.1002/2014JB011340>

References Chapter 3

1. Aki, K. (1979). Characterization of barriers on an earthquake fault. *Journal of Geophysical Research*, 84, 6140. <https://doi.org/10.1029/JB084iB11p06140>
2. Barbot, S., Lapusta, N., Avouac, J.-P., 2012. Under the Hood of the Earthquake Machine: Toward Predictive Modeling of the Seismic Cycle. *Science* 336, 707–710. <https://doi.org/10.1126/science.1218796>
3. Bassett, D., & Watts, A. B. (2015a). Gravity anomalies, crustal structure, and seismicity at subduction zones: 1. Seafloor roughness and subducting relief. *Geochemistry, Geophysics, Geosystems*, 16, 1508–1540. <https://doi.org/10.1002/2014GC005684>
4. Bassett, D., & Watts, A. B. (2015b). Gravity anomalies, crustal structure, and seismicity at subduction zones: 2. Interrelationships between forearc structure and seismogenic behavior. *Geochemistry, Geophysics, Geosystems*, 16, 1541–1576. <https://doi.org/10.1002/2014GC005685>
5. Blanpied, M. L., Lockner, D. A., and Byerlee, J. D. (1995), Frictional slip of granite at hydrothermal conditions, *J. Geophys. Res.*, 100(B7), 13045– 13064, doi:10.1029/95JB00862.
6. Boatwright, J., and Cocco, M. (1996), Frictional constraints on crustal faulting, *J. Geophys. Res.*, 101(B6), 13895– 13909, doi:10.1029/96JB00405.
7. Brantut, N., Schubnel, A., Rouzaud, J.-N., Brunet, F., and Shimamoto, T. (2008), High-velocity frictional properties of clay-bearing fault gouge and implications for earthquake mechanics, *J. Geophys. Res.*, 113, B10401, doi:10.1029/2007JB005551.
8. Brantut (2020). Dilatancy-induced fluid pressure drop during dynamic rupture: Direct experimental evidence and consequences for earthquake dynamics, *Earth and Planetary*

Science Letters, Volume 538, 2020, 116179, SSN 0012-821X,
<https://doi.org/10.1016/j.epsl.2020.116179>.

9. Cattania, C. (2019). Complex earthquake sequences on simple faults. *Geophysical Research Letters*, 46, 10384– 10393. <https://doi.org/10.1029/2019GL083628>
10. Collot, J.-Y., Marcaillou, B., Sage, F., Michaud, F., Agudelo, W., Charvis, P., et al. (2004). Are rupture zone limits of great subduction earthquakes controlled by upper plate structures? Evidence from multichannel seismic reflection data acquired across the northern Ecuador-southwest Colombia margin. *Journal of Geophysical Research*, 109. <https://doi.org/10.1029/2004JB003060>
11. Contreras-Reyes, E., & Carrizo, D. (2011). Control of high oceanic features and subduction channel on earthquake ruptures along the Chile-Peru subduction zone. *Physics of the Earth and Planetary Interiors*, 186, 49–58. <https://doi.org/10.1016/j.pepi.2011.03.002>
12. Dieterich, J. H., Time-dependent friction and the mechanics of stick-slip, *J. Geophys. Res.*, 116 , 790–806, 1978.
13. James H. Dieterich, Earthquake nucleation on faults with rate-and state-dependent strength, *Tectonophysics*, Volume 211, Issues 1–4, 1992, Pages 115-134, ISSN 0040-1951, [https://doi.org/10.1016/0040-1951\(92\)90055-B](https://doi.org/10.1016/0040-1951(92)90055-B).
14. Fukuyama, E., T. Mikumo, and B. Olsen (2003), Estimation of the critical slip-weakening distance: Theoretical background, *Bull. Seismol. Soc. Am.*, 93, 1835–1840, doi:10.1785/0120020184.
15. E. A. Hetland, M. Simons, Post-seismic and interseismic fault creep II: transient creep and interseismic stress shadows on megathrusts, *Geophysical Journal International*, Volume 181, Issue 1, April 2010, Pages 99–112, <https://doi.org/10.1111/j.1365-246X.2009.04482.x>
16. S.A.M. den Hartog, A.R. Niemeijer, C.J. Spiers, New constraints on megathrust slip stability under subduction zone P–T conditions, *Earth and Planetary Science Letters*, Volumes 353–354, 2012, Pages 240-252, ISSN 0012-821X, <https://doi.org/10.1016/j.epsl.2012.08.022>.
17. Hippchen, S., and Hyndman, R. D. (2008), Thermal and structural models of the Sumatra subduction zone: Implications for the megathrust seismogenic zone, *J. Geophys. Res.*, 113, B12103, doi:10.1029/2008JB005698.

18. Hori, T., Miyazaki, S. A possible mechanism of M 9 earthquake generation cycles in the area of repeating M 7~8 earthquakes surrounded by aseismic sliding. *Earth Planet Sp* 63, 48 (2011). <https://doi.org/10.5047/eps.2011.06.022>
19. Horowitz, F. G., and Ruina, A. (1989), Slip patterns in a spatially homogeneous fault model, *J. Geophys. Res.*, 94(B8), 10279– 10298, doi:10.1029/JB094iB08p10279.
20. Jara-Muñoz, J., Melnick, D., Brill, D., & Strecker, M. R. (2015). Segmentation of the 2010 Maule Chile earthquake rupture from a joint analysis of uplifted marine terraces and seismic-cycle deformation patterns. *Quaternary Science Reviews*, 113, 171–192. <https://doi.org/10.1016/j.quascirev.2015.01.005>
21. Kaneko, Y., Avouac, JP. & Lapusta, N. Towards inferring earthquake patterns from geodetic observations of interseismic coupling. *Nature Geosci* 3, 363–369 (2010). <https://doi.org/10.1038/ngeo843>
22. Lambert, V., & Lapusta, N. (2021). Resolving simulated sequences of earthquakes and fault interactions: Implications for physics-based seismic hazard assessment. *Journal of Geophysical Research: Solid Earth*, 126, e2021JB022193. <https://doi.org/10.1029/2021JB022193>
23. Lay, T., & Kanamori, H. (1981). An asperity model of large earthquake sequences. In D. W. Simpson, & P. G. Richards (Eds.), *Earthquake prediction, an international review*, Maurice Ewing series (pp. 579–592). American Geophysical Union. <https://doi.org/10.1029/ME004p0579>
24. Li, D., & Liu, Y. (2017). Modeling slow-slip segmentation in Cascadia subduction zone constrained by tremor locations and gravity anomalies. *Journal of Geophysical Research: Solid Earth*, 122, 3138–3157. <https://doi.org/10.1002/2016JB013778>
25. Liu, Y., and J. R. Rice (2009), Slow slip predictions based on granite and gabbro friction data compared to GPS measurements in northern Cascadia, *J. Geophys. Res.*, 114, B09407, doi:10.1029/2008JB006142.
26. Lui, S., Lapusta, N. Repeating microearthquake sequences interact predominantly through postseismic slip. *Nat Commun* 7, 13020 (2016). <https://doi.org/10.1038/ncomms13020>
27. Luo, Yingdi, Ampuero, Jean-Paul, Stability of faults with heterogeneous friction properties and effective normal stress, *Tectonophysics* (2017), doi:10.1016/j.tecto.2017.11.00

28. Marone, C. (1998), Laboratory-derived friction laws and their application to seismic faulting, *Annu. Rev. Earth Planet. Sci.*, 26, 643–646.
29. Melnick, D., Bookhagen, B., Strecker, M. R., & Echtler, H. P. (2009). Segmentation of megathrust rupture zones from fore-arc deformation patterns over hundreds to millions of years, Arauco peninsula, Chile. *Journal of Geophysical Research*, 114. <https://doi.org/10.1029/2008JB005788>
30. A.J. Meltzner, K. Sieh, H.-W. Chiang, C.-C. Wu, L.L.H. Tsang, C.-C. Shen, E.M. Hill, B.W. Suwargadi, D.H. Natawidjaja, B. Philiposian, R.W. Briggs. Time-varying interseismic strain rates and similar seismic ruptures on the Nias–Simeulue patch of the Sunda megathrust
31. Métois, M., Vigny, C. & Socquet, A. Interseismic Coupling, Megathrust Earthquakes and Seismic Swarms Along the Chilean Subduction Zone (38°–18°S). *Pure Appl. Geophys.* 173, 1431–1449 (2016). <https://doi.org/10.1007/s00024-016-1280-5>
32. Molina, D., Tassara, A., Abarca, R., Melnick, D., & Madella, A. (2021). Frictional segmentation of the Chilean megathrust from a multivariate analysis of geophysical, geological, and geodetic data. *Journal of Geophysical Research: Solid Earth*, 126, e2020JB020647. <https://doi.org/10.1029/2020JB020647>
33. Moreno, M., Rosenau, M., & Oncken, O. (2010). 2010 Maule earthquake slip correlates with pre-seismic locking of Andean subduction zone. *Nature*, 467, 198–202. <https://doi.org/10.1038/nature09349>
34. Mitchell, E. K., Y. Fialko, and K. M. Brown (2016), Velocity-weakening behavior of Westerly granite at temperature up to 600 ° C, *J. Geophys. Res. Solid Earth*, 121, 6932–6946, doi:10.1002/2016JB013081.
35. Noda, H., Lapusta, N., 2013. Stable creeping fault segments can become destructive as a result of dynamic weakening. *Nature* 493, 518–521. <http://dx.doi.org/10.1038/nature11703>.
36. Ojeda, J., Ruiz, S., del Campo, F., & Carvajal, M. (2020). The 21 May 1960 Mw 8.1 Concepción Earthquake: A deep megathrust foreshock that started the 1960 Central-South Chilean seismic sequence. *Seismological Research Letters*, 91(3), 1617–1627. <https://doi.org/10.1785/0220190143>

37. Ohnaka, M. (2003), A constitutive scaling law and a unified comprehension for frictional slip failure, shear fracture of intact rock, and earthquake rupture, *J. Geophys. Res.*, 108(B2), 2080, doi:10.1029/2000JB000123.
38. Okamoto, A. S., Verberne, B. A., Niemeijer, A. R., Takahashi, M., Shimizu, I., Ueda, T., & Spiers, C. J. (2019). Frictional properties of simulated chlorite gouge at hydrothermal conditions: Implications for subduction megathrusts. *Journal of Geophysical Research: Solid Earth*, 124, 4545–4565. <https://doi.org/10.1029/2018JB017205>
39. Perfettini, H., and Ampuero, J.-P. (2008), Dynamics of a velocity strengthening fault region: Implications for slow earthquakes and postseismic slip, *J. Geophys. Res.*, 113, B09411, doi:10.1029/2007JB005398.
40. Philibosian, B., & Meltzer, A. J. (2020). Segmentation and supercycles: A catalog of earthquake rupture patterns from the Sumatran Sunda Megathrust and other well-studied faults worldwide. *Quaternary Science Reviews*, 241, 106390. <https://doi.org/10.1016/j.quascirev.2020.106390>
41. Phillips, N. J., Belzer, B., French, M. E., Rowe, C. D., & Ujiie, K. (2020). Frictional strengths of subduction thrust rocks in the region of shallow slow earthquakes. *Journal of Geophysical Research: Solid Earth*, 125, e2019JB018888. <https://doi.org/10.1029/2019JB018888>
42. Plata-Martinez, R., Ide, S., Shinohara, M. *et al.* Shallow slow earthquakes to decipher future catastrophic earthquakes in the Guerrero seismic gap. *Nat Commun* 12, 3976 (2021). <https://doi.org/10.1038/s41467-021-24210-9>
43. L. Prawirodirdjo, R. McCaffrey, C.D. Chadwell, Y. Bock, C. Subarya. Geodetic observations of an earthquake cycle at the Sumatra subduction zone; role of interseismic strain segmentation. *J. Geophys. Res.*, 115 (2010), 10.1029/2008JB006139 Article B03414
44. Rubin, A. M., and Ampuero, J.-P. (2005), Earthquake nucleation on (aging) rate and state faults, *J. Geophys. Res.*, 110, B11312, doi:10.1029/2005JB003686.
45. Rice, J. R. (1980), The mechanics of earthquake rupture, in *Physics of the Earth's Interior*, Proc. Int. Sch. Phys. Enrico Fermi, vol. 78, edited by A. M. Dziewonski and E. Boschi, pp. 555 – 649.
46. Demian M Saffer, Chris Marone, Comparison of smectite- and illite-rich gouge frictional properties: application to the updip limit of the seismogenic zone along subduction

megathrusts, *Earth and Planetary Science Letters*, Volume 215, Issues 1–2, 2003, Pages 219–235, ISSN 0012-821X, [https://doi.org/10.1016/S0012-821X\(03\)00424-2](https://doi.org/10.1016/S0012-821X(03)00424-2).

47. Saillard, M., Audin, L., Rousset, B., Avouac, J.-P., Chlieh, M., Hall, S. R., et al. (2017). From the seismic cycle to long-term deformation: Linking seismic coupling and Quaternary coastal geomorphology along the Andean megathrust. *Tectonics*, 36, 241–256. <https://doi.org/10.1002/2016TC004156>
48. Sawai, M., A. R. Niemeijer, O. Plümper, T. Hirose, and C. J. Spiers (2016), Nucleation of frictional instability caused by fluid pressurization in subducted blueschist, *Geophys. Res. Lett.*, 43, 2543–2551, doi:10.1002/2015GL067569.
49. Sawai, M., A. R. Niemeijer, T. Hirose, and C. J. Spiers (2017), Frictional properties of JFAST core samples and implications for slow earthquakes at the Tohoku subduction zone, *Geophys. Res. Lett.*, 44, 8822–8831, doi:10.1002/2017GL073460.
50. Sparkes, R., Tilmann, F., Hovius, N., & Hillier, J. (2010). Subducted seafloor relief stops rupture in South American great earthquakes: Implications for rupture behavior in the 2010 Maule, Chile earthquake. *Earth and Planetary Science Letters*, 298, 89–94. <https://doi.org/10.1016/j.epsl.2010.07.029>
51. Tanikawa, W. & Shimamoto, T. Frictional and transport properties of the Chelungpu fault from shallow borehole data and their correlation with seismic behavior during the 1999 Chi-Chi earthquake. *J. Geophys. Res.* 114, B01502 (2009)
52. Tassara, A. (2010). Control of forearc density structure on megathrust shear strength along the Chilean subduction zone. *Tectonophysics*, 495, 34–47. <https://doi.org/10.1016/j.tecto.2010.06.004>
53. L.L.H. Tsang, A.J. Meltzner, E.M. Hill, J.T. Freymueller, K. Sieh A paleogeodetic record of variable interseismic rates and megathrust coupling at Simeulue Island, Sumatra
54. Tullis, T. E. (1988), Rock friction constitutive behavior from laboratory experiments and its implications for an earthquake prediction field monitoring program, *Pure Appl. Geophys.*, 126, 555–588.
55. Verberne, B. A., Niemeijer, A. R., De Bresser, J. H. P., and Spiers, C. J. (2015), Mechanical behavior and microstructure of simulated calcite fault gouge sheared at 20–600°C: Implications for natural faults in limestones, *J. Geophys. Res. Solid Earth*, 120, 8169–8196, doi:10.1002/2015JB012292.

56. Völker, D., Grevenmeyer, I., Stipp, M., Wang, K., and He, J. (2011), Thermal control of the seismogenic zone of southern central Chile, *J. Geophys. Res.*, 116, B10305, doi:[10.1029/2011JB008247](https://doi.org/10.1029/2011JB008247).
57. Wang, K., & Bilek, S. L. (2014). Invited review paper: Fault creep caused by subduction of rough seafloor relief. *Tectonophysics*, 610, 1–24. <https://doi.org/10.1016/j.tecto.2013.11.024>
58. Kelin Wang, Jiangheng He; Effects of Frictional Behavior and Geometry of Subduction Fault on Coseismic Seafloor Deformation. *Bulletin of the Seismological Society of America* 2008;; 98 (2): 571–579. doi: <https://doi.org/10.1785/0120070097>
59. Wei, M., & Pengcheng, S. (2021). Synchronization of earthquake cycles of adjacent segments on oceanic transform faults revealed by numerical simulation in the framework of rate-and-state friction. *Journal of Geophysical Research: Solid Earth*, 126, e2020JB020231. <https://doi.org/10.1029/2020JB020231>
60. Weng, H., Ampuero, JP. Continuum of earthquake rupture speeds enabled by oblique slip. *Nat. Geosci.* 13, 817–821 (2020). <https://doi.org/10.1038/s41561-020-00654-4>
61. Wesnousky, S. Predicting the endpoints of earthquake ruptures. *Nature* 444, 358–360 (2006). <https://doi.org/10.1038/nature05275>